THÈSE

PRÉSENTÉE A

L'UNIVERSITÉ BORDEAUX 1

ÉCOLE DOCTORALE DES SCIENCES CHIMIQUE

Par Seydou, YAO

POUR OBTENIR LE GRADE DE

DOCTEUR

SPÉCIALITÉ: Physico-chimie de la matière condensée

Imagerie IRTF de haute résolution des interactions cellules-fibres pour l'étude des effets pathogènes des amiantes

Directeur de thèse : Cyril Petibois
Co-directeur : Giancarlo Della Ventura

Soutenue le : 07/11/2012

Université Bordeaux 1
Les Sciences et les Technologies au service de l'Homme et de l'environnement

Devant la commission d'examen formée de :

M. Moenner, Michel	Professeur Université de Bordeaux 2	Président du Jury
M. Augusto Marcelli	Directeur de recherche, INFN-LNF, Frascati	Rapporteur
M. Yeukuang Hwu	Professeur, Institute of Physics, Taipei	Rapporteur
M. Giancarlo DellaVentura	Professeur Université de Rome 3 Établissement	Co-directeur
M. Cyril Petibois	Maitre de conférences, Université Bordeaux 1	Directeur

This PhD work has been performed thanks to the grant of the university Italian-French University (Vinci program 2009):

- **Imagerie IRTF de haute résolution des interactions cellules-fibres pour l'étude des effets pathogènes des amiantes.**

- **Immagini FTIR ad alta risoluzione dell'interazione fibracellula per lo studio degli effetti patogeni dell'amianto.**

- **High resolution FTIR imaging of fibers / cell interactions for the study of the pathological effect of asbestos.**

Résumé

Il est assez bien accepter que des maladies pulmonaires tel que l'amiantose ou le mésotheliome, dont la sévérité dépend du phénotype cellulaire impliqué, proviennent de l'interaction entre les fibres d'amiantes et les cellules humaines. Du fait de l'hétérogénéité morphologique et chimique des fibres et l'obligation de disposer de moyens analytique capable d'analyser l'interaction organique – inorganique, les détails du processus pathologique reste largement inconnus. En effet, la toxicité des fibres d'amiantes ne dépend pas seulement de leurs dimensions mais aussi de leurs formes et chimie de surface. Cela implique qu'il existe de nombreux type d'interaction fibre – cellule, rendant difficile l'interprétation du phénomène. Grace à leurs capacités non invasives, d'investiguer à un niveau cellulaire et la possibilité de sonder les fonctions moléculaires, les techniques spectroscopiques tels que l'infrarouge and le Raman sont appropriés pour évaluer ces interactions fibre – cellules. Cependant, il existe certaines limites analytiques tels que la perte de sensitivité des détecteurs infra rouge en travaillant avec des sections de tissus ou d'échantillons de faible épaisseurs, la limite de résolution latéral et spatiale et l'impossibilité d'analyser les échantillons riche en eau. Des études préliminaires réalisées dans notre laboratoire ont permis de développer l'imagerie infra rouge couplé avec une matrice plan focal bidimensionnelle de détecteurs utilisant le rayonnement synchrotron afin de surpasser ces inconvénients. En effet, ces études ont permis de voir l'amélioration du rapport signal sur bruit en utilisant le rayonnement synchrotron plutôt que la source Globar. De plus, l'utilisation de ce rayonnement synchrotron permet de réduire la résolution latérale de la technique à l'échelle micrométrique et augmenter sa sensitivité. Durant ce travail doctoral, des expériences ont été réalisées pour déterminer les substrats qui permettraient d'obtenir une qualité de culture cellulaire corrélée à une bonne image spectrale sur la base de leurs propriétés physiques et biologique. Cela a mis en évidence que les substrats les plus adéquats pour réaliser de l'imagerie infrarouge sont le Si, Ge et Si_3N_4. Par conséquent, l'application de l'imagerie infrarouge couplé au rayonnement synchrotron avec des cellules cryofixées sur des substrats de nitrure de silicium a

permis de déterminer les modifications de contenus cellulaires sous différentes conditions expérimentales. Une fois cette expérience accomplie, en mettant en pratique notre connaissance du rayonnement synchrotron couplé avec les détecteurs à matrice plan focaux et notre capacité à exécuter des cultures cellulaires ex vivo de cellule individuel sur un substrat de silicium, nous avons développé une méthode d'analyse afin d'évaluer les effets de l'interaction entre des matériaux inorganiques (fibres d'amiantes) et des cellules pulmonaires. En comparant les résultats obtenus à partir de différents type de fibres et différentes concentrations, nous avons observé que les changements moléculaires induites dans les cellules pouvait être différenciés et a permis ainsi de confirmer la capacité de l'imagerie infrarouge à déceler les changements moléculaires dans une cellule unique. Dès lors, nous avons décidé d'explorer l'interaction in vitro entre les fibres et les cellules individuelles en utilisant la spectroscopie Raman. Le principal objectif était de suivre le comportement in vitro des cellules individuelles en contact avec les fibres d'amiantes afin d'avoir une meilleure compréhension de l'effet pathogénique des fibres. Avec l'aide de techniques multivariées tel que l'analyse en composante principal ou l'analyse de classes, nous avons pu remarquer que les petites fibres de moins de 5µm peuvent être internalisés par la cellule pendant que les plus larges fibres (<15µm) ne le peuvent pas. Ainsi, l'utilisation des techniques spectroscopiques tels que le Raman et l'infrarouge nous ont permis d'obtenir simultanément des informations morphologique et chimique sur le system, permettant d'avoir une meilleure vision du mécanisme de défense des cellules vivante individuelles en interaction avec les fibres d'amiantes.

Abstract

Interaction of asbestos fibers with human cells cause lung diseases such as asbestosis and mesothelioma, whose severity is directly dependent on the cellular phenotypes involved. Details of this process remain largely unknown because of the chemical heterogeneity and morphology of the fibers and the requirement of organic-inorganic analytical means. Indeed, the toxicity of these fibers depends not only on their dimensions, but also on their habit and surface chemistry. Therefore, there are multiple fiber-cell interactions and phenomena making challenging their interpretation. Because of their non invasiveness, their ability to investigate at a cellular level and the possibility to probe molecular function, spectroscopic methods as FTIR and Raman spectroscopy are suitable techniques to evaluate these fiber cells interactions. However, there are some analytical limitations such as the depletion of the sensitivity of IR detectors by working with thick tissue sections or very small sample, the limitation of resolution due to the spatial and lateral resolution and the impossibility to analyze sample rich in water. Preliminary studies performed in our laboratory as part of this PhD project, permitted to develop FTIR imaging coupled with bi-dimensional focal-plane-array (FPA) of detectors using synchrotron radiation in order to overcome these drawbacks. Indeed, recent studies have revealed that it is possible to obtain a higher SNR by using synchrotron radiation rather than Globar source. Moreover, the use of SR radiation permits to reduce the lateral resolution of the technique to the micrometer scale and to increase his sensitivity. In this work, experiments were realized to determine the substrates which allow a high quality of cell culture and good IR spectral image on the basis of the physical and biological properties of each substrate. This led to determine that Si, Ge and Si_3N_4 are the best substrates for FTIR imaging. Consequently, we applied SR-FTIR imaging with cryofixed cells on Si_3N_4 substrate to determine the cellular content changes under different experimental conditions. Once settled, by implementing our knowledge of SR-IR radiation coupled to FPA detectors and our ability to perform individual ex vivo cells culture on Si substrate, we developed a method to analyze the effect of the interactions between inorganic materials (asbestos fibers) and

organic materials (cells). By comparing the results obtained from different types of fibers and concentrations, we observed that the molecular change induced on cells could be differentiated. Thus, IR imaging confirmed its ability to show molecular changes in one cell as previously revealed. Henceforth, we decided to investigate the *in vitro* interaction between asbestos and single cells using Raman spectroscopy. The main goal was to monitor the *in vitro* behavior of single cells in contact with asbestos fibers to get a better understanding of the pathogenic effect of the fiber. With the help by multivariate analysis such as principal component analysis or cluster analysis, we found out that the small fibers can be apparently well internalized by the cell, while larger fibers are not internalized. Thus, the use of spectroscopic techniques as Raman and FTIR spectroscopy allowed us to obtain simultaneously morphological and chemical information on the system, thus providing a further insight into the mechanism of defense of single living cells interacting with asbestos fiber.

Riassunto

L'interazione tra fibre di amianto e cellule umane causa malattie polmonari come l'asbestosi e il mesotelioma, la cui gravità dipende direttamente dai fenotipi cellulari coinvolti. I dettagli di questo processo rimangono in gran parte sconosciuti a causa della eterogeneità chimica e morfologica delle fibre e della mancanza di metodi in grado di analizzare sistemi che sono simultaneamente organici ed inorganici. Infatti, la tossicità delle fibre dipende non solo dalle dimensioni, ma anche dalla loro morfologia e dalla composizione chimica superficiale. Pertanto, vi sono diverse modalità di interazione tra fibre e cellule, che rendono difficile l'interpretazione del fenomeno. A causa della loro non invasività, la loro capacità di indagare a livello cellulare e la possibilità di analizzare le funzioni molecolari, i metodi spettroscopici come FTIR e Raman sono tecniche adatte per studiare l'interazione fibra/cellula. Tuttavia, vi sono alcuni limiti analitici come la mancanza di sensibilità dei rilevatori IR per sezioni troppo spesse di tessuto o per campioni molto piccoli, la scarsa risoluzione spaziale e la difficoltà di analizzare campioni ricchi in acqua. Studi preliminari condotti nel nostro laboratorio hanno permesso di sviluppare tecniche di imaging FTIR utilizzando rivelatori bi-dimensionali FPA (focal-plane-array) e radiazione di sincrotrone per superare questi inconvenienti. Infatti, studi recenti hanno rivelato che è possibile ottenere un miglior SNR utilizzando radiazione di sincrotrone, piuttosto che una sorgente Globar. Inoltre, l'uso di radiazione di sincrotrone permette di migliorare la risoluzione laterale fino al micron e di aumentare la sensibilità della misura. In questo lavoro, sono stati realizzati esperimenti per determinare i substrati che consentono simultaneamente una elevata qualità della coltura cellulare e buone immagini spettroscopiche IR sulla base delle proprietà fisiche e biologiche di ogni substrato. Ciò ha permesso di riconoscere i substrati di Si, Ge e Si3N4 come ottimi candidati per l'imaging FTIR. Di conseguenza, abbiamo utilizzato metodi di imaging SR-FTIR su cellule cresciute su substrato di Si3N4 e criofissate per studiare i cambiamenti del contenuto cellulare in differenti condizioni sperimentali. Una volta stabilite le migliori condizioni sperimentali, e dopo aver migliorato la nostra conoscenza sull'uso della radiazione di sincrotrone

accoppiata ai rivelatori FPA e la nostra capacità di eseguire le culture di cellule sui substrati di Si, abbiamo sviluppato un metodo per analizzare l'effetto dell'interazione tra un materiale inorganico (le fibre di amianto) e un materiale organico (le cellule). Confrontando i risultati ottenuti con differenti tipi di fibre e diverse concentrazioni, abbiamo osservato che il cambiamento molecolare indotto sulle cellule poteva essere caratterizzato, e che quindi le tecniche di imaging IR permettevano effettivamente di analizzare i cambiamenti molecolari in una cellula. In una seconda fase abbiamo deciso di studiare l'interazione in vitro tra amianto e singola cellula utilizzando la spettroscopia Raman. L'obiettivo principale era di monitorare il comportamento in vitro delle cellule in contatto con le fibre di amianto per avere una migliore comprensione dell'effetto patogeno della fibra. Con l'aiuto di analisi multivariata come l'analisi delle componenti principali o la cluster analisi, abbiamo scoperto che le fibre di piccole dimensioni possono essere ben interiorizzate dalla cellula, mentre le fibre grandi non vengono internalizzate. Pertanto, l'uso combinato di tecniche spettroscopiche come Raman e FTIR permettono di ottenere simultaneamente informazioni morfologiche e chimiche sul fenomeno dell'interazione tra fibre di amianto e singole cellule, consentendo di migliorare la nostra comprensione del meccanismo di difesa della cellula vivente.

TABLE OF CONTENTS

ABBREVIATIONS

A549: Adenocarcinoma human alveolar basal epithelial cells

ATCC: American type culture collection

ATR: Attenuated Total Reflection

CARS: Coherent anti-Stokes Raman scattering spectroscopy

CCD: Charge couple device

DMEM: Dulbecco’s modified eagle medium

DNA : Desoxy ribonucleic acid

FTIR: Fourier Transformed InfraRed

FPA: Focal Plane Arrays

GPa: GigaPascal

HCA: Hierarchical cluster analysis

HCMEC: Human cerebral microvascular endothelial cell

IARC: International Agency for Research on Cancer

MPa : MegaPascal

MTT: Mitochondrial tetrazole assay

NA: Numerical aperture

OLS: Ordinary least squares

PC: Principal component

PCA: Principal component analysis

PCR: Principal component regression

PBS: Phosphate buffered saline

PLS: Partial least squares regression

RNA: Ribonucleic acid

RNS : Reactive nitrogen species

ROS: Reactive oxygen species

SEM: Scanning electron microscopy

SERS: Surface Enhanced Raman Scattering

SNR: Signal-to-noise ratio

SR: Synchrotron radiation

TEM: Transmission electron microscopy

1. ASBESTOS FIBERS

There are more than two hundreds types of natural minerals fibers coming from rocks. Volatile, most of them are not harmless but others as asbestos show a real pathogenicity for humans. Asbestos is a commercial term applied to six varieties of naturally occurring fibrous mineral that have been widely exploited industrially. The practical use of these minerals is ancient but the demand for asbestos fibers grew exponentially in the beginning of the 20th century. This inflation was due to their thermal properties, average tensile strength, resistance to fire, heat, electrical and chemical damage of these materials used in the automobile industry and for military applications. The maximum of production was in 1977 with $4,8.10^6$ tons produced and is currently around 2.10^6 tons per year worldwide[1].

The world production had decreased since 1978 because of health issues linked to the use of asbestos fibers. Early the 1980s, a series of pathologies were developed by asbestos mining workers. Thus, researchers as Goldsmith[2] debated the relationship between silica exposure and lung cancer and suggested that silica based minerals were carcinogen and lung cancer were due to minerals, ‘foreign bodies’ in the biological environment; the results were enhanced by epidemiological evidence. As a consequence, the International Agency for Research on Cancer (IARC) defined asbestos fibers properties; evaluated asbestoses as lung carcinogenic fibers and related the exposure to asbestos with the risk of pulmonary diseases as nonmalignant inflammatory (pleural plaques, asbestosis…) and malignant (mesothelioma and bronchogenic carcinoma) diseases; differences were related to the cellular phenotypes as well as the nature of the asbestos involved [3, 4]. Later, the studies revealed that the fibers carcinogenicity is not simply correlated to the exposure but depends on the chemistry and structure of each type of fiber. Thus, the six varieties of fibers were regulated by the safety administration exposure standards [5].

Asbestos fibers belong to two classes of minerals: serpentines and amphiboles. These two groups occur also in non fibrous forms, which are not considered as asbestos, but are more common and widespread than the fibrous varieties. Thus, within the serpentine group only one fiber has a fibrous shape. Named Chrysotile, it is a magnesium silicate mineral. On the other hand, there are five asbestiform varieties of amphiboles – see figure 1. Asbestiforms are defined as fibrous shape occurring in bundles that can be divided or cleaved into thinner fibers (less than 0.5 µm in width) with high tensile strengths and high aspect ratio (length/diameter of 20:1 to 100:1 or higher for fibers longer than 5 µm up to 200µm).

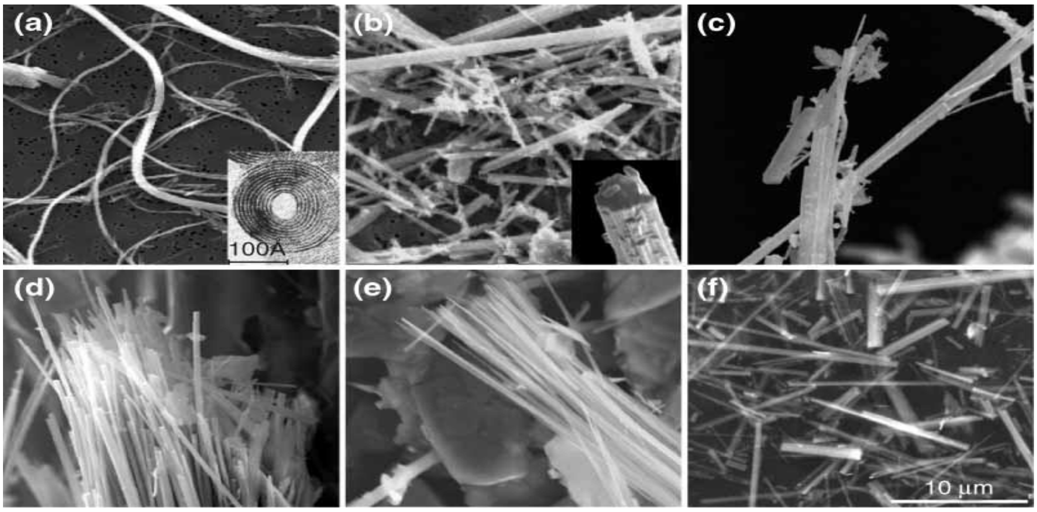

Figure 1: Shapes of asbestos fibers by transmission electron microscopy (TEM): (a) chrysotile, (b) crocidolite, (c) anthophyllite, (d) winchite-richterite asbestos (e) tremolite and (f) amosite. Scale bar = 10 µm **[6].**

These six industrial minerals share a set of physical and chemical properties that make them unique, such as their high tensile strengths or resistance to chemical damage, even if each can be distinguished by its compositions or structure. Indeed, chrysotile has a planar sheet-like structure which is rolled up to finally give needles, while amphibole minerals are characterize by a double-chain arrangement of Si-O tetrahedra as shown in (a) and (b) from figure 1 above.

Amphiboles are considered as more powerful carcinogens than chrysotile fibers due to their physical and chemical properties. As a consequence, more than 95% of world exploitation of asbestos regards the chrysotile specie. The chemistry of fibers is considered as main inducer of the pathogenicity of fibers.

1.1 CHEMISTRY OF FIBERS

The term “asbestos fibers” refers to a family of silicate based mineral described by a heterogeneous chemistry and morphology. The diversity of crystallization of the silicate chains into thins fibrous structures can explain this variety of fibers. The chemical properties within each class of fibers, i.e., the serpentine characterized by chrysotile and the amphiboles group, will be discussed in the next section.

1.1.1 SERPENTINES

Chrysolite asbestos, one of the polymorph minerals in the serpentine phyllosilicate group is chemically a hydrated magnesium silicate with an ideal composition = $Mg_3Si_2O_5(OH)_4$. The two other common serpentine minerals are lizarite and antigorite. The formation is realized thanks to the co-deposition of many minerals as brucite ($Mg(OH)_2$), magnetite (Fe_3O_4), calcite ($CaCO_3$), dolomite ($(Mg,Ca)(CO_3)_2$), chlorite ($(Mg,Al,Fe)_{12}Si_8O_{20}(OH)_{16}$), and talc ($Mg_6Si_8O_{20}(OH)_4$), the stress and deformations in the host matrix, the water content, the temperature cycles during geological periods, etc… Chrysotile fibers are found in veins in serpentinite rocks, they grow as extended sheets that tend to enfold forming a tubular fiber structure. These crystalline fibers are usually curved; hence the name ‘serpentine’; extremely thin and flexible, see figure 2.

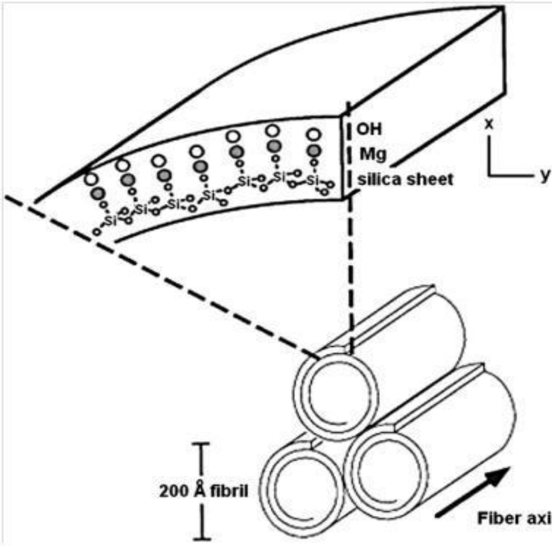

Figure 2: Microscopic structure of chrysotile fibers [7].

The properties of chrysotile fibers are correlated to their chemical composition but also to their crystal structure. Chrysotile's crystal structure is formed by a double layer composed of a tetrahedral and octahedral sheets. The octahedral brucite layer – $(Mg_6O_4(OH)_8)^{4-}$ – is intercalated between each silicate tetrahedral sheet and bonded together by oxygen atoms [8]. This difference of distance between O-O forces the double sheet to roll up leading to the tubular shape characteristic of chrysotile [9]. This kind of structure explains why chrysotile fibers have a poor chemical persistence. Indeed, the outer octahedral layer of chrysotile is readily leached of magnesium, even under pH=4 to ph=6 acid conditions [10].

1.1.2 AMPHIBOLES

The amphibole group of asbestos includes the species amosite (grunerite), crocidolite (riebeckite), tremolite, anthophyllite, and actinolite. The different amphibole species have different geological origin but the common point is the necessity of mechanical stress or high temperature during their chemicals reactions of formation or metamorphic process [11].

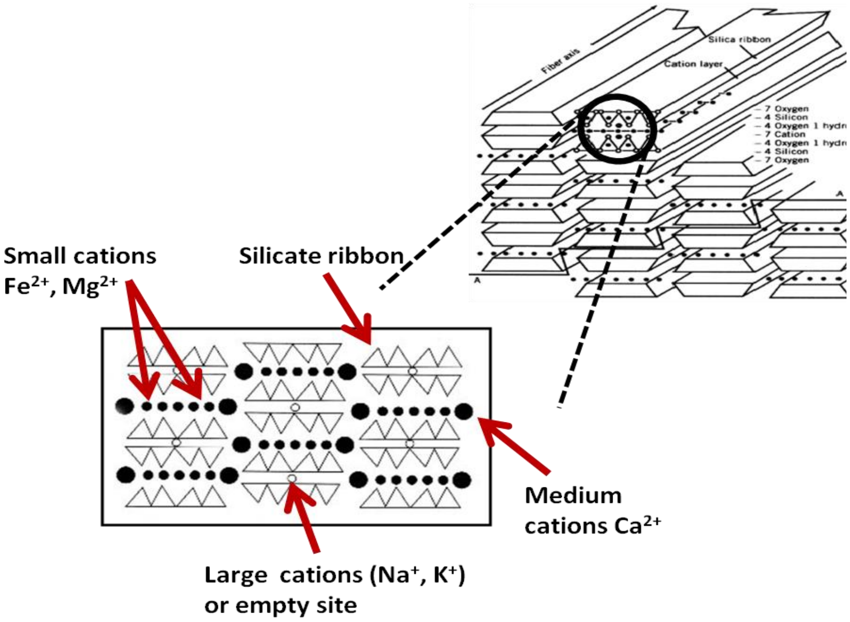

Figure 3: Schematic structure of amphibole fibers (adapted from [12]). There are different cationic sites that can accept different types of atoms, depending on their size.

The chemical composition of the amphiboles may be represented by the following general formulae:

$$\mathbf{A}_{\mathbf{0}\text{-}1}, \mathbf{B}\,_2\mathbf{C}_5\mathbf{T}_8O_{22}\,(OH, O, F, Cl)_2$$

Where **A**= Na or K ;

B = Na, Ca, Mg, Fe^{+2}, Mn, Li

C= Al, Fe^{+2}, Fe^{+3}, Ti, Mg, Mn or Cr

T= Si, Al

A, B, C represent different cationic sites having different sizes within the crystal structure [8].

This formula reveals that the amphibole group includes many mineral species characterized by different cation substitutions at the structural sites. For example, tremolite and actinolite are related by the substitution (at the C-sites) of divalent iron (dominant in actinolite) by magnesium (dominant in tremolite).

Amphibole fibers usually come out as individual species rather than as bundles and with a linear double chain as polymeric structure. These chains crystallize into long, thin, and straight fibers, which structure is characteristic of this kind of asbestos fibers.

Amphiboles crystallize either as a monoclinic, rectangular prism with a parallelogram as its base, than an orthorhombic - rectangular prism with rectangular base - forms. The crystal structure is based on double Si_4O_{11} chains of tetrahedral. The arrangement contains several cation sites which host atoms with different coordination, charge and dimension. Two double chains of this silica tetrahedral group are placed back to back and linked along the c-axis; axis corresponding to the direction of elongation in all amphibole fiber (figure 3) [13].

1.2 PHYSICAL PROPERTIES OF ASBESTOS FIBERS

Asbestos fibers, known as miracle fibers in the 1950s, have a set of properties that make them ideal for a variety of construction and insulation purposes. The most important for industrial application is the fiber length distribution. Indeed, the length and the distribution of the fibers play a central role in the performance of the final material where the fiber is embedded. Other physico-chemical properties as: 1- the thermal behavior during heating which is relatively stable, mechanically stable with a low weight loss 2- the high tensile strength (near 10 GPa; thanks to the Si-O-Si bonds) superior to the tensile strength of steel (between 450 - 1970 MPa) [14] and the flexibility 3- the hardness comparable to other glassy silicate 4- the high electrical resistivity used for electrical insulation applications and 5- a good resistance to acids and bases. The most important physical and chemical properties of the six regulated asbestos minerals are summarized in the Table 1.

The table shows that:

- The chemical stability of amphibole fibers is better in acid environment compared to chrysotile. This explains why amphiboles fibers remain longer in the lung compared to chrysotile.
- Amphiboles develop more fibrous shapes than chrysotile. This feature can be related to the high carcinogenic potential of amphibole.
- Chrysotile fibers have a higher flexibility and thus a lower hardness than the amphibole. This explains the larger use of chrysotile instead of amphiboles for many industrial applications.

characteristic	Chrysotile	Amosite	Tremolite	Actinolite	Anthophyllite	Crocidolite
Chemical formula	Mg3Si2O5(OH)4	$(Fe^{+2})_2(Fe^{+2},Mg)_5Si_8O_{22}(OH)_2$	$Ca_2Mg_5Si_8O_{22}(OH)_2$	$Ca_2(Mg,Fe^{+2})Si_8O_{22}(OH)_2$	$Mg_7Si_8O_{22}(OH)_2$	$Na_2(Fe^{+2},Mg)_3Fe^{+3}Si_8O_{22}(OH)_2$
Color	White, gray, green, yellowish	Brown, gray, greenish	White to pale green	Green	White, brown-gray	Lavender, blue, green
CAS registry	[*12001-29-5*]	[12172-73-5]	[14567-73-8]	[12172-67-7]	[17068-78-9]	[12001-28-4]
Structure	structure as veins in serpentine and mass fiber deposits	lamellar, coarse to fine, fibrous and asbestiform	long, prismatic, and fibrous aggregates			fibrous in ironstones
Physical state	Solid	Solid	Solid	Solid	Solid	Solid
hardness, Mohs	2.5-4.0	5.5-6.0	5.5			4.0
specific gravity	2.4-2.6	3.1-3.25	2.9-3.2	3.0–3.2	2.85–3.1	3.2-3.3
Specific surface area (m^2/g)	26.8 ± 0.7	5.7 ± 0.3	NA	NA	11.8 ± 1.0	8.3 ± 0.5
optical properties	biaxial positive parallel extinction	biaxial positive parallel extinction	biaxial negative oblique extinction	NA	NA	biaxial oblique extinction
refractive index	1.53-1.56	1.63-1.73	1.60-1.64	NA	NA	1.65-1.72
flexibility	high	fair	fair to good	Fair to brittle	Fair to brittle	poor,generally brittle
texture	silky, soft to harsh	coarse but somewhat pliable	generally harsh	NA	NA	soft to harsh
tensile strength, Mpa	1100-4400	1500-2600	<500	NA	NA	1400-4600
resistance to: acids 4 < pH< 6	weak, undergoes fairly rapid attack	fair, slowly attacked	good	NA	NA	good
resistance to : alkalies 7 < pH< 10	very good	good	good	NA	NA	good
surface charge, mV (zeta potential)	+13.6 to +54b	-20 to -40	NA	NA	NA	-32
decomposition temperature, °C	800-850	600-900	1040		950	800

Table 1: Physical and chemical properties of the six regulated varieties of asbestos fibers [15-17]

1.3 PHYSICAL STUDY AND ANALYSIS OF FIBERS

The mineral composition and structure of asbestos fibers are characterized through different analytical methods. Indeed, morphological characterization is not enough to ensure the identification of these fibers. Thus, microscopic methods or other analytical techniques must be used. Optical microscopy is the easiest way of identification when the sample size is in the micrometric scale; the spatial resolution of the fiber must be better than 0.2 µm of diameter to be seen by this technique. It's a powerful technique, fast and accessible allowing the recognition of the different types of asbestos thanks to their differences of optical properties and shape. Identification can also be performed with the transmission or scanning electron microscopy (TEM, SEM) techniques. These techniques allow the visualization of the thinnest fibrils and counting of fibers in small samples. Coupled with an energy-dispersive X-ray spectrometer, it is possible to determine the elemental composition of the fiber; they are however non routine techniques and require strong manipulation of the sample. When the samples contain a large amount of fibers, the characterization can be accomplished using X-ray fluorescence (XRF), Secondary ion mass spectrometry (SIMS), laser microprobe mass spectrometry (LMMS) or X-ray photoelectron spectroscopy (XPS) [18]. Indeed, the diffraction technique by X-ray allows the identification of the different types of asbestos fibers and also their minerals composition [19]. There are also other techniques to determinate the type of fibers. Thermo-analytical methods as DTA (Differential Thermal Analysis), TGA (Thermo Gravimetric Analysis), or DSC (Differential Scanning Calorimetry), can be used as complementary techniques to identify the asbestos fiber. Indeed, the unique feature observed to each asbestos fiber (as the exothermic peak due to the release of heat at 830°C for chrysotile to determine the presence of talc [20] can be used to reveal the mineral contamination of asbestos. The same principle can be applied to IR and Raman spectroscopy; these techniques allow the identification of asbestos fibers thanks to the unique spectral signature at the difference – with the other techniques mentioned above – that it's possible to achieve both organic and inorganic information and reuse without destroy the sample.

1.4 TOXICITY OF THE FIBERS

At the beginning of the asbestos issue, these minerals were considered as a single substance. Their toxicity was explained on the basis of properties like the fibrous habit, the fiber dimensions, the aspect ratio and mineral composition. However, each of them failed to explain all the experimental data. Thus, the necessity to consider biochemical aspects as iron generated free radicals (ROS and RNS), durability and biopersistence – the capacity of asbestos fiber to remains into the lung – was investigated to explain the results. The knowledge evolved and now it is well clear that asbestos fibers are heterogeneous materials, i.e. there are several issues to consider, involving differences among their shape, their different crystallinity, chemical composition and dynamic phenomena occurring at the fiber surface. All these issues together play a role in the carcinogenicity of the asbestos. Moreover, it's now well accepted than the fiber surface plays a crucial role since the cells and tissues are directly in interaction with the surface of the fibers. Thus, the surface composition, the surface area, the active sites at the surface and the ions that might selectively leach from the fiber surface are important to study the *in vivo* effects of each type of fiber. To understand the cytotoxicity of the fibers, different physico-chemical and biochemical properties need to be explained.

1.4.1 FIBROUS HABIT

Once inhaled, asbestos fibers have different fates – see figure 4. They can be removed from the lung by phagocytosis; they can reach the alveolar region, migrate to the interstitium and remain into the pleura and/or undergo "frustrated phagocytosis" – phagocytosis can't be done totally because of the size of the fiber.

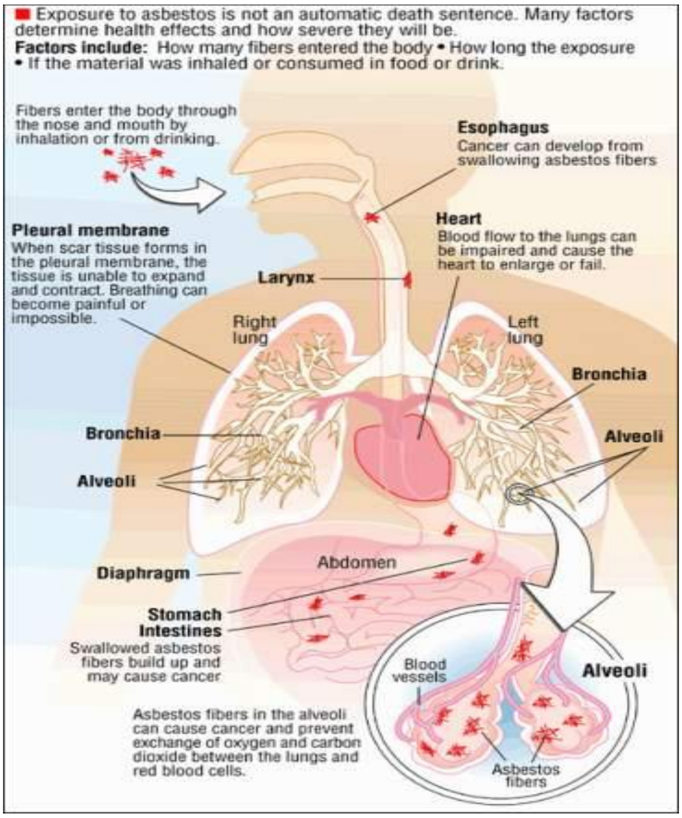

figure 4 :Asbestos fibers fates after exposure (developed by [21]).

After the fibers enter into the nose and mouth, they go through the esophagus - leading to cancer of esophagus. Once in the lung, they can go to the bronchia and alveoli space but also through the abdomen to the stomach intestines leading to diverse type of cancer.

Indeed the size of alveolar macrophages is not enough to ingest the long sized fibers [22]

Figure 5: Frustrated phagocytosis realized by macrophage (in yellow) on asbestos fiber (in white). The phagocytosis is said to be “frustrated” because macrophages cannot phagocyte the fiber [23].

Each fate depends on the shape and the dimensions of the fiber. Non-fibrous asbestos are well cleared from the lung. Serpentine fibers, as discussed above, can be disintegrated in small fragments by the pH of the lung that are ingested and cleared from the lung by phagocytosis. Amphiboles, into the lung are disassociated into unique long and thin fibers that penetrate into the epithelial cells. The IARC define a fiber as potentially carcinogen when the length is > 5µm and the aspect ratio >3:1 (with width <0.5µm) [24]. When the length is > 5µm, the phagocytosis can't be completed (figure 5) and the macrophage releases oxidants, enzymes of degradation and cytokines to call other macrophages and thus realized the phagocytosis. This releasing leads to a cascade of *in vivo* actions that induce mesothelioma. Thus, amphibole fibers are up to 500 times more powerful in causing mesothelioma than chrysotile fibers because of their typical dimensions and shape [25].

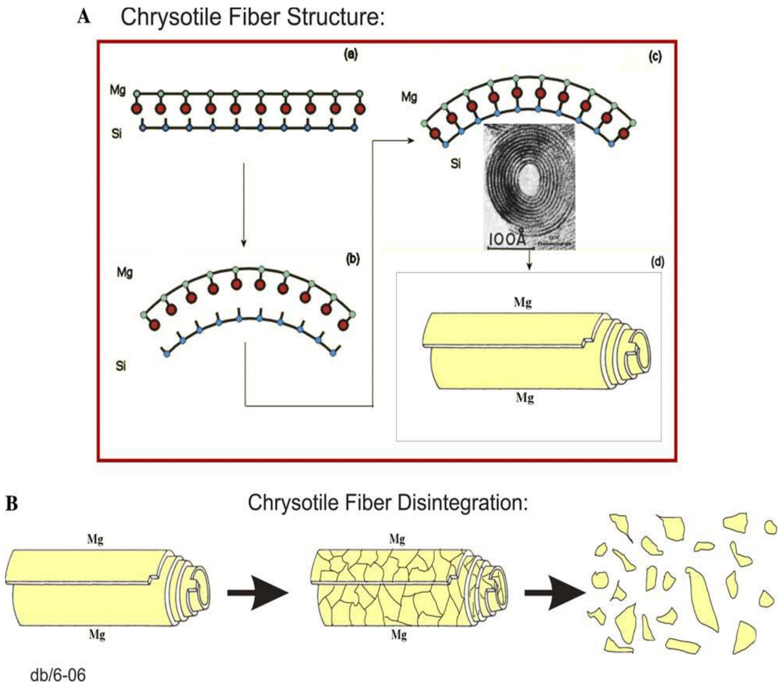

Figure 6: A: Schematic formation of chrysotile. The Mg layer and the Si layer are linked together the oxygen atom (in red) leading to the final rolled up structure.

B: chrysotile fiber disintegration. In mildly acid condition, the chrysotile fiber is disintegrated into small pieces that can be phagocyted [26].

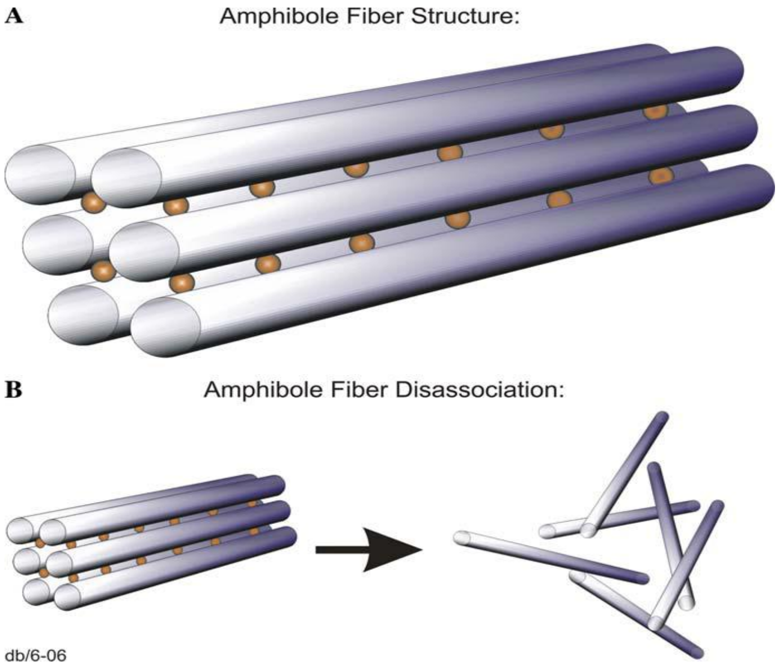

Figure 7: A: Schematic crystal structure of amphibole. The fiber are connected to each other thanks to oxygen atoms (in red)
B: amphibole fiber disassociation. In acid condition ($2<pH<5$), the oxygen bond is cut off leading to the dissociation of long and thin fiber into the lung [26].

1.4.2 GENERATION OF FREE RADICALS

Asbestos fibers can generate free radicals. The generation of these free radicals, due to the presence of iron on the fiber surface leads to the Reactive Oxygen Species (ROS) and Reactive Nitrogen Species (RNS) as $HO^{\bullet}$, H_2O_2, $O2^{\bullet-}$, $ONOO^{\bullet-}$ and NO. Thus, the surface of the fiber contains active sites that suggest a variation in the amount of free radical release, amount enhanced by the presence of chelatants that assisted to the iron release [27]. There are different mechanisms of generation of ROS. If there is H_2O_2 in the system the production of ROS is done through the Fenton reaction:

$$\mathrm{Fe\ (II)}_{(surface)} + H_2O_2 \rightarrow \mathrm{Fe(III)} + OH + HO^{\bullet}$$

As show by the reaction, the Fenton activity is insensitive to the redox state i.e. a change of the oxidation state of the atom, requires surface iron and is a catalytic surface site i.e. can be regenerated.

Thus, these reactions are consistent with prolonged effects *in vivo* and depend not only on the iron content but also upon the crystallographic structure. The knowledge of these reactions and the presence of active site on the fiber surface explain why biopersistence plays an important role in the cytotoxicity of the fibers.

Thanks to all the information collected, we are aware that the different types of fiber lead to the different effects depending on the various fibers dimensions, the fiber shape and the heterogeneity of the surface reactive sites. Thus, the pathogenicity is not related to a single feature but to a set of features, acting at different level and explaining why there is a range of diseases due to the inhalation of asbestos fibers.

1.5 PATHOLOGICAL PATHWAY OF ASBESTOS FIBERS

The pathological pathway of the asbestos fibers is a process that starts at the moment of the inhalation of the fibers to the damage of the target cells – epithelial and mesothelial – leading to the asbestosis or mesothelioma; the process is summarized in figure 8.

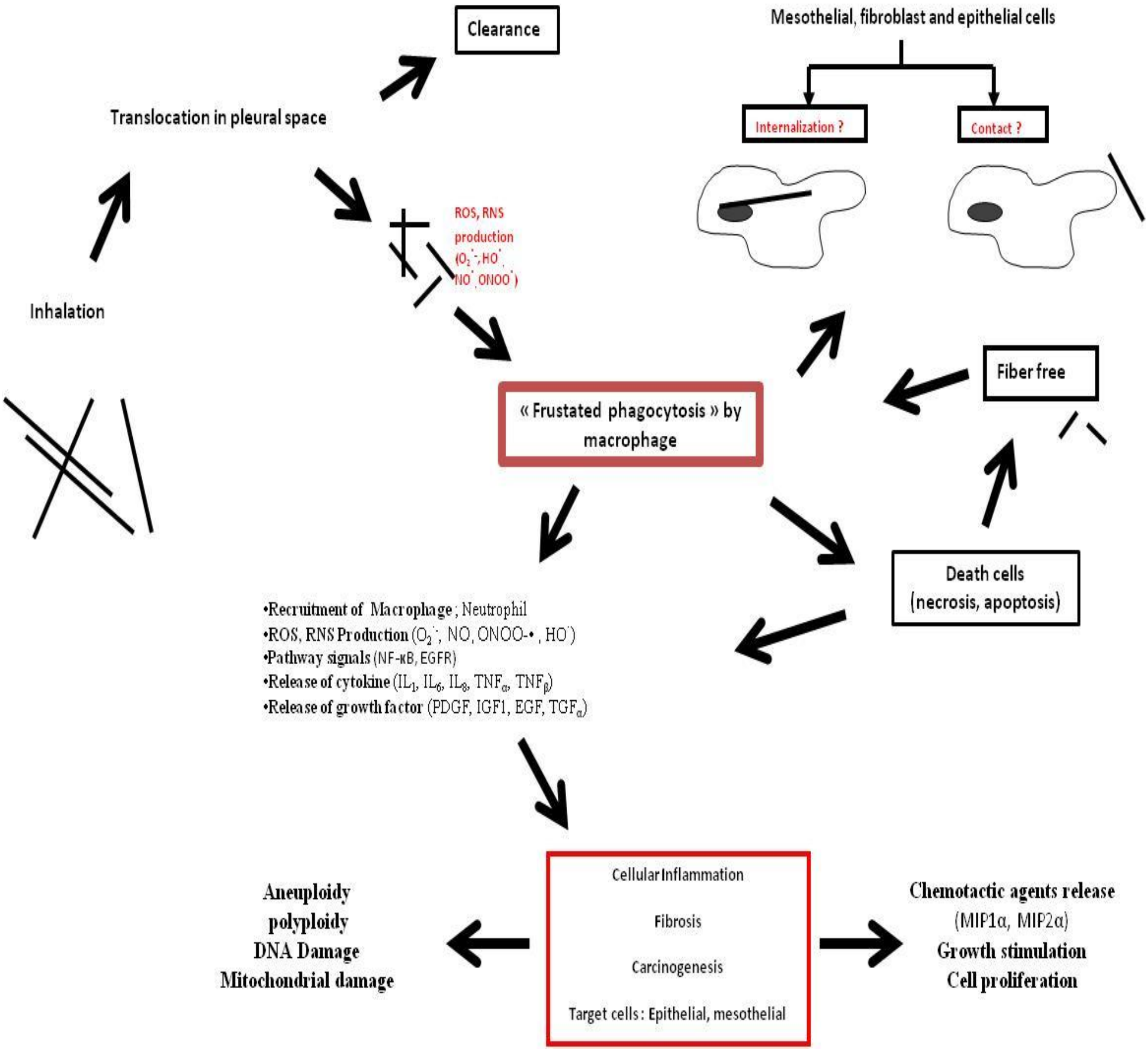

Figure 8: Hypothetical pathological pathway of asbestos carcinogenicity and their effects on cells. From the inhalation of the asbestos by the nose and mouth to the carcinogenicity of the target cells (mesothelioma, epithelial), including the frustrated phagocytosis. Adapted from [28].

Once inhaled into the lung, the asbestos dust can reach the alveolar region. Thus, pulmonary parenchymal cells, including alveolar macrophages, pulmonary epithelial cells, mesothelial cells, endothelial cells, and fibroblasts, are all susceptible to develop cell-fiber interactions with chemotoxic effects. Alveolar or interstitial macrophages represent the key elements in the development of fibrosis, the other inflammatory cells (T-lymphocytes, neutrophils, mast cells) being involved only as a second line. These macrophage-fibroblast interactions are established at two levels: 1- by the production of chemotactic factors, the macrophages participate in the recruitment of other cells; and 2- the multiplication of cells mediated by growth factors leading to the cell proliferation in the region involved. Since they are the first line in contact with asbestos fibers in the lung, epithelial cells from the alveolar epithelium have been the most studied. The aim of previous studies has been to observe the clearance of fibers, the effect of the fibers on cells (notably for type I and II alveolar epithelial cells). There has also been interest in the induction of inflammation as well as on the proliferation of these cells [29]. These recent studies used human lung epithelial (A549) cells. The other types of cells studied are the mesothelial cells (human mesothelial MeT 5A) [10].

The mechanism of asbestosis or the nature of asbestos carcinogenicity process may be described as follows:

- Fibers generate free radicals that damage cells and DNA. Indeed, asbestos induce DNA damage in two different ways, one associated with asbestos fibers in the cell and another one not depending on the presence of fibers. The latter could be due to iron release from the asbestos fibers or reactive oxygen species formed from iron contained in the fibers [10].
- Fibers stimulate proliferation of cells. Indeed, the alveolar macrophages due to the frustrated phagocytosis release also chemotactic agents like platelet-derived growth factor (PDGF), Transforming Growth Factor (TGF) and interleukin-1 (IL-1). These factors increase cell proliferation and stimulate extracellular matrix (ECM) production. They allow the detainment of sites of asbestos and finally to further macrophage accumulation. These chemotactic agents can recruit and activate inflammatory cells (neutrophils and lymphocytes) locally but also from the interstitial space, such as fibroblasts [11].
- Fibers induce chronic inflammation reaction-chain (release of ROS, cytokines, growth factors…etc.). Majors factors involved include IL-1, PDGF, insulin-like growth factor-1 (IGF-1) or tumor necrosis factor α (TNF-α). As an example, TNF-α exhibits powerful pro-inflammatory activity related both to induction of adhesion molecules on endothelium and epithelium surfaces and to the stimulation of other cytokines, notably chemokines, such as IL-8 [30].
- Physical action of fibers interferes with mitosis by troubling chromosome segregation, which results in abnormalities during the mitosis.

At the macrophage level, studies have shown that apoptosis of alveolar epithelial cells plays a significant role in the pathogenesis of lung disorders [14, 31]. Basically, apoptosis is the main way for reducing the hyperplasia in type II alveolar cells when a lung injury occurs. However, in the case of asbestosis, apoptosis may induce epithelial barrier dysfunction, further lung injury, and fibrosis [32]. Concerning DNA, chromosomal aberrations have been observed (aneuploidy, lagging, bridged, and sticky chromosomes). This is due to the accumulation of unphagocyted fibers in the perinuclear region of the cells [33]. The uptake of fibers by the cells is increased by adsorption of proteins at the fiber surface. At the genes level, gene expression is altered by the release of RNS and ROS, which induces cytotoxicity manifested by gene base substitutions, deletions, insertions, rearrangements, and sister chromatin exchanges [34, 35]. These molecular features of cell-fiber interactions appear as major issues for diagnosis and monitoring of asbestosis. Except the utilization of tissue biopsies for determining specifically given molecular parameters, several imaging methods have been applied to the diagnosis of this large and diffuse family of pathologies.

Today, no techniques allow a better overview of the toxicity issue of asbestos fibers. Spectroscopic techniques as Raman and IR spectroscopy are exploited all along this work together with toxicity techniques in order to determine morphological and chemical information of cellular response. This would permit to access details of the effective toxicity of asbestos fibers as well as information on the physical and chemical features of the interaction between asbestos fibers and epithelial lung cell at a molecular level with a sub cellular resolution.

2. IR SPECTROSCOPY

Fourier-Transform Infra Red (IR) spectroscopy is an analytical technique revealing the bonds between atoms. It helps the determination of the structure of molecules thanks to the intra molecular and inter-molecular vibrations occurring into the sample. Indeed the amount of IR radiation absorbed by the materials is measured as a function of the wavelength. Allowing the analysis in solid, liquid and gaseous phases, IR spectroscopy has been significantly used during the last 20 years in analytical chemistry thanks to the strong increase in the performance of the equipments.

2.1 PRINCIPLES

The energy domain of IR light is broad and can be divided into three sub domains: far-IR, mid-IR and near-IR. The domain where most vibrations of molecules are observed is the mid IR and corresponds to the wave numbers between 4000 cm^{-1} and 400 cm^{-1} – 2.5 to 25µm in wavelengths or $1.2*10^{13}$ to $1.2*10^{14}$ Hz in frequency. IR spectroscopy is based on the capacity of the apparatus to detect the vibrational transitions happening between two different vibrational energy levels in a molecule. It's important to understand that bonds in molecules react as a harmonic oscillator. Indeed, these bonds are elastic, can diverge in term of bonds lengths and angles from a mean position and vibrate at precise frequencies – frequency corresponding to the vibrational frequency and its environment of a chemical bond.

When hit by an IR light, an atom is excited by the energy of the photons and can move in the three dimensions of the space. When they are bonded together, because of its environment, a molecule can only translate and rotate into the space limiting the number of degrees of freedom:

$$3N-6 \text{ (non-linear molecule)}$$

$$3N-5 \text{ (linear molecule)}$$

where N is the number of atoms of the molecule.

There are different types of vibrations: symmetric and anti-symmetric. Moreover these vibrations can also be separated in stretching mode, ν (where the atom bond is stretched) and bending mode δ (where the molecule is deformed). Thus, symmetric stretching ν_s or anti-symmetric stretching ν_{as} can occur and the same for the bending mode – δ_s and δ_{as} – as shown below.

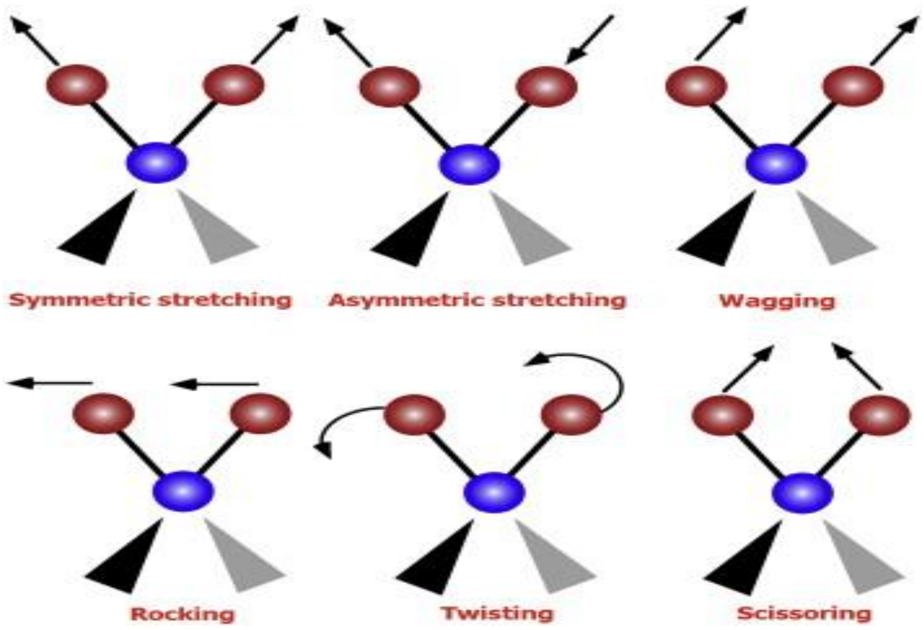

Figure 9: Different vibrational modes of a molecule. These others modes correspond to different bending occurring in complex molecule.

An IR absorption is correlated to the change of the electrical dipole moment. This makes impossible the IR detection of homonuclear molecules as O_2 or N_2 in contrast to heteronuclear molecules as H_2O or CO_2 that vibrate in the IR region with intense characteristic peaks.

2.2 INSTRUMENTATION

IR spectrophotometers consist of a source, a detector and an interferometer. Each will be discussed below.

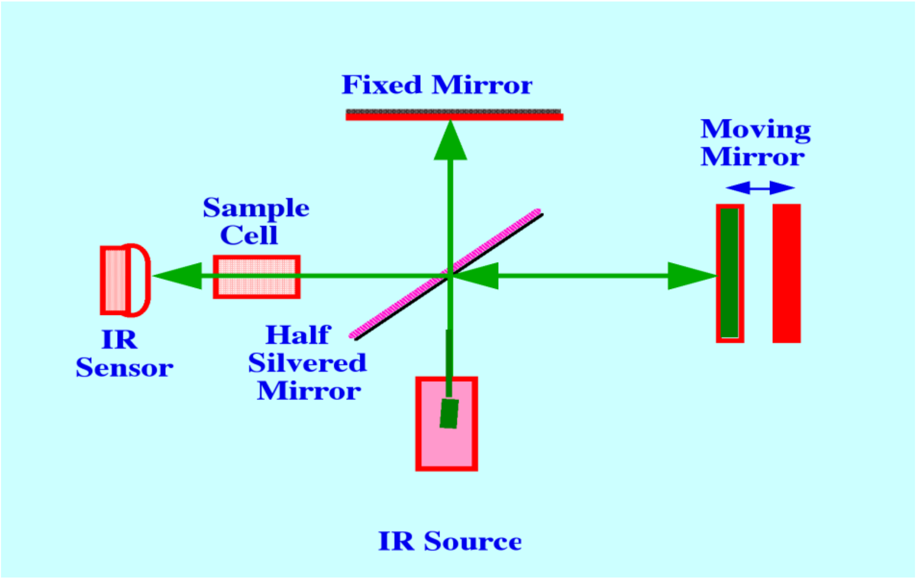

Figure 10: IR spectro-photometer with the interferometer of Michelson [36].

2.2.1 THE IR SOURCE

The most common IR source used in IR spectroscopy is the Globar. It’s a silicon carbide rod allowing a spot size of ≈ 100µm [37]**.** To increase the resolution of the spot, another type of source called the synchrotron IR radiation came into play in the recent years. This source allows a photon flux several orders of magnitude higher than the Globar source. However, due to the complexity and the cost of SR light, the use of Globar source is still widespread in the laboratory experiment.

2.2.2 THE INTERFEROMETER

The early dispersive spectrometers were based on the use of a monochromator. This permitted the scan of each wavenumber separately i.e. each point of the spectrum was recorded distinctively. These spectrometers were extremely slow. The type of spectrometer used nowadays is the Fourier transform interferometer. Combined with a suitable detector, it allows a better sensitivity and a faster scan speed based on the recording of the whole wavenumber range simultaneously. The interferometer allows a difference of optical path by a game of reflection and transmission of the light from the source leading to the achievement of an interferogram.

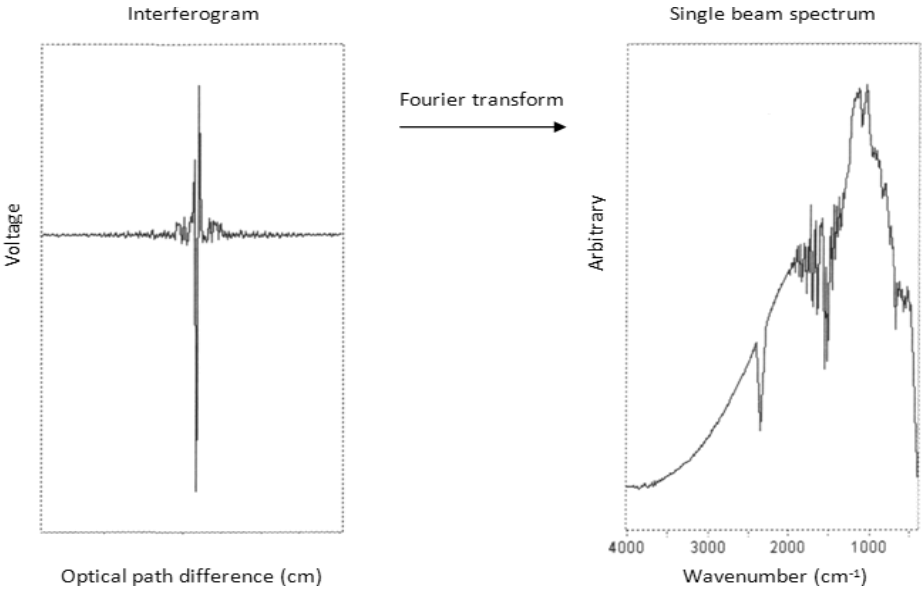

Figure 11: The interferogram and the single spectrum obtained by Fourier transformation [38].

Thus, the interferogram is a measurement of the temporal coherence of the light at each different time delay setting [38]. The application of the Fourier transformation on the interferogram obtained, permits to resolve it into a sum of sinusoidal functions, corresponding respectively to a wavenumber. The frequency and the amplitude of each of them are calculated from the interferogram. The reference is a helium neon laser with the same optical pathway than the source and used as internal calibration.

2.2.3 THE DETECTOR

Two type of detectors are usually used in the mid IR region: 1- the DLaTGS detector – deuterated l-alanine-doped triglycine sulfate – allowing to work at room temperature with a great stability and ease to use, and 2- the MCT – Mercury Cadmium Telluride – having a higher sensitivity but requiring to be cooled with liquid N_2.

Recent developments of IR microscope detectors including the Focal Plane Array – FPA – have decreased the acquisition time of experiments by collecting 4096 spectra at the same time. These IR multichannel detectors or arrays are based on the collection of data by small individual detectors – pixels – allowing a simultaneous and very rapid spectral mapping on large area [39]. The FPA detectors permit to analyze a 1 mm^2 sample area at the microscopic resolution in few minutes instead of hours with single element detector to obtain a similar spectral quality but also to reduce the instabilities due to the changes of the experimental condition [39, 40]. Moreover, the development of the number of arrays from 8*8 elements to 128*128 elements allows a better lateral resolution. Indeed, the dimensions of individual detectors are 40*40 µm and with the use of magnification level of microscope's objective – 4x, 15× or 36× it is possible to obtain a final pixel resolution of 10*10, 2.6*2.6 or 1*1 µm respectively [37]. The final pixel resolution of 1*1 µm allows the study of single cells by IR imaging in laboratory despite the problem of the weak photon flux of the Globar source.

It is important to note that the most critical factor defining image fidelity is the lateral resolution. Diffraction of light happens when the size of an optical device, placed in the path of the light beam, is smaller than the beam diameter. Thus, any types of optical microscopy are restricted by the inherent low spatial resolution called diffraction limit. This diffraction limit is correlated to the wavelength and the size of the aperture through the equation 1 [41]:

$$\Delta x = 0.61 * \frac{\lambda}{n \sin\theta}$$

(eq.1)

Where Δx correspond to the distance between two objects, λ the wavelength and $n \sin\theta$ is the numerical aperture (N.A.) of the objective with n the refractive index of the medium between the objective and the specimen and θ the acceptance angle of the objective [42]. It is obvious that objects can be seen by mid IR light – 4000cm^{-1} to 900cm^{-1} – if they are spaced between 2.5µm and 10 µm. The resolution can be reduced by others minors factors as mirror, detector geometry, objective, detector response…. Moreover, the diffraction limit is a concept that can be overcome by using ATR IR devices [43]. Indeed, by collecting the evanescent wave on the surface of a substrate with specific properties, it’s possible to obtain information on objects smaller than 0.5µm, which would challenge the principle of Rayleigh criterion (two points can be separated when the central maximum of the first Airy disc is placed at a distance of just one radius) and thus the principle of lateral spatial resolution [44].

Thus, the use of the FPA detectors with the IR interferometer leads to the acquisition of a spectroscopic image in a time similar to the acquisition of a single spectrum, in conventional mode. Utilization of synchrotron radiation provides a high brightness over a small size spot, an increase of SNR and a fast measurement, thus allowing the study of molecular change occurring in single cell. By coupling the multichannel detection of FPA detectors with the spectral multiplexing advantage of FTIR interferometry, the field of view of an entire sample is spectroscopically imaged in a time period faster than to acquiring a single spectrum conventionally but with a better SNR.

2.3 APPLICATIONS

First used in material science for characterizing and analyzing chemical species, IR was developed for biological applications during the second half of the 20th century thanks to the development of computers. First used for the analysis of simple biomolecule, IR spectroscopy and then IR imaging with the availability of FPA detectors, made possible the examination of more complex biosystems. Thanks to the development of statistical theories for data treatment, it was possible to extract information on specific molecular components and their changes from their spectra [45]. Thus, the IR imaging technique made possible to access to the internal organization, elemental or molecular distribution from complex biosystems such as bacteria [46], cells [47], tissues, and model biosystems such as membranes [48] or vesicles [49].

For inhomogeneous and complex biosamples, such as cells or tissues, with different molecular and structural components, each vibrating molecule absorbing within the mid-IR region : nucleic acids, osidic residues, lipids, and proteins contribute to the whole spectra. These different molecules have overlapping absorptions modes, which make challenging the assignment of IR bands to particular molecular components [39]. However, relevant spectral regions as lipids (3050 cm^{-1} – 2800 cm^{-1}), proteins (1700 cm^{-1} – 1480 cm^{-1}) and osidic residues (1200 cm^{-1} – 900 cm^{-1}) can be highlighted. From these regions, there are also pertinent bands: the amide I and the amide II vibrational bands between 1700 and 1480 cm^{-1}; lipids absorptions modes around 2900 cm–1 and DNA, RNA vibrational band at 1705 and 1610 cm^{-1} and osidic residues around 1000 cm^{-1}. Thus, it’s possible to obtain the distribution of molecular components of interest, for example protein or lipids, by integrating the proper bands over the scanned region.

The development of infrared applications in the biological field allowed to obtain a large qualitative and quantitative database and thus to determine the structural composition in a vibrational spectrum as shown in the table below.

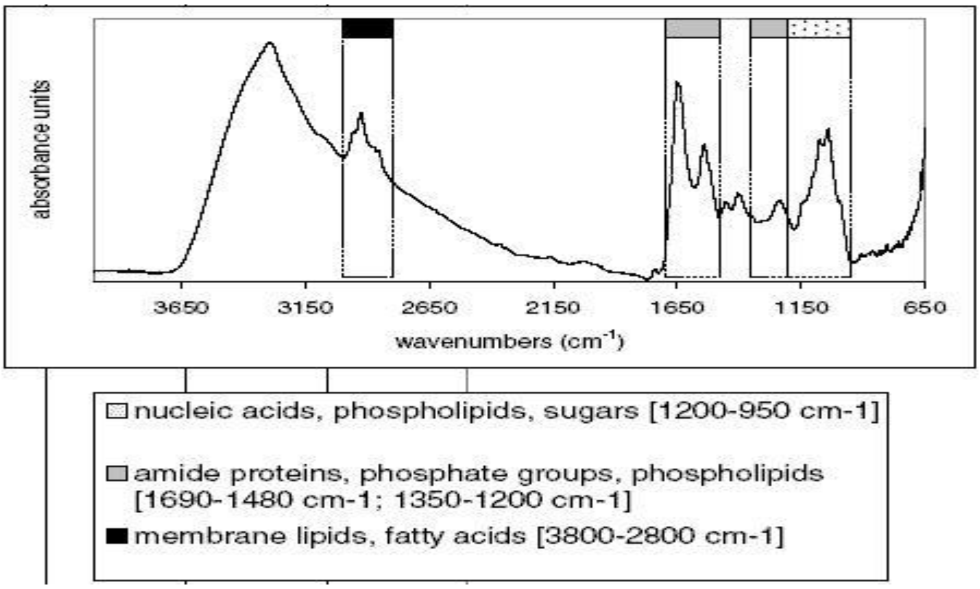

Typical Mid IR spectrum of cell [50] with the spectral region of interest and their meaning peaks assignments of cellular spectra [51]

Wavenumber (cm^{-1})	Assignment
3328	Amide A (ν -N-H), proteins
3129	Amide B (ν -N-H), proteins
3015	ν =C-H, lipids
2960	ν as -CH_3, lipids proteins
2920	ν as -CH_3, lipids proteins
2875	ν s -CH_3, lipids proteins
2850	ν s –CH_2, lipids proteins
1720-1745	ν –C=O, lipids (esters)
1710-1716	ν as –C=O, RNA (esters)
1705-1690	ν as –C=O, RNA, DNA
1654	Amide I ν -C=O (80%), ν - C-N (10%), δ -N-H (10%), α-helix
1630-1640	Amide I ν -C=O (80%), ν - C-N (10%), δ -N-H (10%), β-structure
1610, 1578	ν -C4-C5, ν -C=N, imidazole ring, DNA, RNA
1515	Aromatic tyrosine ring (Lasch et al)
1540-1550	Amide II δ -N-H (60%), ν - C-N (40%), α-helix
1530	Amide II δ -N-H (60%), ν - C-N (40%), β-structure
1467	δ –CH_2 lipids, proteins
1455	δ as –CH_3 / -CH_2 scissoring lipids, proteins
1370-1400	ν -COO^-, δ s –CH_3 lipids, proteins
1330-1200	Amide III, proteins
1230-1244	ν as –PO_2^-, RNA, DNA
1160, 1120	ν -C-O, RNA ribose
1170, 1070	ν as, ν s –CO-O-C, lipids
1090-1084	ν s –PO_2^-, RNA, DNA
1060, 1050	ν –C-O, deoxyribose/ribose DNA, RNA
996	RNA stretch and bend ring of uracyl
965	symmetric PO_4^- stretch (DNA) and deoxyribose-phosphate skeletal motions

In the same way, samples containing asbestos fibers have been investigated by IR spectroscopy. Schematically, the relevant absorption bands are located in the 3600-3700 cm^{-1} range (specific hydroxyl bands), the 600-800 and 900-1200 cm^{-1} ranges (specific Si-O-Si bands) [52]. Moreover, the IR study of each type of fiber allows to discover differences in spectra between them and provides the opportunity to identify the different species.

Vibrations	Chrysotile	Anthophyllite	Amosite	Crocidolite	Tremolite	Actinolite
O-H Stretching	3680 (s)	3668 (vs)	3640 (w)	3630 (vw)	3670 (vs)	3670 (vs)
	3640 (w/m)		3620 (w)	3620 (w)	3650 (w)	3650 (w/m)
			3610 (w)	3610 (w)		
Si-O stretching	**1075 (s)**	1085 (m)	1120 (m)	1135 (m)	**1100 (vs)**	**1094 (vs)**
	1020 (s)	1010 (s)	**1075 (s)**	**1100 (s)**	1060 (s)	**1050 (s)**
	950 (vs)	970 (m)	990 (s)	**985 (vs)**	995 (s)	1035 (s)
			885 (w)	**970 (vs)**	940 (s)	1010 (s)
				890 (w)	920 (s)	985 (vs)
				870 (w)		948 (s)
						914 (s)
Silicate chain and ring vibrations		775 (w/m)	765 (w)	770 (m)	755 (m/s)	755 (m)
		750 (w)	695 (w)	685 (m)	680 (m/s)	727 (w)
		705 (w)	630 (w)	630 (m)	660 (w/m)	682 (m)
		665 (m)			635 (w/m)	658 (w)
						645 (w)
Cation-oxygen stretching	600 (s)	480 (s)	490 (m)	535 (m)	500 (m/s)	540 (s)
	430 (vs)	440 (s)	475 (s)	495 (m)	455 (vs)	507 (vs)
	400 (s)	420 (m)	418 (s)	435 (vs)	440 (vs)	475 (vs)
	295 (m/s)	385 (m)	365 (w)	350 (w)	395 (w/m)	465 (vs)
		360 (w)	345 (w)	310 (m)	385 (w/m)	450 (vs)
			325 (w)		355 (w/m)	

Table 2 : Principal IR absorptions peaks and their assignments for asbestos minerals [53] (in cm^{-1}).(s) strong ; (m) medium; (w) weak; (vs) very strong. In red the IR peaks characteristic of each asbestos fiber.

Working on single cells implies the analysis of low amount of biological material and thus the measurement of spectra with low signal. Moreover, it was show that coupling IR imaging with SR radiation leads to a higher sensitivity and spatial resolution. Thus, the exploitation of the SR-IR signal made possible the extraction of qualitative information from biological samples.

Not all the intense IR bands characteristic of asbestos fibers can be used for the identification when working with biological materials. Indeed, the IR bands of biological objects are extremely more intense than those of the fibers. This explains the difficulty of using IR spectroscopy in the study of the interaction between cells and asbestos fibers and our inability to visualize the IR image of the fiber when we realize IR representation of the interaction because of the biological group.

Thus, we decided to use Raman spectroscopy as an additional technique to obtain images of the interaction of fibers with lung cells. Thanks to the achievement of spectrum with sharp and narrow bands, Raman spectroscopy allows to better differentiate the organic vs. inorganic elements. Moreover, the spectra can be collected in aqueous medium which leads to access to in vitro information of the interaction. So, the use of Raman spectroscopy is susceptible to bring out new information and on the work and that why we decide to employ Raman spectroscopy.

3. RAMAN SCATTERING

3.1 THEORY AND PRINCIPLES

Raman Spectroscopy, as IR spectroscopy, probes vibration mode of molecules. Once the electromagnetic radiation is emitted, a material can absorb, emit or scatter the photon. Thus, a beam of radiation from a source such as a laser is passed through a sample, and the radiation leaving the sample is captured. There are different types of scattering, the elastic scattering or Rayleigh scattering that occurs when the scattered radiation has the same wavelength i.e. the same energy that the incident light and the inelastic scattering or Raman scattering which is described by a difference of frequency of the exiting light due to a difference of the vibrational energy of the sample. Discovered in 1929 by Sir C.V. Raman, the Raman Effect is the inelastic scattering of a photon because of a change in the photon energy. Stable at the ground electronic state, an atom hits by a laser light is excited and reach to a higher level of energy. Then the energy is brought back down and emitted a photon. 1 in 10^6 of the incident photons is scattered inelastically.

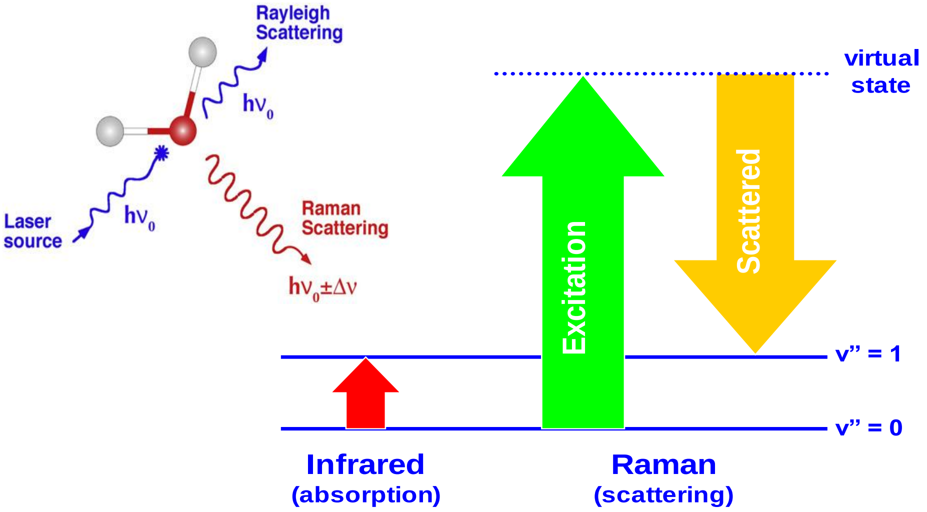

Figure 12: light scattering processes with a simple molecule: Rayleigh scattering (blue) and anti- Raman scattering (red) and the electronic state for each process.

Moreover, if an atom is at a given energy level, it can be excited and fall below the original level. Thus, there are two vibrational energies of the inelastic scattered light: the Stokes and anti-Stokes mode. In Stokes scattering, the laser light induces a vibration in the bond and after the scattering process, the photon is in a higher vibrational energy state and the scattered energy is decreased. In anti Stokes scattering, the scattered photon gains energy and the material remains at a lower electronic state (see figure 13).

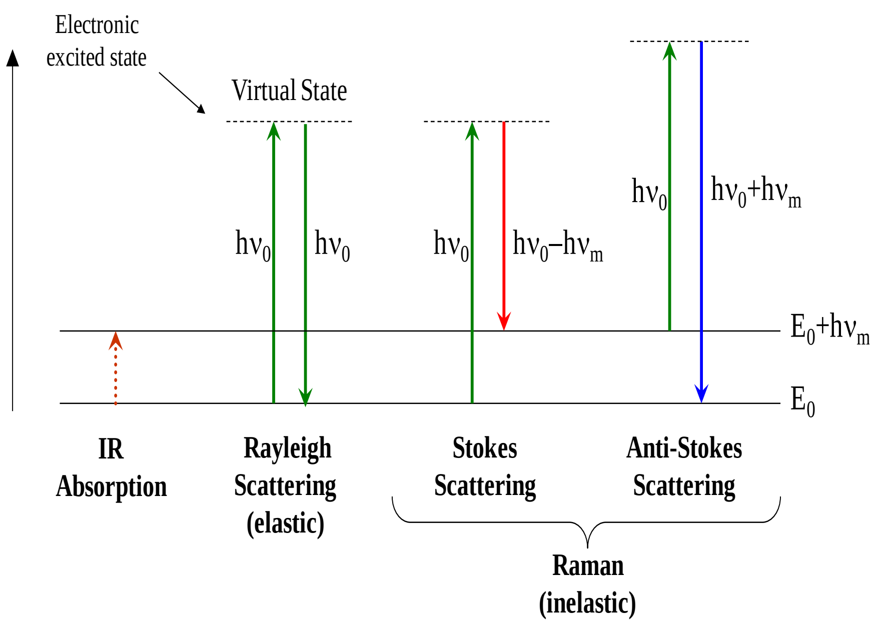

Figure 13: The Raman scattering process. Stokes scattering: the chemical bond absorbs energy and the emitted photon has less energy than the absorbed photon; anti-Stokes scattering: the atom loses energy and the emitted photon has more energy than the absorbed photon.

Being an electromagnetic radiation, the light interact (by its electric component) with the molecular vibration modes and induce a polarization of the bond [54] given by the equation 2:

$$\alpha(Q) = \alpha_0 + \left(\frac{\partial \alpha}{\partial Q}\right) \qquad \textbf{(Eq.2)} \qquad \text{with} \quad Q = Q_0 \cos \omega_{vib}\, t \ \text{and} \left(\frac{\partial \alpha}{\partial Q}\right) \neq 0 \qquad \textbf{(Eq.3)}$$

Where α is the polarizability, Q is the motion of a vibration mode, Q_0 the vibration mode at the initial state t and ω_{vib} the vibration frequency of the molecule.

That leads to the creation of an induced oscillating dipole moment represented by the equation 4:

$$\vec{p}(t) = \alpha \vec{E_i}(t) \quad \text{with} \quad \vec{E_i}(t) = \vec{E_0} \cos \omega_0 t \qquad \textbf{(Eq.4)}$$

Where $\vec{p}$ is the polarization and $\vec{E_i}$ the electric field.

If α change when the molecule vibrates, the polarization leads to the equation 5:

$$\vec{p}(t) = \alpha(Q) \vec{E_i}(t) \qquad \textbf{(Eq.5)}$$

$$\vec{p}(t) = \left(\alpha_0 + \left(\frac{\partial \alpha}{\partial Q}\right) Q_0 \cos \omega_{vib} t\right) \vec{E_0} \cos \omega_0 t \qquad \textbf{(Eq.6)}$$

$$\vec{p}(t) = \alpha_0 \vec{E_0} \cos \omega_0 t + \left(\frac{\partial \alpha}{\partial Q}\right) \frac{Q_0 \vec{E_0}}{2} \{\cos[(\omega_0 + \omega_{vib})t] + \cos[(\omega_0 - \omega_{vib})t] \qquad \textbf{(Eq.7)}$$

$$\vec{p}(t) = \vec{p}(\omega_0) + \vec{p}(\omega_0 + \omega_{vib}) + \vec{p}(\omega_0 - \omega_{vib}) \qquad \textbf{(Eq.8)}$$

Equation (2) explains why, a change in the molecular polarizability of the sample is required to be able to measure the Raman Effect on a sample. This change is reflected by a change in either the magnitude or the direction of the polarizability ellipsoid of the molecule i.e. $\left(\frac{\partial \alpha}{\partial Q}\right) \neq 0$. In general, for molecule with a center of symmetry, no active IR transitions are Raman active; and for non linear symmetric molecules, all the modes are IR and Raman active.

Equation (8) shows that the oscillating dipole will reradiate at the same frequency than the applied field $\vec{p}(\omega_0)$ which is the definition of the Rayleigh scattering and creates two others frequencies of radiation: 1- the Stokes scattering has the form of $\vec{p}(\omega_0 - \omega_{vib})$ and occurs for the negative wavenumbers – if the laser radiation is set to zero – and 2- the anti-Stokes scattering illustrated by the term $\vec{p}(\omega_0 + \omega_{vib})$ and will have positive wavenumbers.

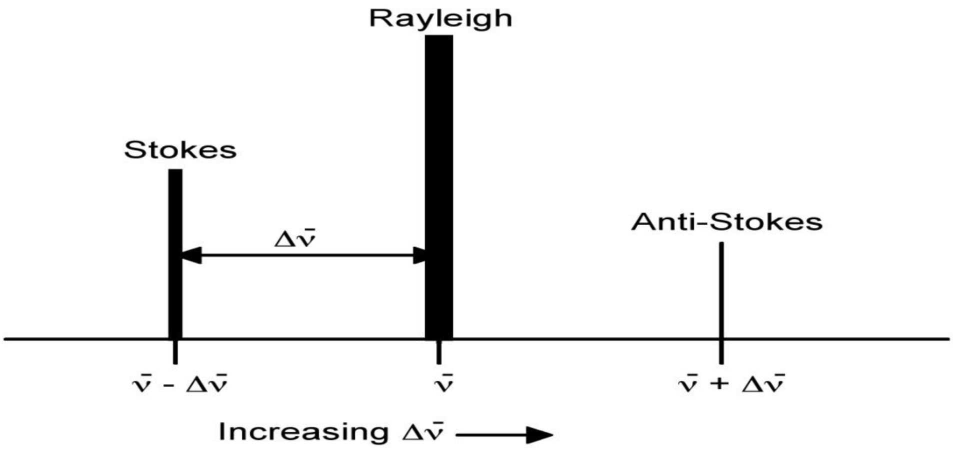

Figure 14: Position and relative intensity of stokes and anti-stokes scattering relative to Rayleigh scattering.

Another way of showing the Raman spectrum is to set to zero the incident frequency to the characteristic frequency of the silicon (ν (Si) = 520.7 cm^{-1}). This allows a better calibration of the system since the frequency shift is the most important parameter for acquisition. Because of the difference of intensities between stokes and anti stokes peaks (the difference can be revealed by the quantum mechanics equation of the distribution of phonon), only the Stokes peaks are represented in the positive shift.

3.2 INSTRUMENTATION

The Raman spectroscopy set up is based on five essential components, a monochromatic sources (ie a laser), an appropriate arrangement of the sample (see section 4.2), an analyzer for the scattered light which may either be a spectrometer or a spectrograph , a device for converting photons into electrical signals, and a control unit for data acquisition.

Nowadays, compact Raman spectrometer systems are available in which all these components are integrated. Such system offers the advantages and disadvantages of typical “fully operating “systems: they are easy to handle but cannot readily be modified, such that they are difficult to adapt to non standard applications. Each part will be described below.

3.2.1 THE SOURCE

Thanks to their good SNR and their high intensities, the laser sources are now in Raman systems instead of mercury arc and high power gas lasers (e.g. Ar^+). Raman signal needs a high intensity from the source to be able to measure the signal at low levels since only 1 photon over 10^6 is scattered and collected.

The intensity of the Raman scattering is given by the formula (4):

$$I_S = \frac{8\pi^4\alpha^2}{\lambda^4 r^2}(1+\cos^2\theta)I_o \quad \text{(Eq 9)}$$

Where I_s represents the scattered intensity, I_0 the incident intensity, α the polarizability of the particle, λ the wavelength of the incident radiation, θ the angle incident and r the distance from center of scattering to detector [54].

Consequently, the intensity of Raman varies as the fourth power of the frequency – $f = \frac{1}{\lambda}$, so the sources emitting in the blue and green region (argon – 488 or 514nm – or krypton – 530.9 or 647.1nm – laser source) are the most advantageous for Raman studies. Thus, in our lab, we used for experimentations the Witec apparatus that combined Confocal Raman spectroscopy, Atomic force and Scanning Near-field Optical microscope with a 532 nm excitation laser source. Thanks to the use of laser light, the practical diffraction limit, which is on the order of the excitation wavelength, is about 10 – fold smaller for Raman spectroscopy than for mid - IR spectroscopy. In our case, the diffraction limit is around 250nm at 532nm – with an NA of 1.4 for the objective – and a lateral resolution of 90nm. There is also the possibility to use three types of fibers with 25, 50 and 100 nm core diameter, allowing reducing the resolution. However, the use of these sources induces high fluorescence signal and is harmful for the biosamples. Indeed, the heat of the laser beam focusing on a very small area of the sample and the absorption of cellular component as proteins or nucleic acids lead to the photodecomposition of the sample [55]. It is probably possible to overcome this limit by using a good sample amplifier and a fast scan to reduce the fluorescence and the degradation of the sample induced by UV ionization.

3.2.2 THE DETECTOR

Detectors sensitivity is based on the fact that Raman scattered radiation emits in the visible or the near IR region. There is two different technologies to detect the Raman Effect: the Fourier Transform Raman (FT-Raman) and the dispersive Raman. As we work with a dispersive Raman detector, we will describe the theory below.

Dispersive detector is based on polychromatic detection. The principle consists in the use of a long wavelength excitation laser passing through the sample, and after the Raman signal is focused on a grating. This grating permits to divide the radiation into the different frequencies – the dispersed beam. Then, the beam is collected by a multichannel two dimensional CCD detector and connected to a computer that transformed the light obtained into specific wavelengths.

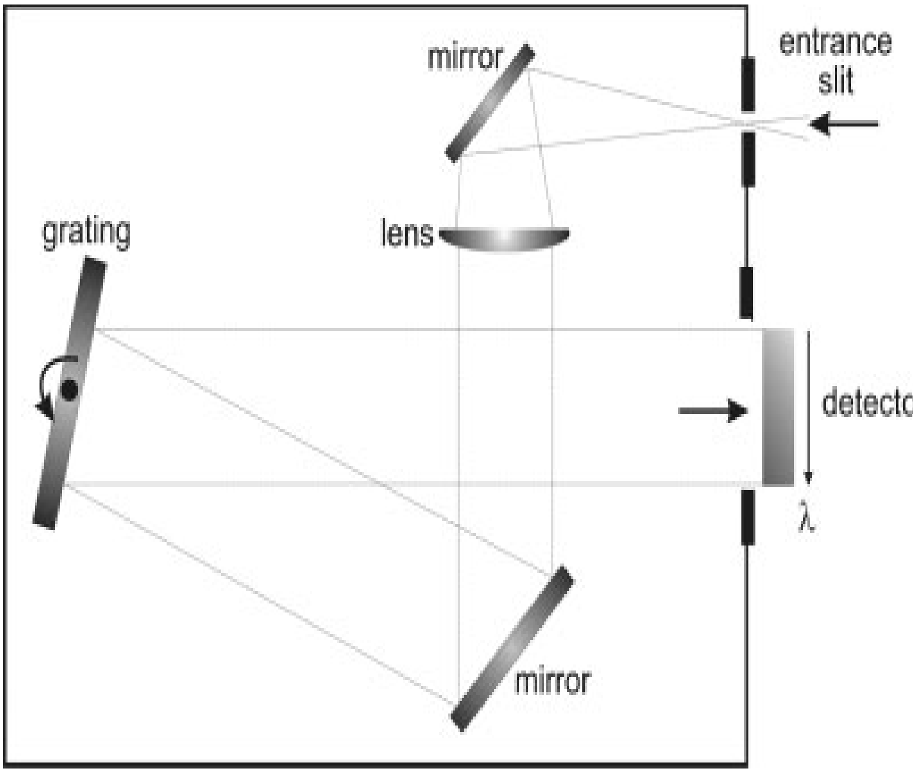

Figure 15 : Optical principle of dispersive Raman detection. The laser light is dispersed onto a grating composed of photoactive arrays that are positioned into the focal plane of the spectrograph leading to the detection of each frequency [56].

Taking into account the typical size of a CCD array with a length of around 25 mm including more or less 1000 individual photoactive elements, the wavenumber increment per pixel at 500 nm is 0.5 cm^{-1} and the total range to be covered is 500 cm^{-1}. Then, besides the constraints due to the spectral slit width, in principle, bands can be resolved that are separated by at least three pixels which, in the present example, corresponds to 1.5 cm^{-1} [56]. The size of the spectral range that is covered by the CCD array increases with decreasing number of grooves of the grating, such that the choice of the grating is a trade-off between spectral coverage and spectral resolution. The sensitivity of gratings and detectors used in the polychromatic detection mode exhibits distinct wavelength dependence as explain in theory and principles section. Thus, during our work, the scattered light is collected by an objective lens of 300mm of focal length that permits the dispersion grating of the light into the thermoelectrically cooled CCD detector by one of the dual grating; 1800 and 600 lines / mm @ 500nm leading to a spectral window for detection from 150cm^{-1} to 4000cm^{-1}.

3.2.3 CONFOCAL SPECTROMETERS

Several Raman micro spectrometers employ confocal optics, which provide the capability to produce images of thick samples at various depths. The exciting laser beam is focused onto the sample via a microscope objective, which simultaneously serves to collect the scattered light in the backscattering configuration (Figure 16)

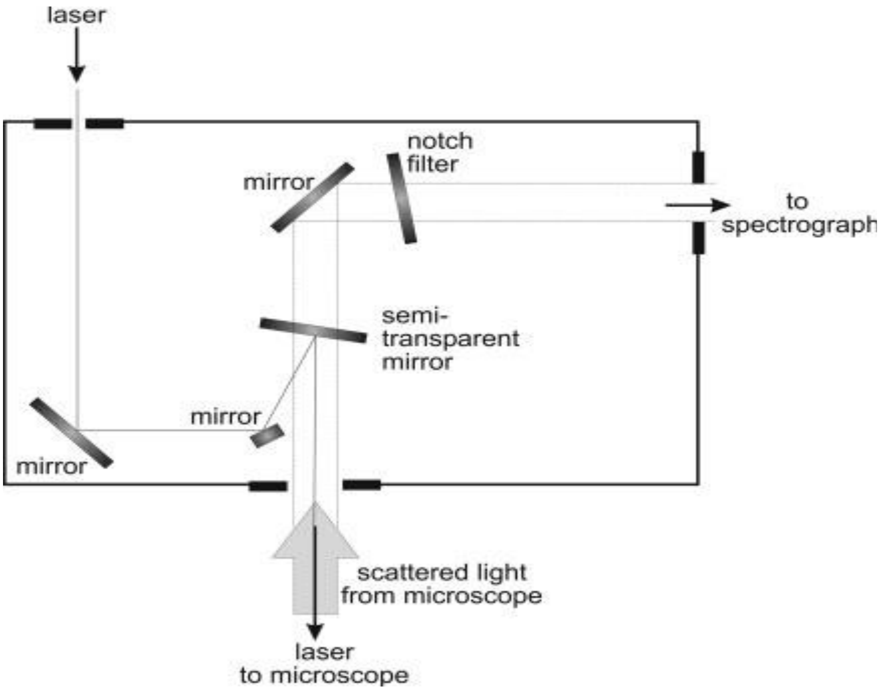

Figure 16: **Schematic optical principle of a confocal spectrometer**. The laser is focused onto the sample via a microscope objective, which in turn also collects the scattered light. The reflected laser light and the Rayleigh light is removed from the scattered light by a notch filter prior to entering the spectrograph stage [56].

There is a special design to perform the confocality in Raman (micro) spectrometry. In such a design (see Figure 17) the laser beam is first focused on a small aperture (to clean up the beam profile and present a diffraction - limited source), and then refocused by an objective lens with a large numerical aperture onto a small (ideally diffraction - limited) focal volume within the sample. A mixture of the Raman - and Rayleigh - scattered light from the illuminated spot is then collected by the objective lens. The high NA of these optics allows the light to be collected over a solid angle of almost a full hemisphere. I.e. An objective with a NA of 0.95 collects about 70% of the radiation emitted.

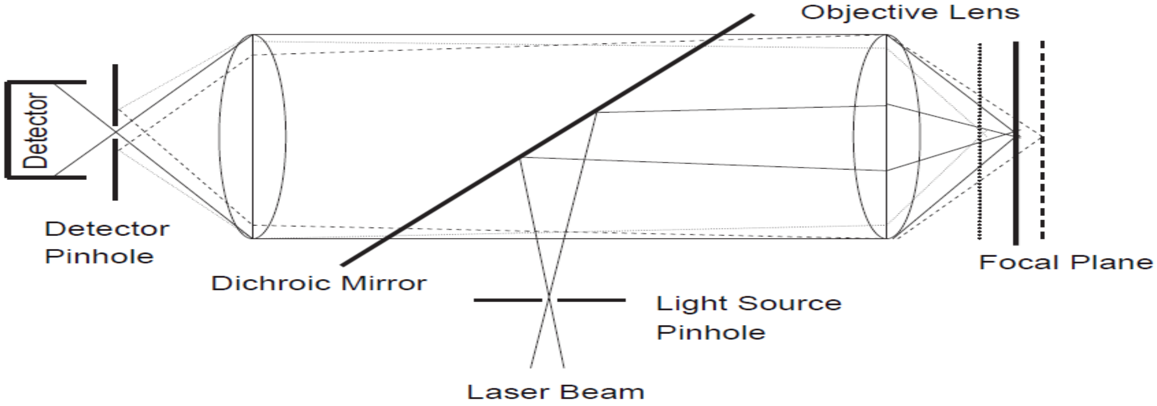

Figure 17: **Schematic representation of the optics of a confocal microscope.** The detector pinhole obstructs the so - called out - of- focus (or out - of - plane) light, i.e. light from adjacent spatial regions and fluorescent emission not originating from the focal plane of the objective lens. Light rays from below the focal plane come to a focus before reaching the detector pinhole, and then expand out so that most of the rays are physically blocked from reaching the detector by the pinhole. In the same way, light from above the focal plane is focused behind the detector pinhole, and is not detected. However, all the light from the illuminated focus (solid lines) is imaged at the pinhole and passed to the detector [57].

The detected light originating from an illuminated volume element within the specimen is then focused and permits the mapping of the entire specimen by moving the sample by small amounts after each spectrum has been recorded. For Raman mapping measurements, the readout time per pixel must be very short. For example, if an image consisting of 128 pixels per line and 128 lines is acquired with an integration time of 1 s per pixel, then the total acquisition time will be a little over 4.5 h. Reducing the readout time to 100 ms per pixel decreases the measurement time to 27 min. A further 10 - fold reduction in the readout rate decreases the acquisition time to less than 3 min. Thus, our Raman spectrometer allows us to perform 3D mapping of 100 µm section by acquiring an entire spectrum in be less than 1 ms, which allows Raman mapping of over 10 000 spectra in less than one minute when the Raman signal is adequate.

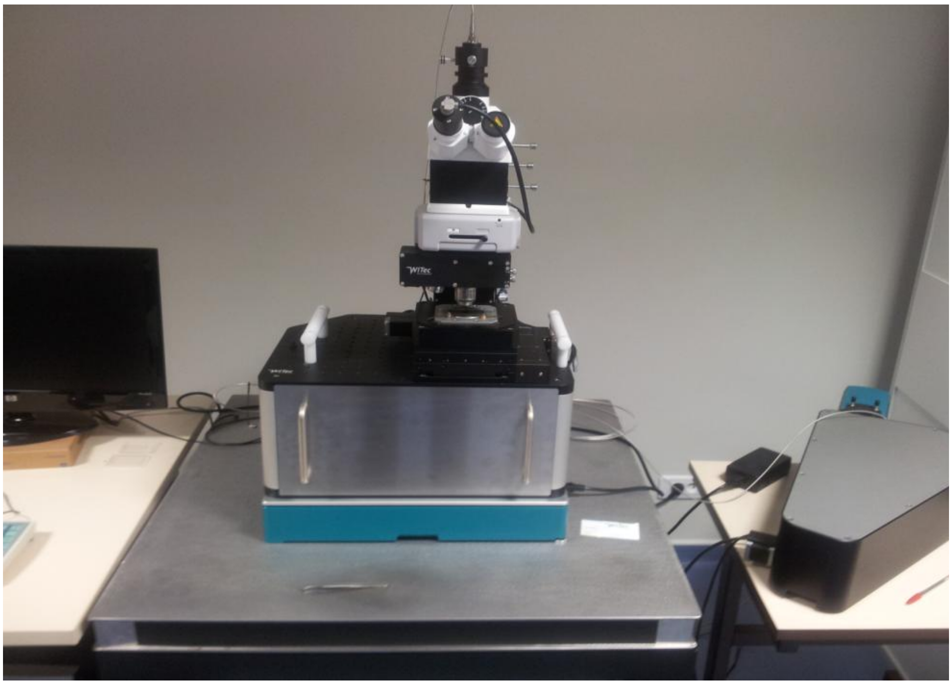

Image of the Confocal Raman Microscope from Witec

3.3 APPLICATIONS ON SAMPLE

3.3.1 INORGANIC SAMPLES

Raman spectroscopy is able to work into aqueous medium, this allowing to analyze inorganic samples. Indeed, thanks to his aptitude to offer information as composition, structure or stability of coordination compounds, Raman scattering is widespread in material science as super and semiconductors, carbon-based materials, oxides, glasses …[58]. An example of use is the detection of vibrational energies of metal-ligands bonds – between 100cm^{-1} and 700cm^{-1} – active in Raman and well observed but difficult to extract in IR [59].

Moreover, considering 1- the absence of sample preparation; 2- the high chemical specificity since narrow bands are obtained and 3- the access to qualitative information, as led to apply Raman spectroscopy to the analysis of asbestos species to determine and differentiate each fibers types in microscopic quantities on the basis of their chemical composition [60, 61].

This permitted the detection of functional groups and fingerprint regions for each type of fiber, thus leading to the identification of different species. All these information are grouped in the table below

Asbestos fibers	Si-bridging O -Si stretching	Non bridging O - Si stretching	Si-O-Si deformation	Cation-oxygen stretching	O-H Stretching
Amosite	1093 (vw)	1020 (s)	506 (w)	421 (m)	3656
	658 (vs)	968 (m)		401 (m)	3639
	555 (vw)	903 (vw)		364 (m)	3623
	528 (m)			349 (m)	
				309 (w)	
				287 (w)	
Anthophyllite	**671 (vs)**	1042 (m)		430 (m)	3674
				410 (w)	
				384 (m)	
				362 (m)	
				336 (vw)	
				304 (m)	
				260	
Chrysotile	1105 (vw)			465 (m)	3700
	692 (vs)			432 (vw)	3685 (sh)
	623 (w)			389 (vs)	
				345 (s)	
				321 (vw)	
				304 (vw)	
Crocidolite	1085 (s)	969 (vs)	509 (w)	469 (m)	3637
	1032 (m)	891 (s)		374 (vs)	3685
	664 (s)	772 (m)		332 (m)	
	577 (vs)	737 (m)		297 (s)	
	539 (vs)			249 (s)	
				271	
Tremolite	1061 (m)	928 (w)		414 (w)	3677
	1028 (m)			393 (m)	
	672 (vs)			369 (m)	
				349 (vw)	
				251 (w)	
				222 (w)	
				232 (w)	

Figure 18: Asbestos Fibers Identification by Raman Micro-spectroscopy [61] (in cm^{-1}). (s)

strong; (m) medium; (w) weak; (v) very; (sh) shoulder. The table shows that each asbestos fiber has specific bands in the low frequency region: 671 cm^{-1} for anthophyllite, 692 cm^{-1} for chrysotile, 577 cm^{-1} or 664 cm^{-1} for crocidolite and 672 cm^{-1} for tremolite corresponding to the Si-O-Si stretching modes. Bands can be used as markers during imaging work to differentiate the species

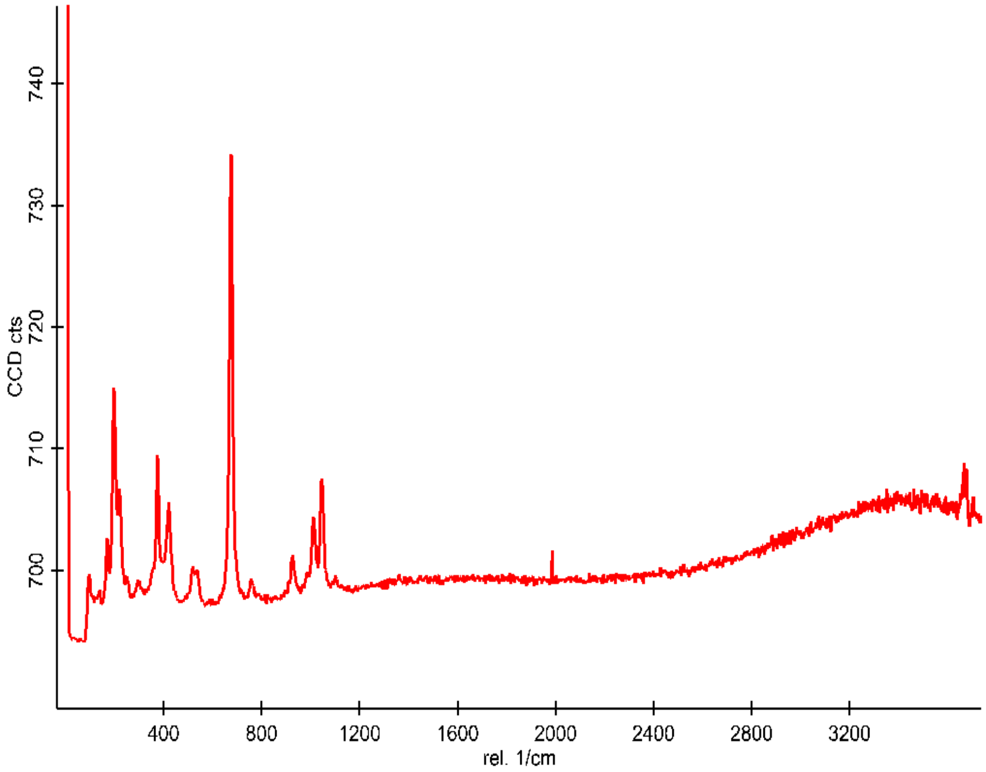

Raman spectrum of a tremolite fiber

3.3.2 ORGANIC SAMPLE

In addition to the advantages described above, Raman spectroscopy was extended to the biomedical field because of its capacity to image and obtained spectra of cells– so combining qualitative morphological information of the sample. Moreover, it’s possible to access the biochemical composition and metabolic states of a single cell without using labels or dyes; showing the length scale of the technique, which is comparable to that of the confocal fluorescence microscopy or other optical techniques [62, 63].

Thus, different types of cells were investigated by Raman spectroscopy and the determination of the fingerprint regions has been evaluated. Consequently, the identification of the Raman signal of cell sub compartments were determined and mostly due to the contribution of DNA and proteins for nucleus and proteins and metabolites as sugars signals for cytoplasm [64].The assignment of the

Raman peaks for cellular compounds has been well investigated and can be summarized in the table below.

Wavenumber (cm^{-1})	Assignment
3070	Amide B (CNH bend)
2960	CH_3 stretch (antisymmetric) due to methyl terminal of membrane phospholipids
2936	CH_3 stretch
2928	CH_2 antisymmetric stretch of Methylene group of membrane phospholipids
2886	CH_2 stretch (symmetric) due to methylene groups of membrane phospholipids
2854	CH_2 stretch
2739	CH stretch
1736	C=O stretch
1667, 1640	Amide I (protein) C=O stretching of amide coupled to NH_2 in-plane bending
1657, 1659	C=C stretch (lipids), Amide I (α-helix, protein)
1611	Tyr (aromatics)
1566	Phe, Trp (phenyl, aromatics)
1550	Amide II absorption due to N-H bending coupled to a C-N stretch
1509	C=C stretch (aromatics)
1452	CH_2 stretch deformation of methylene group (lipids)
1439	CH_2 def.
1420	CH_3 asymmetric stretch (lipids, aromatics)
1397	CH_3 bending due to methyl bond in the membrane
1382	COO^- symmetric stretch
1367	CH_3 symmetric stretch
1336	Adenine, Phenylalanine, CH deformation
1304	Lipids CH_2 twist, protein amide III band, adenine, cytosine
1267	Amide III (α-helix, protein)
1250	Amide III (β-sheet, protein)
1235	Antisymmetric phosphate stretching
1206	C-C stretch, C-H bend
1165	C-O stretch, COH bend
1130	C-C asymmetric stretch
1100, 1094, 1081	PO_2^- symmetric stretch (nucleic acids)
1065	Chain C-C
1056	RNA ribose C-O vibration
1003	Phenylalanine (ring-breathing)
967	C-C and C-N stretch PO_3^{2-} stretch (DNA)
957	CH_3 deformation (lipid, protein)
936	C-C residue α-helix
921	C-C stretch proline
898	C-C stretch residue
870	C-DNA
853	Ring breathing Tyr – C-C stretch proline

828, 833	Out of plane breathing Tyr; PO_2^- asymmetric stretch DNA (B-form)
807	A-DNA
786	DNA – RNA (PO_2^-) symmetric stretching
746	Thymine
727	Adenine

Table 3 : Raman spectroscopy peaks assignment for cells compartments [51].

As explained for the asbestos fibers, a correct assignment of the peak observed for lipids, DNA and RNA provides a rapid method to identify these components. Thus, the development of Raman spectroscopy as a tool in biological research is important in a range of application as the analysis of chemical composition of cells and the search for specific markers, the macromolecules interaction – DNA / protein – or the determination of molecular markers of disease as cancer in the early stages of its development [65].

Thanks to its non invasiveness, label free and ability to provide high spatially resolved image, several groups have tried to analyze *in vitro* the chemical changes from single living cells using Raman spectroscopy. Their studies are mainly based on the change of proportions of nucleic acid and proteins [66, 67]; or the difference of distribution of macromolecule [68]. In general, some of them worked using fixed [69] cells as reference for the study but it became impossible to monitor a biological process over the time and be sure that the change is not due to the fixation method [70, 71]. Others work with living cell but by using SERS [72, 73] and CARS techniques [74] with a laser source in red region (to avoid heat of the cell of interest), they lose spectral information. Working with SERS allows a 10 fold increase of the Raman signal without regards on the necessity and the difficulty of sampling and the growth of cell on metallic surface. Only one group [75] has studied the cell response to a chemotherapy drug treatment at single cell level using living cell and 532nm laser source and analyzed chemically the spectral difference in RNA and DNA region by using Raman micros spectrometry (spectral region of interest between 800 and 1800cm^{-1}) but they have oversampling and the signal level is three fold better with us. Thus, at this point of the study, no one has been able to perform safe 3D Raman spectra of a single living cell using Raman spectroscopy and obtain morphological and chemical information on them. Beforehand, an upstream work is necessary. The right condition of growth cells, the intensity of the laser and other experimental conditions as the scan velocity must be found prior to realize the image as the scattering signal is weak and the biological material can be degraded.

Thus, the Raman spectroscopy is potentially a powerful technique to investigate the interaction of cell – asbestos fibers because of its aptitude to provide both organic and inorganic information. Moreover, the possibility to work in aqueous solution allows the investigation of living cells. Since the spatial resolution is better than the IR one, the use of the Raman spectroscopy will permit to investigate the vibration as the IR spectroscopy but also obtain a better spatial characterization of the sample. Another reason is the complementarity between IR and Raman spectroscopy since a bond inactive in Raman is active in the IR and vice versa. So these techniques can be combined to elucidate analytical and toxical issues and have information of the interaction by looking at the interface organic / inorganic species. IR technique will be most useful to determine modification for protein and osidic residues spectral regions when Raman will be used to access nucleic acid and lipids modification.

4. PROBLEMATIC

The asbestos fibers are known to have a carcinogenic effect on human leading to diseases such as asbestosis, or mesothelioma. At present, there are no technological resources able to fully characterize the interaction asbestos fibers / cell for understanding the pathogenicity of these fibers at the cellular and sub-cellular levels. In this work, we developed new Raman and IR imaging techniques to investigate the interaction between asbestos fibers and lung cells to determine the pathological pathways of fibers.

The goal of using IR spectroscopy is to obtain cellular response information at a molecular level. It's also a very fast technique that requires no or little sample preparation. In addition, the achievement of spectral information can be done in few minutes. Therefore, chemical information can be extracted and when working with biosamples, a biochemical fingerprint of the specimen is obtained allowing ultimately to access features indicative of the cell state such as cell proliferation, apoptosis, differentiation etc… Indeed IR imaging has already proved his ability to achieve information in the protein and lipid regions. The data, when treated with multivariate analysis allow the determination of markers for cancer purpose. Due to its ability to perform experiment in solution and determine extracellular and intracellular modification occurring on living cells, Raman spectroscopy brings complementary information.

Thus the aim of the study will be the development of IR and Raman spectroscopic methods to investigate the toxicity of asbestos fibers on lung cells *ex vivo* and *in vitro*. The results will be coupled with biological assays used to evaluate the toxicology profile of the fiber to complete the spectroscopic measurements. The goal is to show how IR and Raman technique can overcome disadvantages of other toxicological assays and bring out valuable responses of the problem. The first step of the study, as shown in chapter 4, is the determination of the best substrate for spectroscopic measurement. To do this, the HCMEC cells were grown on different types of substrate as PbF_2, CaF_2 or Si… and the samples were measured using synchrotron radiation to evaluate which substrate allows the best SNR and integration for each spectral region. On the basis of the preliminary results the next step of the study was done with the best substrates thanks to the analyses of the data using multivariate analysis. Thus, the effects of different types of asbestos fibers on lung cells were investigated using firstly IR imaging (chapter 5). Coupled with biological tests as colorimetric methods, the difference in IR spectra was evaluated and elucidated for the protein and lipids regions. This study allowed us an attempt to determine the spectroscopic features due to the presence of asbestos fibers in the systems. Chapter 6 will be an example of application of IR imaging using SR radiation, while in the chapter 7 we describe is the living cell behavior when they interact with asbestos fibers. For this last step, Raman spectroscopy methods were developed. Thanks to the spatial resolution of the method in the two dimensions, the localization and the spectroscopic features of the asbestos fibers could be elucidated.

In summary, during the work of this thesis, spectroscopic methods were developed and tested to couple inorganic information with organic data in order to establish the effective value of these spectroscopic techniques to characterize the interaction of fibers with cells. According to these methods, morphological and chemical parameters were thus investigated to determine the carcinogenic effect of the asbestos fibers.

5. MATERIALS AND METHODS

5.1 SUBSTRATES FOR CELL IMAGING

The choice of a substrate for spectroscopic studies is a critical point to plan and perform the experiments. The good substrate should have a good biocompatibility and a good adhesion to allow a good attachment of the cells. In the same time, it must have an insignificant or well-defined contribution in the spectrum to provide the highest signal-to-noise ratio (SNR) on IR image spectra of a cell. Thus, we performed several tests aimed at defining which substrates, with different spectral windows and characteristics, among **Si_3N_4, Ge, GLS, LaF_3, Si, SrF_2, ZnS/C, ZnS/F, PbF_2, $PbCl_2$, diamond, AgCl, CaF2** was suitable for cell culture conditions comparable to those observed when using polycarbonate petri dishes and offer the best performance the IR and Raman spectroscopy work. It is important to note that the direct cell culture on the substrate may have an influence on their chemical content and morphology [51, 76] so it's important to choose a substrate that can minimizes this contribution. At the end of the study which is fully described and explained in chapter 5, we selected **Si** wafers to perform the spectroscopic work.

5.2 CELL LINE

We selected the cell line A549 cell line (CCL-185, from American Type Culture Collection) for this project aimed at studying the interaction between asbestos fibers and lung cells. The A549 is a cell line coming from a Caucasian carcinoma human alveolar basal epithelial cell, widely used as in vitro model for a type II pulmonary epithelial cell of the epithelial barrier for drug metabolism and the pulmonary toxicity induced by external agent as nanoparticles and biochemical toxins [77]. With dimensions from 35 to 70 µm they are anchored to the culture flask in a solution in vitro; they are also squamous and grow as monolayers and adherent cells as shown in figure 19.

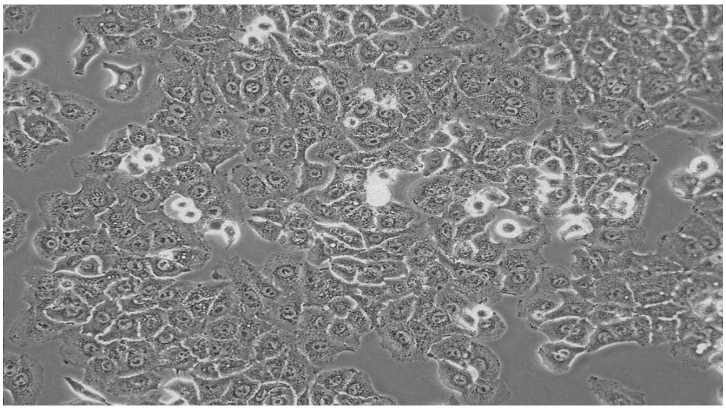

Figure 19: Microscopic image of A549 alveolar epithelial type II cells [78]

5.3 CELL CULTURES

Cells were grown in a Dulbecco's Modified minimum Essential Medium (DMEM)/F-12 medium supplemented with 10% fetal calf serum, 1 g/L of glucose, glutamine, HEPES and antibiotics. Cells were routinely propagated in a humidified 5 % CO_2 atmosphere at 37°C. Serum-free culture was performed according to Barnes *et al* [76]. The serum-free medium consists of a basal medium supplemented with 25 µg/mL HDL, 5 µg/ml insulin, 5 µg/mL transferrin, 2 ng/mL EGF, 1 mg/mL f-BSA and antibiotics

5.4 ASBESTOS FIBERS

Three natural asbestos fibers were used for this work; all samples were selected from the collection of the "Museum National d'Histoire Naturelle" of Paris. The first one is a "crocidolite" from Buchanawald (South Africa), labeled MNHN 134-86. Wavelength-dispersive microprobe analysis (WDS-EMP) gave a composition in the riebeckite compositional field, according the recent accepted nomenclature schemes for amphiboles [79, 80]. Deviations from the end-member composition involved weak amounts of TiO_2, MgO, MnO and K. Both F and Cl were below the detection limit, thus suggesting an anionic composition equals to $(OH)_2$. The second is a cummingtonite, labeled MNHN 137.96; EMP data showed this sample to be very rich in Mn, with a composition actually close to the species mangano-cummingtonite ($Mn_2Mg_5Si_8O_{22}OH_2$). The third fibrous amphibole is an actinolite, labeled MNHN 104.624, with an intermediate Mg/Fe composition with respect to end-member tremolite.

Scanning electron microscopy (SEM) showed all samples to consist of very to extremely fibrous crystals, as it is typically the case of "crocidolite" from South Africa, which has an average dimensions < 1.0 µm in width (average 400-500 nm) and typically > 10 µm in length (and up to several tenths of µm). Before the experiments, the fibers were ground in a mechanical milling machine equipped with a micro agata mortar and baked at 250-300°C overnight to avoid chemical and/or biological contaminations due to handling procedures or from the environment. The amphibole powders were suspended in the cell medium and sonicated (Labsonic, 100 W, B. Braun Biotech International) for 5 minutes before each experiment.

5.5 CELL CRYOFIXATION TECHNIQUES

Most of the methods used for the cell imaging by IR suffer by the necessity to perform cell fixation with PFA or methanol – to remove the water contribution from the sample, and this may modify the chemical and morphological features of the cell. Thus, a dedicated cell- culture method has been developed such as to provide : 1- cells on IR- transparent substrates with their extracellular matrix, 2- cells adhesion on the substrate without adhesion matrix as collagen , 3- cells morphology maintained all along the process. To obtain these features, cells grown on Si-support for IR imaging measurements were prepared as follows: after sterilization (24h bath in ethanol + UV radiation for 15 minutes), the Si-supports were placed in 6 wells plates. 30 000 cells with cell medium were added to each well with the suitable amount of fibers. The cryofixation has been done 24 hours later following the method described by Petibois and al. [81]. Briefly, Si-plates were removed from wells and washed twice with PBS to remove culture medium components before to be placed in sterile tubes and plunged in liquid-N_2. Cells were further dehydrated in freeze chamber with laminar flux of dry air for a slow (12h) freeze-drying.

5.6 COLORIMETRIC ASSAY

The cytotoxicity of each type of fiber and concentration was investigated by 3-(4, 5-dimethylthiazol-2-yl)-2, 5-diphenyl tetrazolium bromide (MTT). It's an alternative method for rapidly and indirectly determining cell viability based on metabolic activity. The test measures the conversion of MTT to insoluble formazan by dehydrogenase enzymes of the intact mitochondria of living cells. A549 cells were seeded at a density of 5.10^3 cells / well into 96-well micro plates for 24h. After treatment with the different concentrations of fibers for 24h, the medium was removed and 200 µl of MTT (Sigma) solution (5 mg/ml in PBS) were added to the plates and incubated for 3 h at 37 °C. After a centrifugation at 2000 rpm for 10 minutes, the liquid was removed and the formazan crystals were dissolved in 200 µl of DMSO (Sigma) for 30 minutes. The amount of formazan crystals formed correlates directly with the number of viable cells. Optical density (OD) was measured at 570 nm (reference filter 690 nm) using a UV-spectrofluorometer. Controls were grown in culture medium without treatments; their absorbance values were taken as reference values. Results were analyzed and expressed as percentage of the control (control equals 100%). Mean values of relative viability ± standard deviation (s.d.) were considered for statistical evaluations [82].

5.7 EXPERIMENTAL MEASUREMENT CONDITIONS

5.7.1 IR IMAGING SETUP

Different IR imaging setup has been used during the different studies presented above. The common conditions are the use of the Bruker Hyperion 3000 microscope equipped with a 64x64 focal plane array (FPA) detector coupled to a IR spectrometer (Bruker Equinox 55, Germany) for the optical and IR images. IR spectra acquisitions were performed in transmission mode, using a 8 cm^{-1} spectral resolution. A Blackman-Harris three-term apodization and a zero-filling factor of 2 were applied before Fourier transformation of each spectrum. N_2 purge was performed on both the microscope and the spectrometer for ensuring optimal spectra acquisitions by removing absorption from the atmosphere and the plexiglass box (on the front of IR microscope) filled for better N_2 purge effectiveness. The spectra were recorded without a normalization process. The baseline was corrected manually and reconstructed to pass through the two side points of the main regions of interest. A nine point smoothing were applied and then, the spectral regions area were integrated according to the chosen abscissa limits (in cm^{-1}) as described previously [83]. The difference of setup for each study is described below.

5.7.2 SUBSTRATE STUDY

Optical and IR images were realized using a Globar source (Ø ~ 1 mm). IR spectra acquisitions were performed coadding 256 scans (4000-900 cm^{-1}). Individual cells were analyzed in triplicate per window with magnification level set at 15X (reconstructed image has pixel size of ~2.6x2.6 µm – see figure 4). From every 2D image, an average of 10*10 spectra corresponding to nucleus location was extracted and averaged. Then, integration of amides I (1720-1600 cm^{-1}) and II (1600-1490 cm^{-1}) absorption bands were performed using sub-routines of Opus 6.5 software (Bruker Germany).

5.7.3 ASBESTOS FIBER INTERACTION STUDY

The IR spectrometer was illuminated by a synchrotron radiation IR source (Ø ~ 35 µm) as described elsewhere [44]. IR spectra acquisitions were done co-adding 128 scans (4000-900 cm^{-1}). Individual cells were analyzed in triplicate per window with the magnification level sets at 36X (the final IR image has a pixel size of about ~1.1x1.1 µm). From each 2D image, the spectrum with higher signal level at amide spectral interval corresponding to the nucleus location was extracted. Then the integration of absorption from lipids (3000-2850 cm^{-1}), amides I (1720-1600 cm^{-1}) and II (1600-1490 cm^{-1}) bands were performed. Amide II / I ratio was further calculated.

5.7.4 RAMAN SPECTROSCOPY SETUP

Raman spectroscopy was achieved using a 532 nm excitation source and a grating of 600 lines / mm at 500nm. The experiments were conducted with a water immersion objective of 63x with a numerical aperture of 1.0. To protect the objective lens and perform long acquisitions spectra, medium cell were removed and replaced before the experiments by PBS with glucose at room temperature. Spectra were acquired using 70*70 (points per line*line per image) sample area for the XY mapping with a scan speed for tracing of 14 s/line and an integration time of 0.2 s. For Z-stack images, the number of layers was determined to obtain a final difference of 800nm between layers. The spectral range was from 0 to 4000 cm^{-1} which allows the study of the main fingerprint regions of the biosample. Before analyzing the data, a pre-processing study has been performed thanks to the software Witec Project 2.06 (Witec, Germany). The baseline was subtracted from each mapping with a polynomial of order 0 for a constant offset, and the Si substrate peaks were removed from the whole spectrum. Then Savitsky-Golay filter of order 3 with eight smoothing point was applied to reduce the electronic noise from the signal. Multivariate analyses were performed further on the modified data. The same procedure was done on all XY mapping of this project.

5.8 STATISTICAL STUDIES

In spectroscopy analysis, Spectrum can be explained as a two dimensional variation in intensity in the Y-direction and an induced variation in the X-direction leading to an X-Y table. The recorded spectra contain chemical features and others particularities which usually come from constant physical effects occurring during the measurement. Thus, spectra can be described as the sum of the intended and the unintended contributions to the data. The desired information in spectra is extracting by investigating peak intensities, shoulder formation, peak shapes and their modifications due to external agents as stress condition. Indeed, the undesired contribution as electronic noise, baseline or substrate subtraction should be attenuate thanks to the use of appropriate preprocessing methods. Unfortunately, the evident information contained in spectra corresponds to absorption zones which are located at multiple spectral regions and usually overlap. As example, changes occurring in the state of cells or tissues are resulting from a complex effect that is revealed by a number of dependant or independent features. Moreover, due to the high molecular content of cells, the corresponding spectra are intricate convolutions of the vibrational signatures of each component. Therefore, multivariate analysis is necessary to be able to analyze and extract the information of interest. Depending on the method used, multivariable analysis - which takes each spectral absorption as variable - can show an elaborate view of the overall response, a classification between different experimental conditions and also bring out spectral absorption for the characterization of biophysical effects. The statistical methods used during this work are explained below.

5.8.1 MATRIX OF CORRELATION

Technically, a correlation matrix allows determining any type of relationship between several series of variables. It's essentially used to large series of data with many dependant and independent parameters to find out the covariables, i.e. variables with the same statistical meaning. There are several correlation coefficients, often denoted ρ or r, measuring the degree of similarity or dissimilarity between two elements. The most common of these coefficients capable of measuring similarities between two elements in the matrix is the Pearson correlation coefficient (p). It is obtained by dividing the covariance of the two variables by the product of their standard deviations which is sensitive only to a linear relationship between two. Thus, the higher the absolute value of p value, the more correlated the data are.

5.8.2 PRINCIPAL COMPONENT REGRESSION

Principal components regression is a technique based on the regression analysis. It means that the aim is the relationship between a dependent variable (for example integration value) and one or more independent variables (=absorptions). The advantage on a simple regression technique is that the principal components regression also handles the problem of multicollinearity (see chapter 5.8.1) and produce stable estimates for regression coefficients. To realize it, the method is to combine first a PCA (Principal Components Analysis - see chapter 5.8.3) on the table of the explanatory variables to reduce the number of variable and then perform a linear regression of the selected components. Thus, the parameters of the model that correspond to the input variables can be compute and presented in charts.

As PCR is build on PCA, a great advantage of PCR regression over classical regression is the available charts that describe the data structure. Thanks to the correlation and loading plots it is easy to study the relationship among the variables. There can be relationships among the explanatory variables, as well as between explanatory and dependent variables. Indeed, PCR gives the value of each parameter with its standard deviation and the value of the t-student test. A variable is significant when the p value greater than $|t|$ is less than 0.01%. The score plot gives information about sample proximity and dataset structure. The biplot gather all these information in one chart allowing the access to the most relevant parameters describing the study.

5.8.3 PRINCIPAL COMPONENT ANALYSIS

It's a method used for datasets with multiple dimensions. It leads to the reduction of the number of variables in the dataset and retains most important variables. To allow the reduction, p variables (X1,…, Xp), which are wavelength in spectroscopic studies, are combined lineary to produce principal componants (PCs) – also call **eigenvectors**. These PCs must not be correlated to each other to explain the different dimensions found in the dataset. Each succeeding component will account for progressively smaller amounts of variance. Thus the highest variation is shown for PC1 and so on. Although a large number of components may be extracted in this way, only the first few components will be important enough to be retained for interpretation. Therefore, the goal is to reduce the data to a small number of eigenvector that explain the largest variance in the data.

Experimentally, after the determination of the spectral regions of interest (650cm^{-1} – 710cm $^{-1}$ and 2820 cm^{-1} – 3020cm^{-1}), we proceed to the determination of the number of PCs with meaningful amount of variance to extract. To do it Witec software will provide the eigenvalues plot from the analysis of a dataset of a 70*70 XY mapping of cell. An **eigenvalue** represents the amount of variance that is accounted for by a given component i.e. a PC.

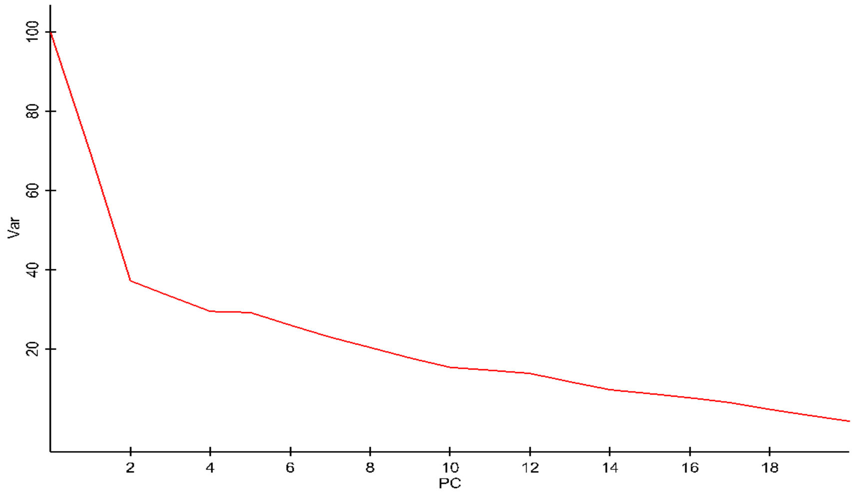

Figure 20: Eigenvalues plot of a XY mapping of cell. On the axis: PC=Principal component; Var= Variance

This plot shows the first components extracted tend to account for relatively large amounts of variance, while the later components account for relatively smaller amounts. By looking at the eigenvalues plot, the rule is to look for a "break" between the components with relatively large eigenvalues and those with small eigenvalues. The components that appear *before* the break are assumed to be meaningful and are retained for rotation; those appearing *after* the break are assumed to be unimportant and are ignored. In case of several break, we look for *last* big break before the eigenvalues begin to level off. Only the components that appear before this last large break should be retained [84]. In our case, the difficulty to determine the number of factors forced us to use a third criterion called the proportion of variance accounted for. It implies that a component is retained only if it accounts for 20% of the total variance. Thus, in the example of figure 20, we retain 6 PCs.

Once the number of PCs is found, the dataset is reconstructed and can be used for other statistical manipulations. The same pattern was applied to each XY mapping.

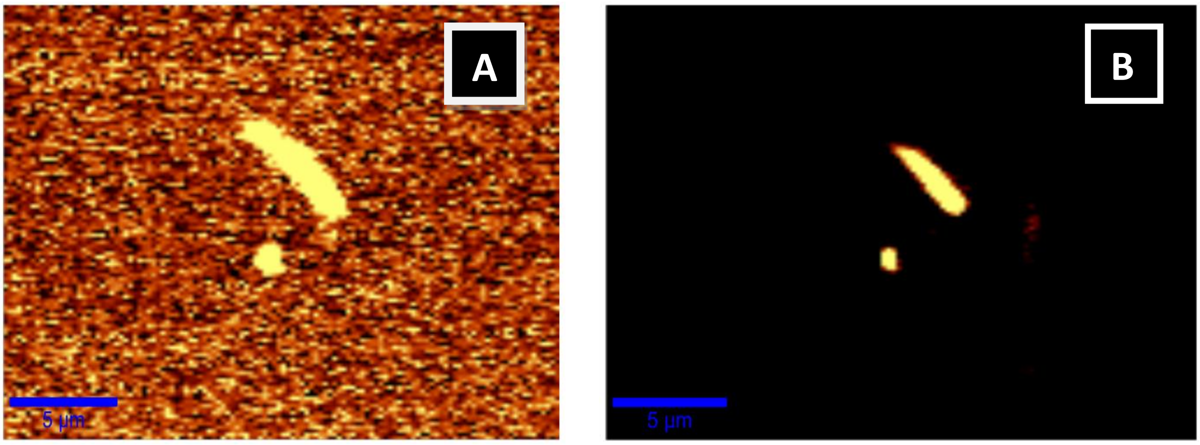

Figure 21: Raman mapping of tremolite fiber before PCA in A) and after PCA in B)

The Reconstructed image after the PCA method shown in figure 21 illustrated the reduction of the noise. It became easier to determine spectral differences. Thus, K-means HCA was applied to find out dissimilarities between spectra.

5.8.4 K MEANS HCA (HIERARCHICAL CLUSTER ANALYSIS)

Cluster analysis is an unsupervised statistical method that identifies and classes groups of samples on the basis of the information found in their data and allows to characterize their relationships. The aim is to find out the samples similar (related) between them and different (unrelated) from samples from other groups. Typically in clustering methods, all the samples with in a cluster are considered to be equally belonging to the cluster. As we work with hierarchical clustering, the result is displayed as a tree or a dendrogram i.e. it’s possible for clusters to have sub-clusters (children) as shown below.

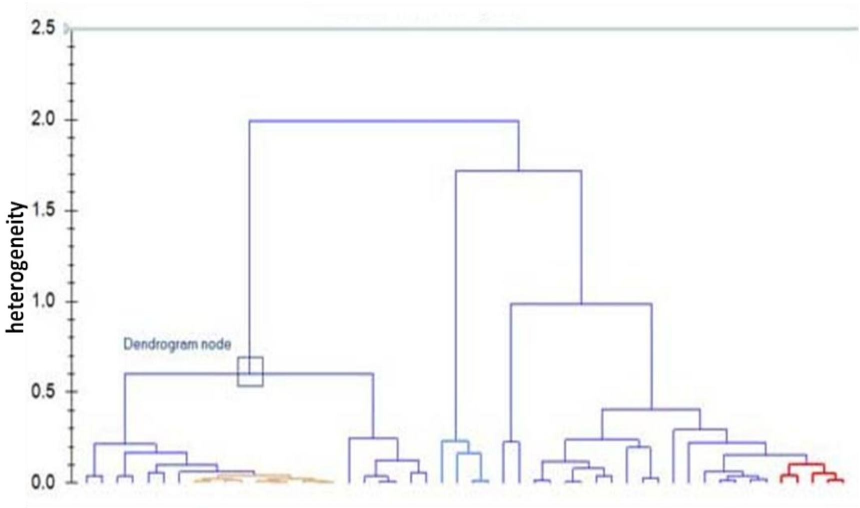

Figure 22: Example of dendrogram representation. A dendrogram node corresponds to heterogeneity between two classes. Each color represents a class.

Thus, clustering's goal is to find out "useful" groups of objects. K-means is a type of cluster usually use for spectroscopic data to reveal these groups. In this technique a cluster is defined as a set of objects in which each object is closer (more similar) to the prototype or reference (average of all the points in the cluster) that defines the cluster than to the prototype of any other cluster. Practically, a number K (user specified parameter) of clusters desired leads to the determination of K references. Each point of the data is assigned to the closest reference and each reference representing a cluster. Thus, the determination of sub-clusters is done by the determination of new K references from the cluster of interest and can be repeated as long as the references are not the same. The distance method used to find out the difference between spectra is the Euclidian distance:

$$\|a-b\|_2 = \sqrt{\sum_i (a_i - b_i)^2} \quad \text{(Eq.10)}$$

6. ARTICLES

METHODOLOGY FOR IR IMAGING OF INDIVIDUAL CELLS

Objectives: The aim of this work was to determine cell growth quality with respect to IR-transparent substrates properties by considering cell viability and IR spectral data.

This article has been submitted at applied spectroscopy in june 2012

Based on the physical and biological properties of each substrate, we realized experiments in order to determine the substrates allowing a high quality of cell culture and good IR spectral image. To obtain this information, most relevant biological and physical parameters characterizing a substrate have been selected and studied in order to find out which parameters are the most important to optimize the IR spectral data. The entire test has been realized according to the same procedure of cell growth for each substrate.

The IR imaging technique has been well developed for the study and the molecular imaging of biological samples in order to characterize their molecular contents. Several advantages of the technique as the ease of sampling, the unnecessary of using of contrast agents, the determination of specific molecule or bonds thanks to the unique spectral fingerprints for each target molecular arrangement. However, there are some analytical limitations such as the depletion of the sensitivity of IR detectors by working with thick tissue sections or very small sample, the limitation of resolution due to the spatial and lateral resolution and the impossibility to analyze sample with water. Therefore, FTIR imaging has been developed using synchrotron radiation in order to overcome these drawbacks. Indeed, an initiative study realized in our lab has shown the possibility to couple synchrotron radiation with focal plane array (FPA) detectors in order to enhance the signal to noise ratio thanks to the increase of the photon flux magnitude – three times higher than that of the conventional sources. Moreover, we also noticed that the reduction of the spot size from ≈ 100 µm to ≈10 µm permits to increase the spatial resolution. Promising results on the achievement of spectral information on sub cellular compartments led to the use of this technique for the present study. Thus, synchrotron radiation has been used to perform the experiments in order to find out which substrates allow the best SNR ratio and high quality of cell culture.

During this work, we grew and cryofixed the cell on each substrate according to a dedicated cell culture method developed in our lab. Then, we collected the IR data of the cells for each substrate using SR-IR light. Then we integrated the spectrum with the higher signal level at amide spectral interval corresponding to the nucleus location in the lipids, amide I and amide II spectral region. Two sets of parameters characterizing the substrates were selected:

1- the cell growth parameters (biotoxicity, adhesion, differentiation…) showing the ability of the substrate to allow a cell culture of quality,
2- Physical parameters (refractive index, reflective coefficient, transmission coefficient, Absorption coefficient, dielectric constant..) illustrating the capacity to obtain good IR data with each substrate.

The spectra obtained from each substrate have been processed using the statistical methods as the matrix of correlation and the Principal Component Regression (see sections 5.8.1 and 5.8.2.).

It turned out that the spectral acquisition quality is mainly influenced by the refractive index value, the hydrophilic degree reflected by the contact angle constant and the biotoxicity. Since the two last parameters are representative of a good quality cell culture, the refractive index value remains the most important parameters to consider. Finally, the best compromise can be obtained by working with Si, Ge and Si_3N_4 substrates.

Methodology for FTIR imaging of individual cells

Seydou Yao[1], Mariangela Cestelli Guidi[2], Michel Moenner[3], Giancarlo Della-Ventura[4], Augusto Marcelli[2], Cyril Petibois[1]

1: Chemistry and Biology of Membranes and Nano-Objects. Université de Bordeaux, CNRS UMR 5248, IPB. Allée de Saint Hillaire, F33600 Pessac, France; 2: INFN, Laboratori Nazionali di Frascati, Via E. Fermi 40, I-00044 Frascati (Rome), Italy ; 3: INSERM LAMC, UMR 1029, Université de Bordeaux, Avenue des Facultés, F33400 Talence, France; 4: Dipartimento Scienze Geologiche, Università Roma Tre, Roma, Italy.

Abstract: FTIR imaging is a novel spectroscopic technique able to provide cell imaging, *in vivo* and in real-time. However, one key-issue is developing methodologies for cell culture on IR-transparent substrates fitting cell biology requirements. In this work we tested different IR-transparent substrates in terms of biotoxicity, surface properties, and spectral image acquisition qualities. Only a few substrates, namely Si_3N_4, Ge, GLS, LaF_3, Si, SrF_2, ZnS/C, ZnS/F, were found to provide cell culture conditions comparable to those observed on usual polycarbonate petri dishes, the main limiting parameter being the toxicity of the material (ZnS, GLS, PbF_2, $PbCl_2$) or a poor adhesiveness (notably diamond, AgCl, CaF2, ZnS). From substrates eligible for a good-quality cell culture, the spectral acquisition quality is mainly affected by the refractive index value. Finally, the best compromise between cell culture quality and image spectral quality could be obtained using Si and Ge substrates. This rationalization of the available IR-transparent substrates for bioimaging is particularly relevant for live cell analyses, where cell culture conditions must remain unaffected by substrate properties.

Key-words: optical constants, cell culture, FTIR imaging

Abbreviations: ATR = attenuated total reflection; FTIR = Fourier-transform infrared; SNR: Signal to Noise Ratio; PCR: Principal component Regression

Introduction:

In the field of cell imaging, there are two main kinds of techniques: 1- those based on contrast agents or probes for analyzing a selected cellular compound, such as UV-confocal microscopy; and 2- those based on bulk information of sample, as for spectroscopy-based techniques, such as Raman or FTIR (1, 2). The clear advantage of probe-based techniques is to define *a priori* and without doubt the cellular information to analyze, thus giving access to very precise information, quantitative as well as topographic, when 3D rendering is feasible (3). Bulk analytical methods usually are not accurate, but by opening the spectrum of information collected from the sample, they also allow access to many characters relating to cell contents (4). Another major difference between these two aspects of cell imaging is that by focusing on a single target in the confined environment of a cell, probe-based techniques could be developed for very fast acquisitions (real-time down to ms or below), and at spatial resolution down to the nanoscale (5). This is clearly an analytical challenge that spectroscopic analytical methods will have to face up to continue playing a role in the field of cell imaging.

Among the available techniques, Raman microscopy seems to have gained in visibility by reaching ~250 nm spatial resolution for the semi-confocal setups (6), a value satisfactory for imaging many cell sub-compartments, such as mitochondria, vesicles, and the nucleus. It can be also coupled to other techniques, such as AFM or UV fluorescence, allowing a multimodal analysis of samples (1). However, live cell imaging is not a viable routine while using Raman microscopy, due to ionization and heating effect on cells because of the long acquisition required by a 3D mapping (~1 hour for high quality spectral acquisition). Among drawbacks, the laser effect on cell seems the most limiting parameter for cell imaging studies, since no cell biochemical processes can be investigated under a laser irradiation. To the contrary, FTIR imaging is now routinely used for analyzing biosamples, from cells to tissue sections (7). Traditionally, FTIR imaging is used in transmission, reflectance or transflectance mode with some major limits, such as dispersion artifacts (i.e., Mie scattering), a lateral resolution diffraction limited as a function of wavelength ($\lambda/2$ at the best: 3-6 μm in the mid-IR spectral interval), the impossibility to analyze living samples due to water absorption fluctuations, and a limited sensitivity while analyzing very small samples, namely single cells. Synchrotron radiation (8) may overcome these drawbacks thanks to the enhanced signal-to-noise ratio (SNR) while using a focal-plane array (FPA) detector, within short-time acquisitions (1-2 minutes). A specific experimental set up was proposed, where the IR beam was tuned in such a way to maximize the photon flux homogeneity between pixels rather than an intense small photon spot (9). This is a real advancement if compared with previous image acquisition based on single detector element , that requires long acquisition time affected also by beam stability and homogeneity of SNR (10). However, recent technological developments on FTIR imaging systems are now allowing the use of ATR crystals coupled to FPA detectors (11). This clearly open new frontiers to live cell imaging and even real-time analyses if we use a SR-IR beam (12) for reducing the acquisition time down to the range of seconds (13). The expected analytical performances of this new ATR-FTIR imaging setup include a lateral resolution of 1*1 µm or below, collecting the evanescent signal on the crystal surface for *in vitro* measurements with a negligible contribution by water absorptions.

However, this setup requires that the cell culture is performed directly on the ATR crystal, usually made by germanium (Ge) or diamond (Dd) crystals for the existing contact-mode devices. At present, no systematic study are available on IR-transparent windows to determine which substrate can match the quality of cell culture performed on polycarbonate petri dish. This is a major methodological issue for developing live cell imaging using an ATR crystal support. Here, we present a cell culture study on 12 IR-transparent windows to determine which substrates offer the best compromise between cell culture quality expectations and IR spectral image quality. The study focuses both on cell growth parameters (biotoxicity, division, differentiation…) and spectral information quality (spectral information obtained at nucleus, cytosol and membrane locations) extracted from FTIR images of individual cells.

Materials and Methods:

IR-transparent substrates:

Substrates selected for this study are listed in Table 1 with their main optical properties (most of optical properties available at http://www.crystran.co.uk/). Polycarbonate and glass have been added for biotoxicity and adhesion values, thus allowing a direct comparison with results on IR-transparent substrates.

Cell culture:

A dedicated cell culture method has been set up to allow a molecular analysis by FTIR imaging. The cell line used to test the culture method was the U87 human glioma cells (ATCC, HTB-14), which is highly proliferative and well resistant to stress factors. Cells were grown in a DMEM/F-12 medium supplemented with 10% fetal calf serum, 1 g/L of glucose, glutamine and antibiotics. Cells were routinely propagated in a humidified 5 % CO_2 atmosphere at 37°C (Heraeus incubator BB-6060). For obtaining a majority of individual cells on the IR-transparent substrate, sub-confluent cells were washed with PBS and incubated for 18 hours in DMEM F405-derived serum-free medium containing 5.55 mMol/L glucose. Cell cultures on IR-transparent windows were perfomed in parallel after sterilization of supports (24 h bath in ethanol + UV radiation for 15 minutes). Supports were placed in petri dishes before inserting culture medium and cells. Cells were incubated for 24 h before removing the substrates and washed three times with PBS. Residual buffer was removed by contact of substrate corner with absorbent paper. Substrates were immediately placed into tubes, closed and plunged in liquid N_2 for cryofixation. Tubes were further placed into a dry chamber with laminar flux at -20°C and open for slow lyophylization (12 h) to remove cellular water. After closing the tubes to avoid moisture deposition at temperature changes, samples were removed from the chamber and tubes could be open again after return to ambient temperature and substrates could be removed. Cell counting on substrate and petri dish (both on the same well and on control wells) was performed optically under an optical microscope for 3 different 2x2 mm areas on every substrate. Examples of cell cultures performed on different IR-transparent substrates are shown in figure 1.

FTIR imaging:

Optical and FTIR images were performed with the same microscope (Bruker Hyperion 3000 with a 64x64 elements FPA detector) coupled to a FTIR spectrometer (Bruker Equinox 55) illuminated by a synchrotron radiation IR source ($Ø \sim 35$ µm) as described elsewhere (14). N_2 purge was performed on both the microscope and the spectrometer for ensuring optimal spectra acquisitions and the plexiglass box (on the front of IR microscope) filled for better N_2 purge effectiveness. FTIR spectra acquisitions were performed in transmission mode, using 128 co-added scans (4000-900 cm^{-1}) and a 8 cm^{-1} spectral resolution. Individual cells were analyzed in triplicate per window with the magnification level sets at 36X (the final IR image has a pixel size of about ~1.1x1.1 µm). From each 2D image, the spectrum with higher signal level at amide spectral interval corresponding to the nucleus location was extracted. Then the integration of absorption from lipids (3000-2850 cm^{-1}), amides I (1720-1600 cm^{-1}) and II (1600-1490 cm^{-1}) bands were performed.

Statistics:

The first analysis between cell culture and substrate properties was the evaluation of biotoxicity and adhesiveness. All substrates identified as unsuitable for cell culture were removed from the further analysis. Significant parameters of a substrate were identified and evaluated. The first step was discriminating the covariables of substrates, i.e., potential redundancy of variables evaluating the same substrate of the cell culture parameter. The correlation test has been made for the main substrates properties (see supplementary material - table S1). A correlation matrix was built among optical properties of substrates and SNR values at different spectral intervals using the Pearson coefficient with a limit of confidence set at 5%. Multivariate analysis of the correlation among optical and spectral data was also performed using Principal Component Regression (PCR).

Results and discussion: The aim of this study was to determine an optimized substrate characterized by the most suitable properties for FTIR imaging of cells directly grown on this support. The objective is a critical step before proceeding to develop dedicated methodologies for live cell imaging by FTIR spectro-microscopy (13). Actually, we look for a substrate characterized by optimal optical properties, allowing simultaneously cell culture in conditions better or comparable to the routine cell biology procedures, where polycarbonate- (PC) or glass-made petri dishes are used. The most relevant parameter for cell biology is the biocompatibility of the substrate, which can be characterized both by cell viability and by cell adhesiveness on the surface (Table 2). Considering biotoxicity, we may point out that Ge, Si, diamond, Si_3N_4, and LaF_3 are the only substrates offering comparable biocompatibility (less than 10% cell death) to PC (5% cell death) or glass (3% cell death). The ZNS/C was also very close with a value of ~11% of cell death. Thus, the first useful information of this study is that the widely used substrates for FTIR spectroscopy and imaging in biosciences, i.e., CaF_2, ZnSe, and ZNS/F, are too toxic to allow a normal cell culture. It is thus obvious that substrate effects induced on cells can alter and even overcome effects induced by drugs, radiations…etc. masking the "real" experimental results. This critical issue points out the urgent need to define dedicated protocols for IR imaging techniques applied to live cell studies. The second parameter we took into account is cell adhesiveness on substrates. Compared to PC (187 cell/mm^2) or glass (171 cells/mm^2), IR-transparent substrates providing satisfying results were $Si_3N_4 > Si > LaF_3 >$ ZNS/C > Ge. All other substrates clearly show much lower cell adhesiveness. Again, CaF_2, ZnSe, and ZNS/F substrates are not satisfying in term of negative correlation found between the IR absorption level and the contact angle is however, an additional demonstration that the cell adhesiveness is a prerequisite for a valuable live cell imaging protocol. The opposite behavior observed between cell adhesion and contact angle in the correlation plot of the figure 2A points out the role of substrates physical property to obtain a standard cell growth. However, the lack of positive correlation with any other physical parameter points out also that no individual parameter can be selected to assess which substrate is suitable for cell imaging.

Therefore, a multivariate approach was necessary, considering many parameters at the same time for a correlation with spectral data. The Principal Component Regression (PCR) approach can be used to calibrate multivariate objects and thus compare systems defined by several parameters. Figure 2A and 2B shows the main results obtained with PCR for spectral data obtained at nucleus location on cell FTIR images. At the nucleus location, i.e., where the largest part of the signal comes from the nucleus itself (dense proteic object), but also from cytoskeleton (dense around nucleus for stability purposes), it was found that refractive index, adhesion, contact angle, and biotoxicity are the most important parameters. Indeed, Figure 2A points out the correlation between the parameters and the factors (F1, F2). Again, considering the results shown in Figure 2B, the adhesion parameter is the most relevant. This bi-plot shows that diamond, GLS, ZnS/F and PbF_2 are in opposite position with adhesion parameter, and then unsuitable for cell growth. If diamond is characterized by a poor adhesiveness, PbF_2, GLS, and ZNS/F are characterized by a high toxicity (see Table 1). In addition PCR gives the value of each parameter with their standard deviation and the value of the t-student test. A variable is significant when the p value greater than $|t|$ is less than 0.01%. Thus, the Table 3 shows only the significant parameters. Consequently, to have the highest integration value i.e., for example the highest SNR value for the amide I region, we need a substrate with high adhesion level, high refractive index, low biotoxicity, low contact angle, and low thermal conductivity. Physical parameters of substrates involved in multivariate correlation with IR signal level were found more numerous for amides absorption (1700-1480 cm^{-1}), with a higher correlation coefficient (> 0.8), than for fatty acyl chains absorptions (3020-2800 cm^{-1}). This is due to the higher SNR found in the amide spectral region, where the signal is by far higher than in the fatty acyl chains range. With an IR microscopy setup providing a 1.1x1.1 μm pixel resolution, this is clearly a direct consequence of the low organic material found at the single cell level. Therefore, one must consider that correlations emerging by this cell imaging study between substrates physical properties and IR absorption values are more reliable for the amide spectral range. As a result of all above information, the most suitable substrates characterized by the highest adhesiveness and refractive index values are Si > Ge > Si_3N_4 > LaF_3 > ZnS/C. Moreover, considering the biocompatibility results obtained, Ge, Si, Si_3N_4, and LaF_3 are the best candidate for cell cultures devoted to high quality FTIR imaging.

Conclusion:

The aim of this study was to determine the best substrate allowing to achieve the highest SNR for FTIR cell imaging. An important result we obtained was the poor biocompatibility of several substrates commonly used by IR spectroscopists such as for CaF_2 or ZnSe. The latter do not appear suitable for IR imaging of cultured cell, a prerequisite condition for live cell analyses. Optical properties of biocompatible substrates were further tested. Data point out that best candidates for FTIR imaging are Si and Ge. Germanium is already used in commercial ATR crystals and can be then reasonably considered a suitable material for high-quality high-resolution live cell imaging by means of FTIR microscopy. This study also points out that a *rationale* selection of substrates for live cell IR imaging have to be considered to move the IR spectroscopy towards *in vitro* applications.

Acknowledgements:

The authors are indebted to the "Italian-French University" (Vinci program 2009), the "Ligue Contre le Cancer", the "Agence Nationale pour la Recherche – ANR" for their financial supports, and the European Community's Seventh Framework Programme (FP7/2007-2013) under the grant agreement n. 226716.

References:

1. Petibois, C. (2010) *Anal Bioanal Chem* **397,** 2051-65.
2. Marcelli, A., Cricenti, A., Kwiatek, W. M., and Petibois, C. (2012) *Biotechnol Adv* **doi:10.1016/j.biotechadv.2012.02.012**.
3. Blow, N. (2008) *Nature* **456,** 825-8.
4. Martin, F. L., Kelly, J. G., Llabjani, V., Martin-Hirsch, P. L., Patel, II, Trevisan, J., Fullwood, N. J., and Walsh, M. J. (2010) *Nat Protoc* **5,** 1748-60.
5. Hell, S. W. (2007) *Science* **316,** 1153-8.
6. Liu, Z., Li, X., Tabakman, S. M., Jiang, K., Fan, S., and Dai, H. (2008) *J Am Chem Soc* **130,** 13540-1.

7. Petibois, C., and Déléris, G. (2006) *Trends Biotechnol* **24,** 455-62.
8. Petibois, C., Deleris, G., Piccinini, M., Cestelli Guidi, M., and Marcelli, A. (2009) *Nat Photonics* **3,** 179.
9. Petibois, C., Cestelli Guidi, M., Piccinini, M., Moenner, M., and Marcelli, A. (2010) *Anal Bioanal Chem* **397,** 2123-9.
10. Jamin, N., Dumas, P., Moncuit, J., Fridman, W. H., Teillaud, J. L., Carr, G. L., and Williams, G. P. (1998) *Proc Natl Acad Sci U S A* **95,** 4837-40.
11. Cestelli Guidi, M., Yao, S., Sali, D., Castano, S., Marcelli, A., and Petibois, C. (2012) *Biotechnol Adv.*
12. Petibois, C., and Cestelli Guidi, M. (2008) *Anal Bioanal Chem* **391,** 1599-608.
13. Petibois, C., and Desbat, B. (2010) *Trends Biotechnol* **28,** 495-500.
14. Petibois, C., Piccinini, M., Cestelli-Guidi, M., and Marcelli, A. (2010) *J Synhrotron Rad* **17,** 1-11.
15. Innocenzi, P., Kidchob, T., Bertolo, J. M., Piccinini, M., Guidi, M. C., and Marcelli, C. (2006) *J Phys Chem B Condens Matter Mater Surf Interfaces Biophys* **110,** 10837-41.
16. Diem, M., Romeo, M., Boydston-White, S., Miljkovic, M., and Matthäus, C. (2004) *Analyst* **129,** 880-5.
17. Holman, H. Y., Miles, R., Hao, Z., Wozei, E., Anderson, L. M., and Yang, H. (2009) *Anal Chem* **81,** 8564-70.
18. Holman, H.-Y. N., Martin, M. C., Blakely, E. A., Bjornstad, K., and Mckinney, W. R. (2000) *Biopolymers* **57,** 329-35.
19. Kneipp, J., Miller, L. M., Spassov, S., Sokolowski, F., Lasch, P., Beekes, M., and Naumann, D. (2004) *Biopolymers* **74,** 163-7.
20. Paluszkiewicz, C., Kwiatek, W. M., Banas, A., Kisiel, A., Marcelli, A., and Piccinini, M. (2007) *Vib Spectrosc* **43,** 237-42.
21. Wood, B. R., Quinn, M. A., Tait, B., Ashdown, M., Hislop, T., Romeo, M., and McNaughton, D. (1998) *Biospectroscopy* **4,** 75-91.

Figures:

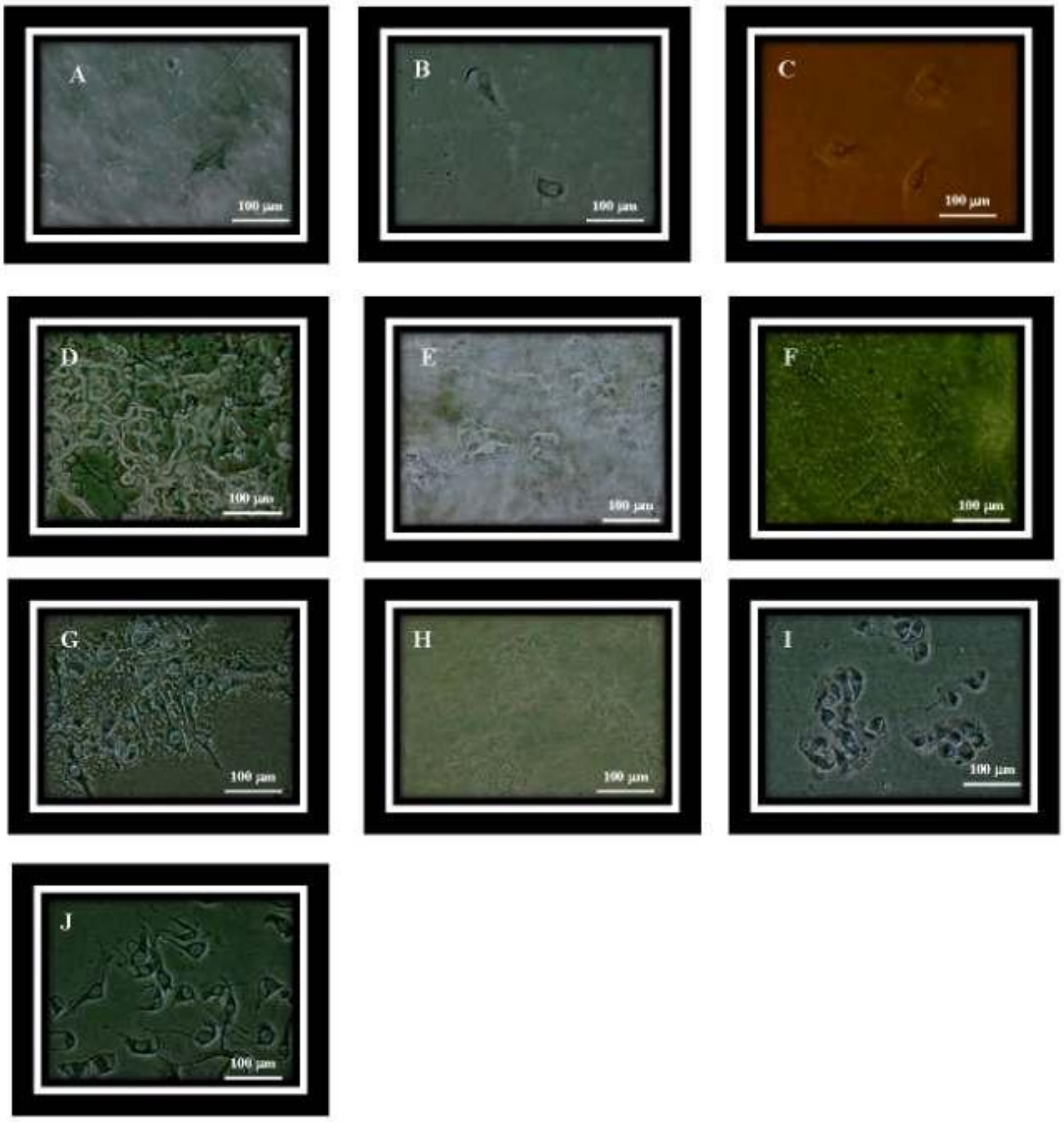

Figure 1: Optical images of two days culture cell on different substrates. **A**: AgCl – 9 cells/cm^2; **B**: CaF_2 – 24 cells/cm^2; **C**: GLS – 6 cells/cm^2; **D**: Si_3N_4 – 164 cells/cm^2; **E**: Diamond – 5 cells/cm^2; **F**: AgBr– 5 cells/cm^2; **G**: SrF_2 – 44 cells/cm^2; **H**: ZnS-F – 8 cells/cm^2; **I**: ZnS-C – 110 cells/cm^2 ; **J**: LaF_3 – 155 cells/cm^2.

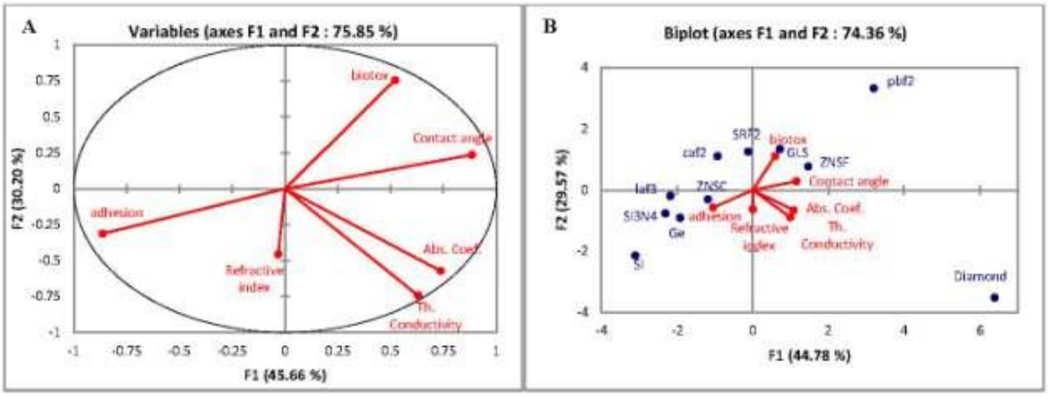

Figure 2: Principal component regression. A) The ellipse shows the correlation between different parameters and the factors F1, F2. B) Biplot of parameters and substrates positions vs. the factor F1 and F2.

Tables:

Parameters	**PC**	**Glass**	**Ge**	**SrF_2**	**LaF_3**	**ZNS/C**	**ZNS/F**	**GLS**	**Si_3N_4**	**Si**	**CaF2**	**ZnSe**	**D**	**AgCl**	**PbF_2**
Refractive index	-	-	4.01	1.39	1.60	2.49	2.24	2.40	1.98	3.42	1.39	2.43	2.38	1.99	1.70
Reflection coef.	-	-	0.36	0.03	0.05	0.18	0.15	0.29	0.11	0.30	0.03	0.17	0.17	0.11	0.07
Transmission coef.	-	-	1.88	1.32	1.44	1.72	1.67	1.70	1.59	1.84	1.32	1.71	1.70	1.60	1.48
Absorption Coef.	-	-	0.027	0.001	0.00085	0.0006	0.02	0.005	0.005	0.00001	0.0078	0.0005	0.07	**NA**	0.018
Th. Conductivity	-	-	58.61	1.42	5.1	27.2	16.7	0.43	30	163.3	9.71	19	2600	1.15	**NA**
Dielectric Constant	-	-	16.09	1.93	2.56	6.22	5.02	5.75	3.93	11.70	1.92	5.88	5.67	3.98	2.88
Contact angle	-	-	38.32	74.24	64.29	70.81	78.62	71.08	60.41	45.58	50.76	70.36	94.92	73.20	93.60
Biotoxicity	5	3	2	16	7	11	23	31	6	3	19	29	5	33	61
Adhesion	187	171	107	44	155	109	9	7	164	157	24	17	5	9	4

Table 1: Main optical properties of IR-transparent substrates. PC = polycarbonate; Coef. = coefficient. NA = not accessible. Units: Refractive index at 10 µm; Absorption Coefficient is in cm^{-1} at 10 µm; Thermal Conductivity is in $W \cdot m^{-1} K^{-1}$ at 293K; Dielectric constant is in GHz at 300 K; Contact angle is in degrees; Biotoxicity is in % of cell death after 24-h incubation; Adhesion is in $cells \cdot cm^{-1}$ after 24-h incubation.

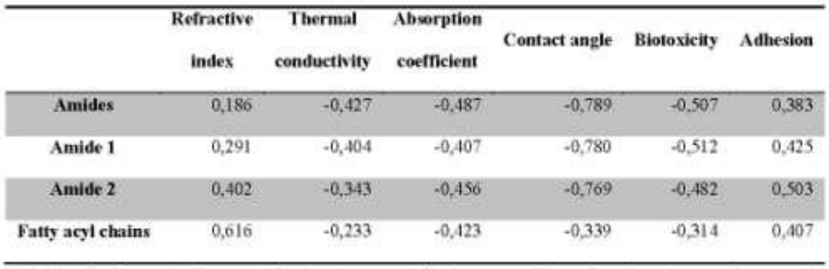

	Refractive index	**Thermal conductivity**	**Absorption coefficient**	**Contact angle**	**Biotoxicity**	**Adhesion**
Amides	0,186	-0,427	-0,487	-0,789	-0,507	0,383
Amide 1	0,291	-0,404	-0,407	-0,780	-0,512	0,425
Amide 2	0,402	-0,343	-0,456	-0,769	-0,482	0,503
Fatty acyl chains	0,616	-0,233	-0,423	-0,339	-0,314	0,407

Table 2: Correlation matrix between optical properties of substrates and spectral integration values at the nucleus location.

Integration	R^2	Refractive index	Thermal conductivity	Absorption coefficient	Contact angle	Biotoxicity	Adhesion
Amides	0.815	0.354			-0.597	-0.454	0.439
Amide 1	0.845	0.464	-0.659		-0.559	-0.474	0.346
Amide 2	0.845	0.508		-0.753			
Fatty acyl chains	0.698	0.675		-0.533			

Table 3: Significant parameters from the PCR test between optical and biological properties of substrates and spectral data at nucleus location of cells. (Units are in Table 1).

USE OF SYNCHROTRON-RADIATION BASED FTIR IMAGING FOR CHARACTERIZING CHANGES IN CELL CONTENTS

Objectives: The aim of this study was the determination of cellular contents changes of cryofixed cells on Si_3N_4 substrate by using FTIR imaging coupled with synchrotron radiation source and a focal plane array detector.

Widely used in laboratory, FTIR spectroscopy has shown its efficiency to access both biological and analytical information on biological sample by probing molecular functions. Thanks to the coupling with focal plane arrays, FTIR spectroscopy has proved its ability to image biological samples. However, in order to obtain quality spectra, it's necessary to realize fast scan acquisitions (minutes) and have a high signal to noise ratio (SNR). Indeed, to obtain both morphological and chemical information, the spectral quality is the main component leading to a good data treatment. Thus, recent studies have revealed that we obtain a higher SNR by using synchrotron radiation rather than Globar source. Moreover, the use of SR radiation permits to reduce the lateral resolution of the technique to the micrometer and to increase his sensitivity. Thus, FTIR imaging fits with the investigations of issues in cell biology by extracting spectral information from biosamples. The goal of this study was to demonstrate the ability of SR FTIR imaging to differentiate two biochemical states of cells by extracting spectral information belonging to the most important molecular contents of samples.

To be able to do that, human cerebral micro-vascular endothelial cell line (hCMEC) has been cultured directly on Si_3N_4 substrate using two different experimental conditions: control and low glucose content. IR images acquisition was realized over periods around 10 minutes in order to obtain the higher SNR with a safe sample. Curve fitting procedures were performed in amide I region (1720–1580 cm^{-1}) and fatty acyl chains (3020–2800 cm^{-1}) regions in order to access to protein secondary structure and to $\nu(C{=}CH)$, ν_{as} (CH_2), and ν_{as} (CH_3) absorption of fatty acyl chains. Several differences were observed: 1-a lower amide I to amide II ratio ($p<0.01$) 2- a different secondary structure profile of proteins, with a significant increase in non-ordered structure components ($P<0.01$); and 3- a higher $\nu(C{=}CH)/ \nu_{as}$ (CH_3) absorption ratio ($P<0.01$) showing an increase of the unsaturation in fatty acyl chains.

Thus, our study has demonstrated that FTIR imaging with a synchrotron radiation source is able to find out molecular changes at single cell level between two physiological conditions. This proves the ability of SR FTIR imaging to analyze low organic matter on the basis of their main molecular structure at a single cell level, which offers a range of application using vibrational spectroscopy in cell biology studies.

Use of synchrotron-radiation-based FTIR imaging for characterizing changes in cell contents

Seydou Yao, Michel Moenner, Anders Engdahl & Cyril Petibois

Analytical and Bioanalytical Chemistry

ISSN 1618-2642
Volume 404
Number 5

Anal Bioanal Chem (2012)
404:1311-1316
DOI 10.1007/s00216-012-6223-0

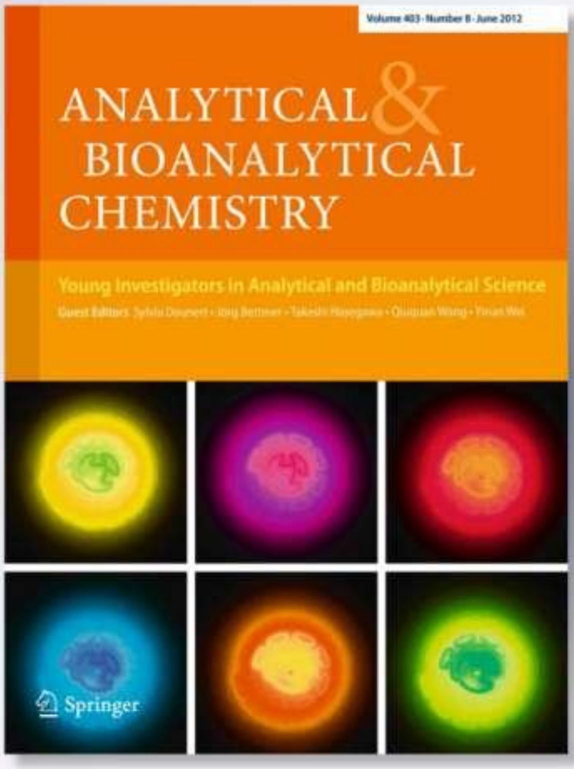

Springer

Anal Bioanal Chem (2012) 404:1311–1316
DOI 10.1007/s00216-012-6223-0

ORIGINAL PAPER

Use of synchrotron-radiation-based FTIR imaging for characterizing changes in cell contents

Seydou Yao · Michel Moenner · Anders Engdahl · Cyril Petibois

Received: 9 December 2011 / Revised: 14 June 2012 / Accepted: 20 June 2012 / Published online: 20 July 2012

Abstract FTIR imaging of individual cells is still limited by the low signal-to-noise ratio obtained from analysis of such weakly absorbing organic matter when using a Globar IR source. In this study, we used FTIR imaging with a synchrotron radiation source and a focal plane array detector to determine changes in the cellular contents of cryofixed cells after culture for 48 h on Si_3N_4 substrate. Several spectral differences were observed for cells deprived of glucose compared with control cells: a lower amide I-to-amide II ratio ($P<0.01$); a different secondary structure profile of proteins (obtained from amide I spectral region curve fitting), with a significant increase in non-ordered structure components ($P<0.01$); and a higher $\nu(C{=}C\text{–}H)/\nu_{as}(CH_3)$ absorption ratio ($P<0.01$), suggesting increased unsaturation of fatty acyl chains. Therefore, our study has shown that FTIR imaging with a synchrotron radiation source enables determination of several spectral changes of individual cells between two experimental conditions, which thus opens the way to cell biology studies with this vibrational spectroscopy technique.

Keywords Bioanalytical methods · Spectroscopy/instrumentation · IR spectroscopy/Raman spectroscopy · Imaging · Synchrotron radiation

Abbreviations

FPA	Focal plane array
FTIR	Fourier-transform infrared
SNR	Signal-to-noise ratio
SR	Synchrotron radiation

Introduction

Among the analytical techniques able to provide global information about a sample, those based on vibrational spectroscopy, mainly Fourier-transform infrared (FTIR) and Raman, have been shown to be useful for biological studies. From molecular assemblies [1, 2] to biological samples [3–5], FTIR spectroscopy setup as microscopy [6] or as an imaging technique [7] is now widely used in research laboratories and is starting to be implemented routinely in clinics [8, 9]. However, FTIR imaging of biological samples requires rapid spectral acquisition for in-vitro or in-vivo applications [10] and high signal-to-noise ratio (SNR) for further spectral data treatment. Recently, it has been shown that FTIR imaging with a synchrotron radiation (SR) source results in a higher SNR than use of a Globar source [11], thus enabling better lateral resolution and/or higher sensitivity [12]. Pioneering studies demonstrated that cell biology could be investigated with unprecedented spectral quality and with short acquisition times, i.e., minutes. Globally, it was demonstrated that the intensity of IR absorption of amides (1700–1500 cm^{-1}), saccharides (1150–

Published in the special paper collection *Imaging Techniques with Synchrotron Radiation* with guest editor Cyril Petibois.

S. Yao · C. Petibois (✉)
Université de Bordeaux, CNRS UMR 5248,
Allée de St Hillaire,
33600 Pessac-Cedex, France
e-mail: cyril.petibois@u-bordeaux2.fr

C. Petibois
e-mail: cyril.petibois@orange.fr

M. Moenner
Université de Bordeaux, CNRS UMR 5095,
1, rue Camille Saint Saëns,
33077 Bordeaux-Cedex, France

A. Engdahl
MAX-lab - Lund University,
P.O. Box 118, 22100 Lund, Sweden

950 cm^{-1}), and fatty acyl chains (3020 2800 cm^{-1}) was higher when using the SR source and the SNR was one order of magnitude higher, thus resulting in much better spectral quality [13]. This was achieved by combining use of a SR source with appropriate management of a focal plane array (FPA) detector (reduction of the number of pixels in the array to 32×32 instead of 64×64 or 128×128 to fit the dimensions of the SR source spot on the detector) [14]. Analytically, therefore, SR-FTIR imaging is now suitable for cell biology investigations [10]. The next step toward functional FTIR imaging is to extract spectral information from samples to show the potential of the technique as a chemical and/or molecular probe of cells. More specifically, considering that FTIR spectroscopy is, in essence, a technique for probing the molecular functions of a sample, FTIR imaging data treatment for biosamples should primarily focus on molecular recognition of sample contents or structural biochemistry of large molecules, for example proteins.

The purpose of this study was to show that SR-FTIR imaging can be used to distinguish between two biochemical states of cells by extracting spectral information belonging to the most important molecular contents of samples. We used cells cultured for 48 h directly on Si_3N_4 as substrate and analyzed in transmission under two different conditions, control and energetically deprived (low glucose content). We also applied curve-fitting procedures to different spectral regions for analysis of protein and fatty acyl chain structure changes.

Materials and methods

Cell culture

As previously described [14], a dedicated cell-culture method has been set up to enable molecular analysis by FTIR imaging. The cell line used to test the culture method was the human cerebral microvascular endothelial cell line hCMEC/D3 [15]; these cells have the potential to undergo tubule formation (during blood capillary sprouting), and thus have numerous cell junctions. Cells were grown in DMEM/F-12 medium supplemented with 10 % foetal calf serum, 1 gL^{-1} glucose, glutamine, and antibiotics. Cells were routinely propagated in a humidified 5 % CO_2 atmosphere at 37 °C (Heraeus incubator BB-6060). Serum-free culture was performed in accordance with methods reported elsewhere [16]. The serum-free medium consisted of a basal medium supplemented with 25 μg mL^{-1} HDL, 5 μg mL^{-1} insulin, 5 μg mL^{-1} transferrin, 2 ng mL^{-1} EGF, 1 mg mL^{-1} f-BSA, and antibiotics. To obtain as many individual cells as possible on the IR-transparent substrate, sub-confluent cells (10^3 cm^{-2}) in serum-free medium were washed with PBS and incubated for 48 h in DMEM F405-derived serum-free medium containing 5.55 mmol L^{-1} (control) or 1 mmol L^{-1} (energy deprivation) glucose (named low-Glc).

Cell adhesion on the substrate was estimated by counting 2×2 mm^2 areas, and cell toxicity was evaluated by measuring LDH activity as an indicator of cell viability after 18 h (TOX-7 assay kit; Sigma Aldrich, France), which was set at 20 % for positive.

Substrates were rinsed from 3 to 5 times with PBS and residual fluid was removed by capillary action, by use of blotting paper for a few seconds. Samples were immediately placed in polycarbonate airtight tubes and plunged into piled carbon dioxide ice for instant freezing. This freezing method with carbon dioxide ice (−80 °C) was preferred to isopentane liquid N_2 flash freezing (−170 °C) to preserve the integrity of the thin and fragile Si_3N_4 windows (0.5 μm thick). Tubes were further placed into a freezing chamber with a dry laminar air flow set at −20 °C. After a few minutes, i.e., when the tubes returned to the temperature of the freezing chamber, the tubes were maintained open for 24 h for sample dehydration (slow freeze-drying) to maintain cell morphology (Fig. 1). Tubes were finally closed again before removal from the chamber to avoid deposition of atmospheric moisture on the samples induced by the rapid temperature change.

FTIR imaging

FTIR imaging was performed in a transmission for cell analysis (Fig. 1). Optical and FTIR images were performed with the

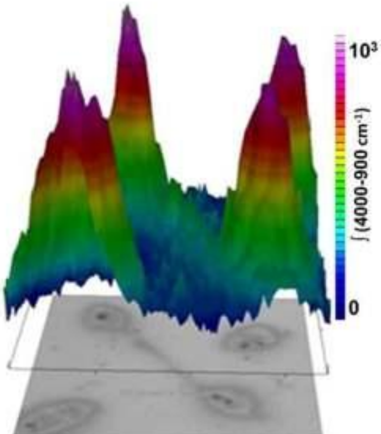

Fig. 1 FTIR image of cells cultures on Si_3N_4 substrate. The image shows an example of overlay of visible views of two hCMEC/D3 cells connected by a filopode. FTIR image rendering shows absorption intensity for the full spectral region (4000–900 cm^{-1})

Table 1 Results from integration of absorption bands for the main molecular components of cells (n=87 cells)

Conditions	Amide I	Amide II	Amide I/II	ν(C=CH)	ν_{as}(CH$_3$)	ν_{as}(CH$_2$)	ν(C=C–H)/ν_{as}(CH$_3$)	ν(C–O)
Control	2.28±0.22	1.16±0.18	1.97±0.27	0.02±0.01	0.12±0.03	0.25±0.07	0.16±0.04	0.33±0.09
Low-Glc	2.15±0.18	0.89±0.20*	2.42±0.31*	0.04±0.02*	0.13±0.05	0.21±0.05	0.31±0.07*	0.24±0.04*

*Significantly different from controls ($P<0.05$)

same microscope (Bruker Hyperion 3000 with a 128×128 FPA; individual dimension of detectors 40×40 μm^2; Bruker Optik, Ettlingen, Germany) coupled to an FTIR spectrometer (Bruker IFS66V) illuminated by the MAX-lab SR-IR source (size ~50×40 μm^2; photon flux 10^{13}–10^{14} ph s^{-1} cm^{-1}) [17]. N$_2$ purge was performed on both the microscope and the spectrometer to ensure optimum spectral acquisition (i.e. minimum atmospheric variation). The 32-pixels correlation mode of the FPA detector was switched off during IR image acquisition with the SR-IR source. The FPA detector was controlled to switch on only 32×32 elements (by using the WinIR software from Santa Barbara Focal Plane) to fit better the SR source dimensions at the sample location. A series of 87 individual cells were analyzed by use of a 15× magnification for a final image size of ~85×85 μm^2. Spectral images were obtained by co-addition of 128 scans at a spectral resolution of 8 cm^{-1}.

Spectral data treatment

To determine the potential of SR-FTIR imaging to distinguish between two cellular conditions, we first performed spectral integration of IR absorption of amide I (1712–1581 cm^{-1}), amide II (1581–1481 cm^{-1}), fatty acyl chains (3020–2800 cm^{-1}), and saccharides (1150–950 cm^{-1}). The amide I/amide II absorption ratio was determined as a folding index of proteins. Spectral curve fitting of amide I (1720–1580 cm^{-1}) and of fatty acyl chains (3020–2800 cm^{-1}) spectral regions were performed as described elsewhere [3, 18, 19] for access to protein secondary structure and to ν(C=CH), ν_{as}(CH$_2$), and ν_{as}(CH$_3$) absorption of fatty acyl chains [17]. All results were expressed as mean ± SE. Comparisons of tumours (solid, diffuse) and healthy tissue were performed by multivariate analysis of variance (MANOVA; SPSS 15.0, SPSS, France) of results obtained from the integration, measurement of absorption ratios, and spectral curve fitting of the different spectral regions. P values of 0.05 were used to indicate significant differences between series of data.

Results

Cell viability

Cell cultures on Si$_3$N$_4$ as substrate were found to be comparable with those grown under control conditions on conventional plastic Petri dishes (n=12 substrates; 64±11 vs. 71±17 cells mm^{-2}; r=0.91, $P<0.01$). A lower rate of division, only 56±13 cells mm^{-2}, was observed for cells grown in low-glucose medium (significantly different from that under control conditions, $P<0.05$). Toxicity was negative under all conditions.

FTIR image acquisition

As shown in Fig. 1, cells could be analyzed by FTIR imaging with a synchrotron radiation source after reduction of the FPA detector size to 32×32 elements to obtain final image dimensions of 85×85 μm, which was large enough for individual (i.e., non-confluent) cells. SNR at the nucleus location was 1067±93, and 408±44 at the cytosol location (n=87 cells). Acquisition time for every IR image was 617 s (256 scans at 8 cm^{-1}) with a decrease in energy level between background and sample image acquisition of <10 % (221±18 vs. 204±13 mA, respectively).

Spectral data treatment

The IR spectrum corresponding to nucleus location of every cell was selected for comparison of cell data between cell culture conditions. Tables 1 and 2 show results obtained for the different spectral regions corresponding to fatty acyl chains (3020–2800 cm^{-1}), proteins (1720–1481 cm^{-1}), and saccharides (1150–950 cm^{-1}), as shown in Fig. 2. Figure 3 shows details on curve-fitting performed on fatty acyl chain [19–21] and protein [22–25] spectral regions (corresponding to results in Tables 1 and 2). It was found that low-Glc conditions induced a decrease in amide II absorption whereas amide I absorption remained equivalent between cell culture conditions. As a consequence, the amide I/amide II absorption ratio was significantly higher for low-Glc conditions ($P<0.05$). An inverse pattern of changes was found for fatty acyl chain absorption, with a marked increase in

Table 2 Secondary structure of proteins (n=87 cells)

Conditions	α-helix	β-turns	β-sheets	Unordered
Control	33±7	21±5	34±5	12±1
Low-Glc	27±5*	19±7	38±7*	16±3*

*Significantly different from controls ($P<0.05$)

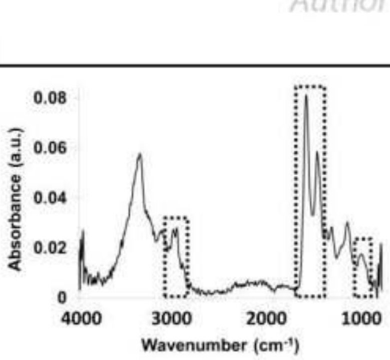

Fig. 2 Example of FTIR spectrum extracted from the FTIR image of cell. Spectral regions used for FTIR image data treatment are shown on the spectrum

ν(C=C H) absorption ($P<0.05$) for low-Glc conditions whereas the $\nu_{as}(CH_3)$ absorption was not modified. The ν(C=C H)/$\nu_{as}(CH_3)$ absorption ratio increased by one order of magnitude between control and low-Glc conditions ($P<0.01$). Results from 1150 950 cm^{-1} spectral region integration were found to decrease by 27 % between control and low-Glc conditions ($P<0.05$).

Spectral curve-fitting for the amide I region revealed all the secondary structure of the proteins (Table 2 and Fig. 3) and could be also used for discriminating between control and low-Glc conditions. Globally, it was found that α-helix absorption was reduced by 19 % whereas β-sheets and unordered structural components increased by 11 and 25 %, respectively (all significantly different from control conditions with $P<0.05$).

Discussion

Development of FTIR imaging for cell biology investigations started in the 90s with the advent of microscopes enabling *x*,*y* mapping of a sample in micrometric steps [6, 8, 26]. However, the very long acquisition time required for a single cell limited utilization of IR microscopes for cohort studies, which are normally required for a full cell biology study. The commercial release of IR imaging systems equipped with a FPA detector was thought to give a second life to cell imaging by IR. However, the very low photon flux obtained by such imaging systems equipped with a Globar source was limited interest for cell samples, which are primarily characterized by their low organic matter content, of the order of pg μm^{-2}. Use of a synchrotron radiation source was envisaged as rapidly overcoming this limitation, but the shape of the source spot at the sample location did not enable proper coverage of the FPA detector and decay of the photon flux between elements could be several orders of magnitude [11, 13]. The solution found was to reduce the number of elements on the FPA detector to make the detector size a better fit to the source dimensions. With a high current (1.2 to 2 A), IR image acquisition could be achieved within 1 2 min only. This short acquisition time enabled avoidance, as much as possible, of the lateral instability of the IR source at the sample location, thus reducing correlatively the noise in the final IR image spectra [14]. However, the current decrease between the beginning and completion of image acquisition was from 2.0 to 1.6 A under the best conditions, so spectra remained noisy and poorly suitable for sophisticated data treatment. Only a global study was possible for the spectral regions of interest. Curve-fitting procedures could not be performed, because small absorption bands could overlap or their shape could be modified by many noise bands. Therefore, no systematic study could be performed on series of cellular samples.

In this study, the objective was to demonstrate that long acquisition time could be beneficial for obtaining better spectral quality of IR images of cells, even when using a synchrotron radiation source with low energy level. The MAX-lab MAX I IR beamline 73 is equipped with the Bruker Hyperion 3000 imaging system, which can be found on most modern

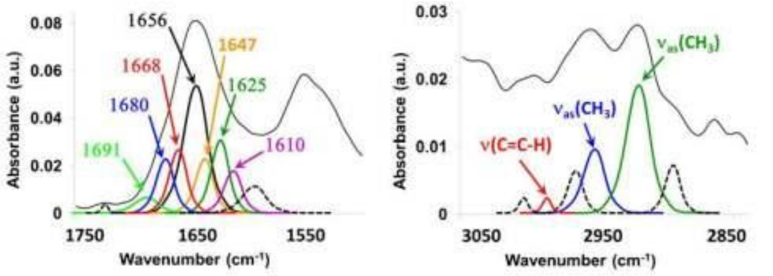

Fig. 3 Spectral curve-fitting performed for protein and fatty acyl chains structure investigation. Absorption bands of proteins were assigned as follows: α-helix (1656 cm^{-1}), β-sheets (1691, 1680, and 1625 cm^{-1}), β-turns (1668 and 1608 cm^{-1}), and unordered structure (1647 cm^{-1}). Secondary structure was expressed as a percentage of total amide I absorption (Table 2). Fatty acyl chain absorption bands were found centred at 3012 cm^{-1} for ν(C=C–H), 2951 cm^{-1} for $\nu_{as}(CH_3)$, and 2928 cm^{-1} for $\nu_{as}(CH_2)$

synchrotron facilities. We used the same procedure as before for obtaining the best fit between the synchrotron IR source shape and FPA detector size, thus reducing the number of elements [14]. However, IR image acquisition was performed over longer periods, approximately 10 min. The lower synchrotron radiation intensity (250 mA for a photon flux of 10^{13}–10^{14} ph s^{-1} cm^{-1}) combined with freeze drying of cell samples made spectral acquisition safe for the sample contents. Furthermore, because of the small current decrease (no more than 10 %) and a stable IR source spot at the sample location over a 10-min acquisition period, the SNR obtained for IR spectral images was high. Such a long scanning period does not enable real-time imaging applications, but the objective here was to obtain high-quality spectra for proposed advanced treatment of spectral data. The high SNR obtained in this study enabled use of a curve-fitting procedure on amide I and fatty acyl chain spectral regions without perturbation of small IR bands by noise. This was noteworthy for the 3050–2800 cm^{-1} spectral region of fatty acyl chains, in which the very weak $\nu(\mathrm{C{=}C{-}H})$ IR absorption band centred at 3012 cm^{-1} could be revealed, which is clearly a sign of spectral quality for biological samples analyzed by FTIR imaging or spectroscopy [19]. Therefore, the $\nu(\mathrm{C{=}C{-}H})/\nu_{as}(\mathrm{CH_3})$ absorption ratio could be determined, and this enabled study of the effect of low-Glc conditions on phospholipid oxidative stress [27, 28]. Therefore, for the first time with an FPA-based IR imaging system with an SR source, cells could be analyzed to determine molecular changes between two physiological conditions at the single-cell level. The other challenging data treatment to apply was determination of the secondary structure of proteins by using the very overlapping IR bands found within the amide I spectral region. Again, systematic curve-fitting of this spectral region requires use of spectra with high SNR to avoid abnormal band resolution or signal perturbation by noise [25, 29, 30]. Here, the seven absorption bands of the amide I spectral region could be systematically obtained from the IR spectra corresponding to location of the nucleus of cells. As previously reported [23, 31, 32], changes in the secondary structure of proteins revealed abnormal cellular development because of energy deprivation as a result of low-Glc culture conditions. The significant decrease in α-helix absorption and concurrent increase in unordered structure absorption is a sign of global protein misfolding by the cellular machinery [33–35]. The third spectral region investigated was that of saccharides for the 1150–950 cm^{-1} region. It was found that IR spectra of cells grown under low-Glc conditions had lower absorption intensity for this spectral region, which corresponded to the lower glucose concentration in culture medium. Finally, all cells could be imaged by use of FTIR with an SR-IR source, and the main three spectral regions (proteins, fatty acyl chains, and saccharides) could be investigated to provide global molecular information about sample changes because of abnormal physiological condition.

Conclusion

Our study has shown that SR-FTIR imaging is now sufficiently efficient to enable analysis of the low organic matter content of small biological samples, namely individual cells, on the basis of their main molecular structures. A low energy storage ring with stable current level was used for long scanning periods to obtain a high signal-to-noise ratio in FTIR spectral images of cells, thus enabling use of sophisticated spectral data treatment. Importantly, curve-fitting of the amide I spectral region could be performed for analysis of the secondary structure of proteins. Spectral regions of fatty acyl chains and the saccharide content of cells could be also investigated, thus providing a global overview of cell molecular changes between two physiological conditions. Therefore, this study demonstrated that SR-FTIR imaging is a suitable analytical technique for investigation of the molecules in cells.

Acknowledgements The authors are indebted to the "Ligue Nationale contre le cancer" and the "Agence Nationale de la Recherche" (ANR contract no. bl-inter09_464249 – MIAG-X) for financial support. This research was also supported within the EU 7th Framework Programme (FP7/2007-2013) under the grant agreement no. 226716.

References

1. Castano S, Delord B, Fevrier A, Lehn JM, Lehn P, Desbat B (2009) Biochimie 91:765–773
2. Castano S, Desbat B (2005) Biochim Biophys Acta 1715:81–95
3. Petibois C, Déléris G (2006) Trends Biotechnol 24:455–462
4. Petibois C, Desbat B (2010) Trends Biotechnol 28:495–500
5. Petibois C, Cazorla G, Cassaigne A, Deleris G (2001) Clin Chem 47:730–738
6. Jamin N, Dumas P, Moncuit J, Fridman WH, Teillaud JL, Carr GL, Williams GP (1998) Proc Natl Acad Sci U S A 95:4837–4840
7. Fernandez DC, Bhargava R, Hewitt SM, Levin IW (2005) Nat Biotechnol 23:469–474
8. Dandon M, Marfisi C, Lacour B, Bader C (1991) Clin Chem 37:83–87
9. Naumann D, Helm D, Labischinski H (1991) Nature 351:81–82
10. Cestelli Guidi M, Yao S, Sali D, Castano S, Marcelli A, Petibois C (2012) Biotechnol Adv doi:10.1016/j.biotechadv.2011.11.009
11. Petibois C, Deleris G, Piccinini M, Cestelli Guidi M, Marcelli A (2009) Nat Photonics 3:179
12. Petibois C (2010) Anal Bioanal Chem 397:2031–2032
13. Petibois C, Piccinini M, Cestelli-Guidi M, Marcelli A (2010) J Synchrotron Rad 17:1–11
14. Petibois C, Cestelli Guidi M, Piccinini M, Moenner M, Marcelli A (2010) Anal Bioanal Chem 397:2123–2129
15. Weksler BB, Subileau EA, Perriere N, Charneau P, Holloway K, Leveque M, Tricoire-Leignel H, Nicotra A, Bourdoulous S, Turowski P, Male DK, Roux F, Greenwood J, Romero IA, Couraud PO (2005) FASEB J 19:1872–1874
16. Barnes PR, Taylor DJ, Kemp GJ, Radda GK (1993) J Neurol Neurosurg Psychiatry 56:679–683
17. Nelander B, Sablinskas V (1995) J Mol Struct 348:167–170

18. Belbachir K, Noreen R, Gouspillou G, Petibois C (2009) Anal Bioanal Chem 385:829–837
19. Petibois C, Déléris G (2004) Analyst 129:912–916
20. Petibois C, Cassaigne A, Gin H, Deleris G (2004) J Clin Endocrinol Metab 89:3377–3384
21. Petibois C, Déléris G (2005) Cell Biol Int 29:709–716
22. Noreen R, Moenner M, Hwu Y, Petibois C (2012) Biotechnol Adv doi:10.1016/j.biotechadv.2012.03.009
23. Wehbe K, Pinneau R, Moenner M, Deleris G, Petibois C (2008) Anal Bioanal Chem 392:129–135
24. Petibois C, Gouspillou G, Wehbe K, Delage JP, Deleris G (2006) Anal Bioanal Chem 386:1961–1966
25. Goormaghtigh E, Raussens V, Ruysschaert JM (1999) Biochim Biophys Acta 1422:105–185
26. Wood BR, Quinn MA, Tait B, Ashdown M, Hislop T, Romeo M, McNaughton D (1998) Biospectroscopy 4:75–91
27. Petibois C, Déléris G (2005) Arch Med Res 36:524–531
28. Severcan F, Gorgulu G, Gorgulu ST, Guray T (2005) Anal Biochem 339:36–40
29. Surewicz WK, Mantsch HH, Chapman D (1993) Biochemistry 32:389–394
30. Troullier A, Reinstadler D, Dupont Y, Naumann D, Forge V (2000) Nat Struct Biol 7:78–86
31. Drogat B, Bouchecareilh M, Petibois C, Déléris G, Chevet E, Bikfalvi A, Moenner M (2007) J Cell Physiol 212:463–472
32. Petibois C, Drogat B, Bikfalvi A, Deleris G, Moenner M (2007) FEBS Let 581:5469–5474
33. Brauns EB, Dyer RB (2005) Biophys J 89:3523–3530
34. Fabian H, Naumann D (2004) Methods 34:28–40
35. Schultz CP, Barzu O, Mantsch HH (2000) Appl Spectrosc 54:931–938

SR-FTIR IMAGING AS A TOOL FOR STUDYING CELL-ASBESTOS FIBERS INTERACTION

Objectives: This study has been realized to analyze the interaction between asbestos fibers and epithelial lung single cell by FTIR imaging. The final goal was to develop a dedicated synchrotron radiation FTIR (SR-FTIR) imaging methodology for analyzing the effect of asbestos fibers on single cell with a 1×1 µm lateral resolution.

Asbestos fibers refer to a group of occurring naturally silicates. These materials have been widely used for their exceptional physical and chemical properties in several industrial applications. Their presence in the environment has been recognized to cause deadly lung pathologies as asbestosis or mesothelioma after exposure. The details on the pathological pathway remain largely unknown because their heterogeneity in chemistry and morphology. Indeed, the toxicity of these fibers depends not only on their dimensions, but also on their habit and surface chemistry. Therefore, there are multiple fiber-cell interactions and phenomena making challenging their interpretation.

The study of interactions between asbestos fibers and cells is also a challenge because we need a technique that allows 1- to analyze organic materials with inorganic species at the same time; 2 – to obtain both morphological and chemical information simultaneously and 3- work at a cellular level. This is why we decided to use spectroscopic methods and IR spectroscopy in particular. Indeed thanks to preliminary studies performed in our laboratory, we developed a dedicated method using bi-dimensional focal-plane-array (FPA) of detectors which allow the collection of 2D infrared images of *ex vivo* cells in a short time.

By implementing our knowledge of SR-IR radiation coupled to FPA detectors and our ability to perform individual ex vivo cells culture on Si substrate, we develop a method to analyze the interactions between inorganic environmental fibers (asbestos).

First of all, the biological study of cell treated with different types of fiber reveals:

1- The concentration of fibers up to 20µg/ cm² is not lethal for the cells
2- Different types of fiber with different chemistry seem to exhibit the same toxic pattern

We use these information to compare the IR spectra between control cell, cells with 10 µg/ cm² (no lethal concentration) and cells with 50 µg/ cm² (lethal concentration).Unfortunately, we could not able to use the synchrotron radiation and all the work was done first using conventional Globar source. This implies that the absorbance level of each 2D IR images was very low for each single cell. Therefore, we integrated the amides and lipids absorption bands only due to their major intensity in the spectra.

By comparing the results obtained from different types of fibers and concentrations, we observed that the molecular change induced on cells could be differentiated. The changes due to the interaction with different types of fibers for amide I, amide II and amide I / amide II were equivalent. Moreover, the ratio of protein to lipids content increased with the concentration of fibers, increase revealed by an enhancement of cellular proliferation, result already known by biologists.

Despite the use of Globar source, IR imaging has shown its ability to show molecular changes in one cell. Moreover, we were able to determine the relative toxicity of different types of fibers interacting with lung cells.

SR-IR imaging as a tool for studying cell-asbestos fibers interaction

Seydou Yao[a,b], Francesco Lazzarin[c], Fabio Bellatreccia[b,d], Gianluca Iezzi[e], Mariangela Cestelli Guidi[d], Claudia Petrarca[c], Mario Di Gioacchino[c], Claudio Marcelli[d], Giancarlo Della Ventura[b,d], Cyril Petibois[a]

[a] Université de Bordeaux, CNRS UMR 5248 CBMN, Allée de Saint-Hillaire, 33600 Pessac, France

[b] Dipartimento Di Scienze Geologiche, Universita Roma 3, Largo S. leonardo Murialdo 1, Roma, Italy

[c] Laboratorio di allergologia, Centro di Scienze dell'Invecchiamento (CeSI), Chieti, Italy

[d] INFN LNF, 40 Via Enrico Fermi, Frascati-Roma, Italy

[e] Dipartimento DIGAT, Università G. d'Annunzio, Via Dei Vestini 30, I-66013 Chieti, Italy

Abstract:

Interaction of asbestos fibers with human cells may cause lung diseases such as asbestosis and mesothelioma, whose severity is directly dependent on the cellular phenotypes involved. Details of this process remain largely unknown because of the chemical heterogeneity and morphology of the fibers and the requirement of organic-inorganic analytical means. We relate here on a research aimed at developing a dedicated synchrotron radiation IR (SR-IR) imaging methodology for analyzing the effect of asbestos fibers on cells with a 1×1 μm lateral resolution and with current ≥ 1.2 A for rapid acquisitions of high quality spectral images. The methodology has been tested on individual cells cultured directly on IR-transparent windows for transmission IR measurements after cryofixation. The experiments show that cell exposed to gradually increasing amounts of asbestos fibers up to 10μg/cm², and to different types of fibers, exhibit characteristic toxicity patterns that were found to correlate to IR signal changes; these changes are notably observed using amides absorption bands. Our results demonstrate that SR-IR imaging allows determination of subtle changes in cells exposed to inorganic species.

Key-words: cytotoxicity, IR imaging, asbestos fibers, methods

Abbreviations: EMP = Electron Micro Probe; FPA = focal-plane-array; IR = Fourier-transform infrared; SEM = scanning electron microscopy; SNR = signal to noise ratio; SR = synchrotron radiation

Introduction:

The term "asbestos" defines several naturally occurring hydrated silicates (see table 1 in [7]) which belong to two mineral groups: sheet silicates (chrysotile) and amphiboles (anthophyllite, tremolite, actinolite, amosite and crocidolite). Amosite and crocidolite are not mineralogical species, but terms used to denote the fibrous varieties of the amphiboles grunerite and riebeckite, respectively. Asbestos have been well identified as lung carcinogenic fibers. Some related pathologies include asbestosis and fibrosis or pleural plaques, which occur after a long and intensive exposure to the fibers; pleural or malignant mesothelioma may also occur following acute intense exposure. A hypothetical pathological process of asbestos carcinogenicity has been discussed on a previous paper [25]. According to several studies [26], the toxicity of the asbestos fibers mostly depends on the crystal morphology and dimension, commonly defined by the "aspect ratio", i.e. the length of a particle divided by its width. Following accepted regulations [27], a particle is considered to be a "fiber" when its dimensions exceed 5μm in length and less than 1.5μm in diameter and its aspect ratio is > 3:1. The reader is referred to Gunther et al. (2007) for a detailed discussion of the several problems involved in the definition of a "fiber" based on morphological concepts.

Factors other than morphology play a significant role in the toxicity of asbestos [28]. These are mainly related with the chemistry of the fiber, and particularly with its surface properties which ultimately control the electronic charge transfer or redox reactions with the lung cells [29, 30]. What seems clear is that the surface of the fiber is a dynamic system, i.e. ions as Fe^{2+} and Fe^{3+} are leached from the surface and may provoke the production of reactive oxygen species and reactive nitrogen species leading to the cancer as shown in figure 1. As a consequence, longer the fibers remain in the lung, more they are toxic; this feature is named "biopersistence". Moreover, the different fiber types may have different morphological features, such as chrysotile vs crocidolite, and these different fibers may interact differently with the cells. As a consequence, there are multiple fiber-cell interactions and responses. Therefore, the asbestos pathogenicity is not a simple feature, but a multivariate process occurring at different levels.

However, the study of interactions between cells and asbestos fibers is still underdeveloped [31]. This is due to methodological difficulties encountered since cells are organic systems while asbestos fibers are inorganic specimens. In analytical chemistry, characterizing both organic and inorganic compounds on the same sample is not trivial since techniques can hardly render information on both aspects at the same time. One analytical technique candidate to this challenge is vibrational spectroscopy, Fourier-transform infrared (IR) spectroscopy in particular, which is well suited for the analysis of both organic [32], and inorganic compounds [33]. The use of IR spectroscopy in biology has been developed during the past twenty years because of the several advantages of this technique, namely being global, non-destructive, and not requiring heavy sample preparation[34]. IR light is used as a probe beam with energy less than that of the visible light, thus one can obtain molecular information on the sample without significant modification of organic matter, and this is even more an advantage with respect to high-energy – ionizing - beam techniques, such as those based on X-rays and UV. However, IR spectroscopy has some disadvantages. A notable one is the necessity to remove the water from the specimen because it absorbs strongly the IR radiation and saturates detectors [11]. One can also mention the weak absorbance of some functional groups for which the data collection becomes extremely time consuming to get a reasonable signal to noise ratio (SNR) of spectrum [16]. Thanks to the development of bi-dimensional, focal-plane-array (FPA) detectors, IR spectroscopy nowadays allows to collect 2D infrared images *ex vivo* in a short time [35, 36]. This gives the opportunity to localize the different compartments of a cell and determine their molecular [37] arrangement. When coupled with high photon flux beams, such as those provided by synchrotron radiation (SR) sources, the problem of weakness of some IR bands can be efficiently overcome, thus significantly improving the spectral quality of spectral images [15, 38]. In this paper, we present recent studies in IR imaging coupled with synchrotron radiation with the goal of develop a dedicated method to analyze the interactions between inorganic environmental fibers (asbestos) and cells and provide a rationale of cell-asbestos studies for lung disease routine investigation (asbestosis).

Methods

Sample preparation: Three natural asbestos fibers were used for this work; all samples were selected from the collection of the Museum National d'Histoire Naturelle of Paris. The first is a "crocidolite" from Buchanawald (South Africa), labeled MNHN 134-86. Wavelength-dispersive microprobe analysis (WDS-EMP) gave a composition in the riebeckite fibers family, according the recent accepted nomenclature schemes for amphiboles **[39-41]**. Deviations from the end-member composition involved weak amounts of TiO_2, MgO, MnO and K. Both F and Cl were below the detection limit, thus suggesting an anionic composition equals to $(OH)_2$. The second is a cummingtonite, labeled MNHN 137.96; EMP data showed this sample to be very rich in Mn, with a composition actually close to the species mangano-cummingtonite ($Mn_2Mg_5Si_8O_{22}OH_2$). The third fibrous amphibole is an actinolite, labeled MNHN 104.624, with an intermediate Mg/Fe composition with respect to end-member tremolite.

Scanning electron microscopy (SEM) showed all samples to consist of very to extremely fibrous crystals, as it is typically the case of "crocidolite" from South Africa, which has an average dimensions < 1.0 µm in width (average 400-500 nm) and typically > 10 µm in length (and up to several tenths of µm; Fig. 1). Before the experiments, the fibers were hand ground in an agata mortar and baked at 250-300°C overnight to avoid chemical and/or biological contaminations due to handling procedures or from the environment. The amphibole powders were suspended in the cell medium and sonicated (Labsonic, 100 W, B. Braun Biotech International) for 5 minutes before each experiment. Preliminary tests showed no modification of the cell medium during the sonic treatment.

A critical aspect for *in vitro* cell-asbestos interaction experiments is controlling the concentration of fibers in the cell-culture medium, which should reproduce as close as possible the concentration usually observed in lungs of workers diseased by such chemical species [31]. The objective is also to define the concentration threshold for inducing cell stress due to the presence of fibers. Several tests at different conditions were made and carefully checked using SEM. The resulting solutions were deposited into petri dish on a Si window (previously deposited on petri dish surface), put at 30°C overnight and studied using a visible microscope and a conventional SEM XL30 from Philips (Netherlands) with computer-assisted operation. This system provides both secondary electron and backscattered electron detection, along with an integrated EDAX system. Three concentrations of asbestos fibers were used in this part of the study: 0.1 µg/cm^2, 1 µg/cm^2, and 10 µg/cm^2. Every solution was first sonicated for 60s, 5min, and 10min to obtain homogeneous dispersions of fibers. The number (by µm^2) and length of fibers, were calculated for each case from the SEM images with the software Ipwin60.

Cell culture: A dedicated cell culture method has been set up to allow a molecular analysis by IR imaging [42]. In this study, the cell line used was the type II epithelial lung cell Beas 2B (ATCC: CRL-9609v). Briefly, cells were grown in a DMEM/F-12 medium supplemented with 10% fetal calf serum, 1 g/L of glucose, glutamine, HEPES and antibiotics. Cells were routinely propagated in a humidified 5 % CO_2 atmosphere at 37°C. Serum-free culture were performed according to Barnes et al. [43]. The serum-free medium consists of a basal medium supplemented with 25 µg/mL HDL, 5 µg/ml insulin, 5 µg/mL transferrin, 2 ng/mL EGF, 1 mg/mL f-BSA and antibiotics. After a 24-hours exposure to different amounts of fiber,– 1 to 100 µg/cm^2 – cells were washed twice with PBS, harvested thanks to PBS-EDTA (10mM EDTA, pH=7.4) and counted adding trypan blue (Sigma) in each tube. The counting was done with the neubauer cell and chromium (concentration: 10^{-3}) was used as a positive control. The aim was to check the toxicity of the cells for different concentrations higher than 10µg/cm^2.

Flow cytometry: in parallel to the trypan blue counting; after the 24-hours exposure to the same different amounts of fiber – 1 to 100 µg/cm² – cells were washed twice with PBS, harvested thanks to PBS-EDTA (10mM EDTA, pH=7.4) and suspended in PBS-EDTA BSA (1% of BSA) and kept at 4°C. Then the cells were stained with 5 µl of Propidium Iodide (Sigma) was added for 30 min at 4°C in the dark and analyzed by flow cytometry. The use of chromium, to check if the experiment works well, is not necessary in this case because of the reliability of the apparatus.

Colorimetric assay: the cytotoxicity of each type of fiber and concentration was investigated by 3-(4,5-dimethylthiazol-2-yl)-2,5-diphenyl tetrazolium bromide (MTT). It's an alternative method for rapidly and indirectly determining cell viability based on metabolic activity. The assay measures the conversion of MTT to insoluble formazan by dehydrogenase enzymes of the intact mitochondria of living cells. A549 cells were seeded at a density of 5.10^3 cells/well into 96-well microplates for 24h. After treatment with the different concentrations of fibers for 24h, the medium was removed and 200 µl of MTT (Sigma) solution (5 mg/ml in PBS) were added to the plates and incubated for 3 h at 37 °C. After a centrifugation at 2000 rpm for 10 minutes, the liquid was removed and the formazan crystals were dissolved in 200 µl of DMSO (Sigma) for 30 minutes. The amount of formazan crystals formed correlates directly with the number of viable cells. Optical density (OD) was measured at 570 nm (reference filter 690 nm) using a UV-spectrofluorometer. Controls were grown in culture medium without treatments; their absorbance values were taken as reference values. Results were analyzed and expressed as percentage of the control (control equals 100%). Mean values of relative viability ± standard deviation (s.d.) were considered for statistical evaluations[44].

Cryofixation: Cells were grown on Si-supports for IR imaging measurements. Supports preparation prior to cell culture was sterilization (24h bath in ethanol + UV radiation for 15 minutes), the Si-supports were placed in 6-well plates. 3.10^4 cells with cell medium were added to each well with given amount of fibers – 10 and 50µg/cm². The use of these concentrations is related to the cytotoxicity experiment. Indeed, 10 µg/cm² is non-toxic concentration for the cells in contrast to 50 µg/cm². The cryofixation has been done 24 hours later following the method previously described [17]. Briefly, Si-supports were removed from petri dishes and washes twice with PBS to remove culture medium components before to be placed in sterile tubes and plunged in liquid N_2. Cells were further dehydrated in freeze chamber (-20°C) with laminar flux of dry air for a slow (12h) freeze-drying.

Fluorescence imaging: After sterilization of cover slips (in ethanol), we applied the same experimental condition than the cryofixation process. To be able to analyze the behavior of the cells with fiber, a 24-hour exposure with a fiber concentration of 10µg/cm^2 – non toxic concentration – was used. At the end, the cover slips were washed in PBS then fixed with 10% of PFA. Cells were double stained with the DAPI and phalloïdin-TRITC to probe respectively their nucleus (blue) and cytoplasm (red). Cells grown on glass coverslips were fixed with 2.5% paraformaldehyde and 5% sucrose in PBS for 10 minutes at room temperature, then permeabilized in 0.1% Triton X-100 in PBS, for 5 minutes. Coverslips were washed twice with PBS, blocked in 1% BSA in PBS and incubated for 1hour at RT with primary antibodies. Cells were rinsed in PBS and secondary antibodies and TRITC-phalloidin were added for 1hour at room temperature. Coverslips were permanently mounted in Mowiol (Calbiochem, VWR International, France) containing 4'6-diamidino-2-phenylindole (DAPI). Fixed cells were examined using a confocal laser scanning microscope (LSM 510, Zeiss) equipped with a 40X Plan Neo Fluor oil-immersion objective. From 4 pictures of each condition – control and 10µg/cm^2 - the area of 15 cells was calculated thanks to the software Image J. The aim was to check if there is any difference in the morphology of the cell.

IR imaging: Optical and IR images were performed with the same microscope with a 64x64 focal plane array (FPA) detector (Bruker Hyperion 3000, Germany) coupled to a IR spectrometer (Bruker Equinox 55, Germany) and a Globar source (Ø ~ 1 mm). IR spectra acquisitions were performed in transmission mode, using 256 co-added scans (4000-900 cm^{-1}), and an 8 cm^{-1} spectral resolution. N_2 purge was applied on both the microscope and the spectrometer for removing air contents absorption.

Individual cells were analyzed in triplicate per window with magnification level set at 15X (reconstructed image has pixel size of ~1.1x1.1 µm – see figure 4). From every 2D image, an average of 10*10 spectra corresponding to nucleus location was extracted and averaged. Then, integration of amides I (1720-1600 cm^{-1}) and II (1600-1490 cm^{-1}) absorption bands were performed using sub-routines of Opus 6.5 software (Bruker Germany). Amide II / I ratio was further calculated (figure 5).

Statistics: All experiments were performed in triplicate. Flow cytometric and trypan blue counting data are expressed, as a ratio of control, with the control value always equal to 100%. The statistical comparison between series of data for each time point was performed by Manova. The morphological difference between cells (nucleus) for the in fluorescence experiments was assessed by ANOVA. For IR imaging data, a Fischer test was used for Amide I / II ratio values changes with experimental conditions.

Results

Figure 1 shows the distribution of natural riebeckite fibers on Si-supports for concentrations ranging from 0.1 to 10 µg/cm². The Figure presents three concentrations – 0.1, 1 and 10 µg/cm² – with 10 minutes of sonication; apart for the 0.1 µg/cm² concentration, where 60 seconds was enough time of sonication. From these experiments, we found that 10 minutes of sonication time and 10 µg/cm² of concentration were the optimal set up to finally obtain a homogeneous distribution of the fibers on Si-supports with sufficient free space for cell growth, thus ensuring best condition for cell cultures to further determine cell-asbestos interactions.

We thus determined the cytotoxicity profile of the asbestos fibers. Experiments were performed using trypan blue counting, flow cytometry and MTT assay for cell viability tests are shown in Figure 2. Lethal dose of asbestos fiber for cells was found to start with 25 µg/cm², considering a 20% cell number decrease with respect to the control condition. The three tests used for assessing fiber toxicity on cells provided comparable results for all concentrations in culture medium ($p = 0.05$). Moreover, the MTT test revealed that fibers types presented the same cytotoxicity profile (change with concentration), but with a final toxicity per type being "crocidolite" > "actinolite" > "cummingtonite". Therefore a 10 $\mu g/cm^2$ of asbestos fibers was considered as useful for testing cell-fibers interaction as a "low" toxicity condition.

Fluorescence imaging of cells under different culture conditions, i.e., the controls and with 10 and 50 $\mu g/cm^2$ of asbestos fibers, are presented in figure 3. First, we imaged the fluorescence of the cells alone – Figure 3A and 3B – and found that all the nuclei are closed from each other, have round shape and behave like a 3D ball. The Figure 3C and 3D shows the fluorescence image of cells in interaction with 10$\mu g/cm^2$ of fibers. It could be observed that; 1) nuclei had inhomogeneous shape and were not round; 2) nuclei were found more distant; 3) cytoplasms were found like a 2D conformation and the cells spread to the cover slip now; 4) the cells took odd shape.

To control these results, the area of 15 cells was measured from figure 3A and 3C. Thanks to Anova ($p=0.010$) and the student test ($p=0.014$) it was found that the two groups of cells were statistically different.

IR imaging was used on 15 cell images for each experimental condition (Table 2). Each condition w

as found to exhibit significantly different amide I / amide II absorptions ratio for actinolite and cummingtonite at 10 and 50 $\mu g/cm^2$ ($P<0.05$) are crocidolite conditions were different between 10 and 50 $\mu g/cm^2$ ($P<0.05$).

Discussion

Before being able to study the interaction between asbestos fibers and cells by IR imaging, a series of preliminary experiments were necessary.

As a First step, the most appropriate sonication duration was sought to obtain regular repartition of the fiber on Si supports.. A 10-min sonication (power =100W) was sufficient to obtain a nearly complete disaggregation of fiber bundles. Moreover the knowledge of the number of cell for each concentration permits to understand why even a small amount of fibers – 50 µg / cm² – can be so toxic for the cell. Indeed for 10 µg / cm², we obtained ≈ $1.4*10^6$ fibers on a 1-cm² silicon wafer surface. With 50 µg/cm², the concentration became toxic, which has been previously reported [45, 46]

To confirm this first result, cytotoxicity assays allowed to demonstrate that fiber concentrations ranging between 1 to 25 µg / cm² could be used to analyze the effect of fibers without immediate toxicity. Another important issue was the cytotoxicity profile of the different types of fiber since this addresses the critical point of pathology relationship with fiber type. It was found that all asbestos fibers show the same cytotoxicity profile with concentration, but crocidolite was starting being toxic at 20 µg/cm², the other fiber types exhibiting equivalent toxicity at 25 µg/cm². One may argue that such concentration difference is not fundamental. Thus this result shows that it is rather the chemical composition that represents the main toxicity factor in asbestos fibers, which has been also suggested in other studies [47]. Another interesting feature related to cells morphology in presence of asbestos fibers. Fluorescence images revealed fiber effects on nuclei size with only 10 µg/cm². The change in nuclei size and shape revealed apoptotic process [46]. This result could be confirmed by IR imaging results, where amide I / II absorptions ratio from spectra corresponding to nucleus location in cells was also found different between conditions. Amide absorption changes is revealing protein content changed and protein and nucleic acids (DNA and RNA) conformational changed in cells submitted to stress [32, 48, 49]. IR spectroscopy has been the method of choice for studying various issues concerning structure[50]. In the 1800–1500 cm^{-1} region, bands originating from the base vibrations of the nucleic acid appear, acting as extremely sensitive markers for base pairing and base stacking effects. Proteins also cover this spectral interval and even contribute more to global IR absorption than nucleic acids. However, our results show direct correlation between shape changes in cells nucleus and amide I, amide II and amide I / amide II absorption ratio. Therefore in our study, we can consider this spectral interval as a global indicator of cellular changes induced by fiber toxicity.

Moreover, by comparing the results obtained from different types of fibers and concentrations, we observed that the molecular change induced on cells could be differentiated – see Table 2. The changes due to the interaction with different types of fibers for amide I, amide II and amide I / amide II were equivalent as shown by evolution of the mean value. Thus, the ratio amide I / amide II can be considered as a marker of cellular stress induced by the asbestos fibers. In addition, actinolite and cummingtonigte at 10 and 50µg / cm² reveal no statistic difference between them, for amide I, and this can be related to the cytotoxicity profile shown in figure 2. As revealed in the Table 2, The lipids integration, in the range of wavenumbers from around 2820 to 2996 cm^{-1} (lipid massif) used for the determination of lipids distribution [51], demonstrate that there is an increase and then a decrease of the global lipids content and this result can be correlated to the ratio of protein to lipids content, which increase with the concentration of fibers. Indeed, an high ratio of protein to lipids content explain an enhance of cellular proliferation[52, 53], result already exposed by cytotoxicity assay[54] . These differences in molecular changes could be explained by the difference in chemical composition of fibers, notably considering the Fe2+/Fe3+ contents of fiber – see table 1 in [31]. It is known that both presence and structural coordination of iron are important factors in the toxicity of asbestos [55]. It has been shown that five different tremolite fibers presented different toxicity levels correlated to Fe2+ vs. Fe3+ contents [47].

Conclusion

Thanks to this worked, we were able to study the interactions between lung cells and asbestos fibers. The interest was to demonstrate the ability of IR imaging to combined organic information with inorganic information. Therefore, the critical point is that IR imaging is able to show the molecular changes in one cell. Thanks to IR imaging, we were able to find the changes due to asbestos fibers to a cell and confirm the results with complementary results. Thus, we were able to go further and analyse the relative toxicity of different type of fibers with lung cells. Proud of these results, the next step will be the use of the synchrotron light to enhance the results and make in vivo experiments to analyze the dynamic change in a cell.

Acknowledgements:

The authors are indebted to the 'Italian-French University" (Vinci program 2009) for their financial supports. The authors thank the DMPFCS group at CNRS UMR 5248 CBMN for the material support.

References:

1. Yao, S., G. DellaVentura, and C. Petibois, *Analytical characterization of cell-asbestos fiber interactions in lung pathogenesis.* Anal Bioanal Chem. **397**(6): p. 2079-89.

2. Stanton, M.F., et al., *Relation of particle dimension to carcinogenicity in amphibole asbestoses and other fibrous minerals.* J Natl Cancer Inst, 1981. **67**(5): p. 965-75.

3. *Asbestos, asbestosis, and cancer: the Helsinki criteria for diagnosis and attribution.* Scand J Work Environ Health, 1997. **23**(4): p. 311-6.

4. Van Oss, C.J., *Hydrophobic, hydrophilic and other interactions in epitope-paratope binding.* Mol Immunol, 1995. **32**(3): p. 199-211.

5. Broaddus, V.C., et al., *Asbestos induces apoptosis of human and rabbit pleural mesothelial cells via reactive oxygen species.* J Clin Invest, 1996. **98**(9): p. 2050-9.

6. Adachi, S., et al., *Inductions of oxidative DNA damage and mesothelioma by crocidolite, with special reference to the presence of iron inside and outside of asbestos fiber.* Carcinogenesis, 1994. **15**(4): p. 753-8.

7. Yao, S., G. Dellaventura, and C. Petibois, *Analytical characterization of cell-asbestos fiber interactions in lung pathogenesis.* Anal Bioanal Chem, 2010. **397**(6): p. 2079-2089.

8. Petibois, C. and G. Deleris, *Chemical mapping of tumor progression by FT-IR imaging: towards molecular histopathology.* Trends Biotechnol, 2006. **24**(10): p. 455-62.

9. Amirouche-Korichi, A., M. Mouzali, and D.C. Watts, *Effects of monomer ratios and highly radiopaque fillers on degree of conversion and shrinkage-strain of dental resin composites.* Dent Mater, 2009. **25**(11): p. 1411-8.

10. Kondepati, V.R., H.M. Heise, and J. Backhaus, *Recent applications of near-infrared spectroscopy in cancer diagnosis and therapy.* Anal Bioanal Chem, 2008. **390**(1): p. 125-39.

11. Petibois, C., et al., *A bright future for synchrotron imaging.* Nat Photonics, 2009. **3**(4): p. 179.

12. Petibois, C. and B. Desbat, *Clinical application of IR imaging: new reasons for hope.* Trends Biotechnol, 2010. **28**(10): p. 495-500.

13. Petibois, C., et al., *Analysis of type I and IV collagens by FT-IR spectroscopy and imaging for a molecular investigation of skeletal muscle connective tissue.* Anal Bioanal Chem, 2006. **386**(7-8): p. 1961-6.

14. Heraud, P., et al., *Focal plane array infrared imaging: a new way to analyse leaf tissue.* New Phytol, 2007. **173**(1): p. 216-25.

15. Petibois, C., *Imaging methods for elemental, chemical, molecular, and morphological analyses of single cells.* Anal Bioanal Chem. **397**(6): p. 2051-65.

16. Petibois, C., *Imaging techniques with synchrotron radiation.* Anal Bioanal Chem. **397**(6): p. 2031-2.

17. Petibois, C. and M. Cestelli Guidi, *Bioimaging of cells and tissues using accelerator-based sources.* Anal Bioanal Chem, 2008. **391**(5): p. 1599-608.

18. Leake et al., B.E.L., A.R. Wooley, W.D. Birch, E.A.J. Burke, G. Ferraris, J.D. Grice, F.C. Hawthorne, H.J. Kisch, V.G. Krivovichev, J.C. Schumacher, N.C.N. Stephenson and E.J.W. Whittaker, *Nomenclature of amphiboles: additions and revisions to the International Mineralogical Association's amphibole nomenclature.* Min. Mag., 2004. **68** (1): p. pp. 209–215.

19. Hawthorne, R.O.F.C., *Classification of the Amphiboles.* Reviews in Mineralogy and Geochemistry, 2007. **67**(1): p. p. 55-88.

20. Barghawa, R.L.I., Anal Chem, 2001. **73**: p. 5157-5167.

21. Petibois, C., et al., *Synchrotron radiation IR imaging in minutes: a first step towards real-time cell imaging.* Anal Bioanal Chem, 2010. **397**(6): p. 2123-9.

22. Loo, D.T., et al., *Extended culture of mouse embryo cells without senescence: inhibition by serum.* Science, 1987. **236**: p. 200-202.

23. Mosmann, T., *Rapid colorimetric assay for cellular growth and survival: application to proliferation and cytotoxicity assays.* J Immunol Methods, 1983. **65**(1-2): p. 55-63.

24. Petibois, C., et al., *Facing the challenge of biosamples IR imaging using the synchrotron radiation source.* J Synhrotron Rad, 2010. **17**(1): p. 1-11.

25. Giantomassi, F., et al., *Biological effects and comparative cytotoxicity of thermal transformed asbestos-containing materials in a human alveolar epithelial cell line.* Toxicol In Vitro, 2010. **24**(6): p. 1521-31.

26. Pugnaloni, A., et al., *Effects of asbestiform antigorite on human alveolar epithelial A549 cells: a morphological and immunohistochemical study.* Acta Histochem, 2010. **112**(2): p. 133-46.

27. Pacella, A., G.B. Andreozzi, and J. Fournier, *Detailed crystal chemistry and iron topochemistry of asbestos occurring in its natural setting: A first step to understanding its chemical reactivity.* Chemical Geology, 2010. **277**(3-4): p. 197-206.

28. Malins, D.C., et al., *Antioxidant-induced changes in oxidized DNA.* Proc Natl Acad Sci U S A, 2002. **99**(9): p. 5937-41.

29. Malins, D.C., N.L. Polissar, and S.J. Gunselman, *Infrared spectral models demonstrate that exposure to environmental chemicals leads to new forms of DNA.* Proc Natl Acad Sci U S A, 1997. **94**(8): p. 3611-5.

30. Banyay, M., M. Sarkar, and A. Graslund, *A library of IR bands of nucleic acids in solution.* Biophys Chem, 2003. **104**(2): p. 477-88.

31. Chwiej, J., et al., *Synchrotron IR micro-spectroscopy study of the rat hippocampal formation after pilocarpine-evoked seizures.* J Chem Neuroanat, 2010. **40**(2): p. 140-7.

32. Mourant, J.R., et al., *IR spectroscopy demonstrates biochemical differences in mammalian cell cultures at different growth stages.* Biophys J, 2003. **85**(3): p. 1938-47.

33. Szalontai, B., et al., *Membrane dynamics as seen by Fourier transform infrared spectroscopy in a cyanobacterium, Synechocystis PCC 6803: The effects of lipid unsaturation and the protein-to-lipid ratio.* Biochimica et Biophysica Acta (BBA) - Biomembranes, 2000. **1509**(1–2): p. 409-419.

34. Adamson, I.Y., *Early mesothelial cell proliferation after asbestos exposure: in vivo and in vitro studies.* Environ Health Perspect, 1997. **105 Suppl 5**: p. 1205-8.

35. Bonneau, L., et al., *Studies on surface properties of asbestos. I. Active sites on surface of chrysotile and amphiboles.* Environ Res, 1986. **41**(1): p. 251-67.

Figures:

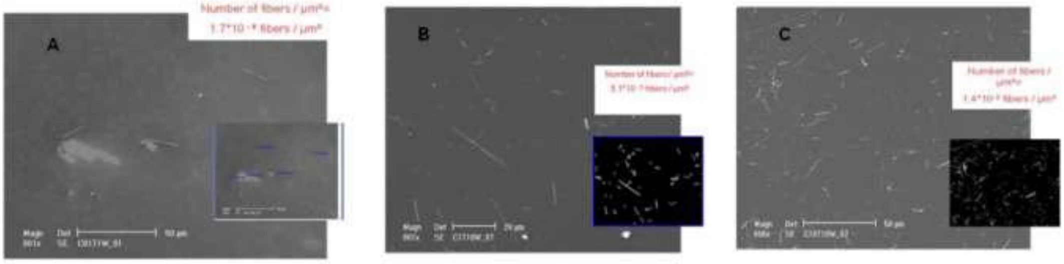

Figure 1: SEM images at different concentrations of crocidolite fibers with the number of fiber/ µm² (A: 0.1 µg/cm²; B: 1 µg/cm² and C: 10 µg/cm²) in water.

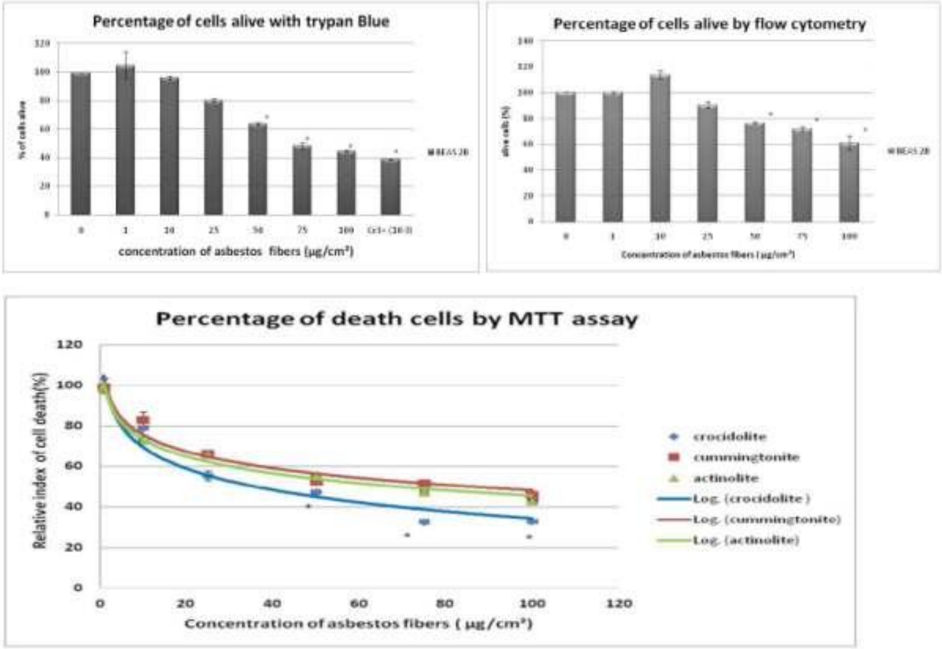

Figure 2: Percentage of cells alive counting by trypan blue (n=3), flow cytometry (n=5) and MTT assay (n=3). * = significantly different from control (0 µg.cm^{-1}); $p < 0.05$.

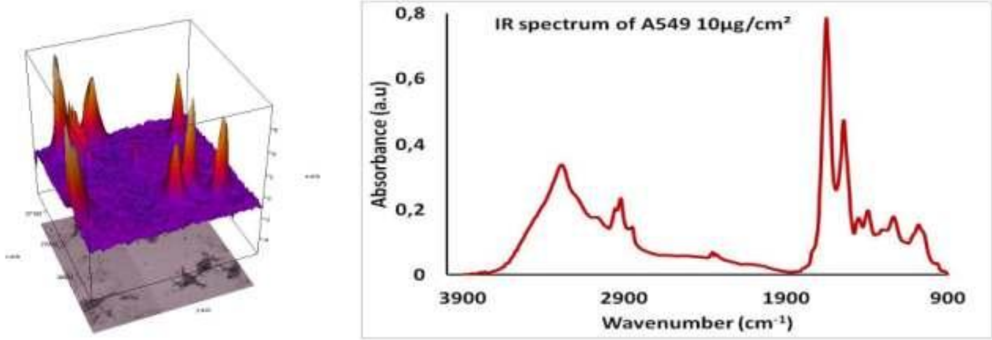

Figure 5: IR imaging and the IR spectrum extracted. 36X, 256 scans, Resolution 8cm^{-1}.

Fibers concentration	*Amide 1*	*Amide 2*	*Amide1/Amide2 ratio*	*lipids*	*Amide 1/ Lipids ratio*
control	3.26 ± 1.60	1.27 ± 0,26	2.61 ± 0,1	1.52 ± 0,41	2.26 ± 0,56
crocidolite 10µg*	6.90 ± 0,66	3.46 ± 0,33	2.01 ± 0,02	3.26 ± 0,24	2.15 ± 0,17
crocidolite 50µg*	7.31 ± 0.44	3.80 ± 0,19	1.93 ± 0,01	2.31 ± 0,14	3.25 ± 0,33
actinolite 10µg*	5.79 ± 0,579	2.49 ± 0,48	2.36 ± 0,14	2.91 ± 0,40	2.04 ± 0,18
actinolite 50µg*	6.34 ± 0.66	3.03± 0,16	2.1± 0,02	2.51 ± 0,46	2.64 ± 0,31
Cummingtonite 10µg*	5.96 ± 1.367	2.69 ± 0,27	2.21 ± 0,02	1.69 ± 0,19	3.78 ± 0,50
Cummingtonite 50µg*	6.73± 0,78	3.44± 0,08	2.01± 0,02	1.36± 0,14	5.16± 0,83

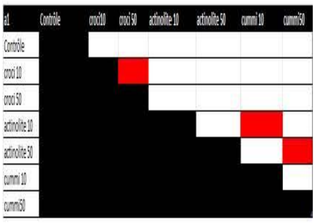

a1	Contrôle	croci10	croci 50	actinolite 10	actinolite 50	cummi 10	cummi50
Contrôle	⬛						
croci 10	⬛	⬛	🟥				
croci 50	⬛	⬛	⬛				
actinolite 10	⬛	⬛	⬛	⬛		🟥	
actinolite 50	⬛	⬛	⬛	⬛	⬛		🟥
cummi 10	⬛	⬛	⬛	⬛	⬛	⬛	
cummi50	⬛	⬛	⬛	⬛	⬛	⬛	⬛

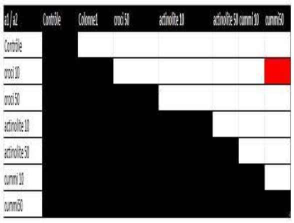

a1 / a2	Contrôle	Colonne1	croci 50	actinolite 10	actinolite 50	cummi 10	cummi50
Contrôle	⬛						
croci 10	⬛	⬛					🟥
croci 50	⬛	⬛	⬛				
actinolite 10	⬛	⬛	⬛	⬛			
actinolite 50	⬛	⬛	⬛	⬛	⬛		
cummi 10	⬛	⬛	⬛	⬛	⬛	⬛	
cummi50	⬛	⬛	⬛	⬛	⬛	⬛	⬛

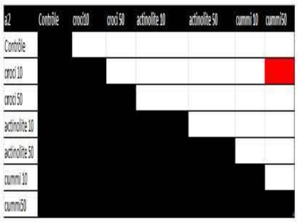

a2	Contrôle	croci10	croci 50	actinolite 10	actinolite 50	cummi 10	cummi50
Contrôle	⬛						
croci 10	⬛	⬛					🟥
croci 50	⬛	⬛	⬛				
actinolite 10	⬛	⬛	⬛	⬛			
actinolite 50	⬛	⬛	⬛	⬛	⬛		
cummi 10	⬛	⬛	⬛	⬛	⬛	⬛	
cummi50	⬛	⬛	⬛	⬛	⬛	⬛	⬛

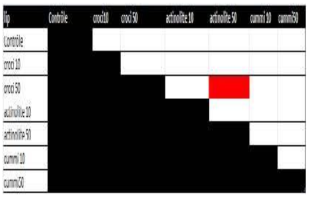

lip	Contrôle	croci10	croci 50	actinolite 10	actinolite 50	cummi 10	cummi50
Contrôle	⬛						
croci 10	⬛	⬛					
croci 50	⬛	⬛	⬛		🟥		
actinolite 10	⬛	⬛	⬛	⬛			
actinolite 50	⬛	⬛	⬛	⬛	⬛		
cummi 10	⬛	⬛	⬛	⬛	⬛	⬛	
cummi50	⬛	⬛	⬛	⬛	⬛	⬛	⬛

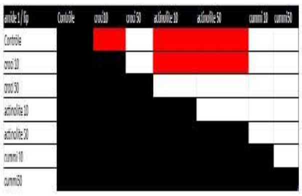

amide 1 / lip	Contrôle	croci10	croci 50	actinolite 10	actinolite 50	cummi 10	cummi50
Contrôle	⬛	🟥		🟥	🟥		
croci 10	⬛	⬛		🟥	🟥		
croci 50	⬛	⬛	⬛				
actinolite 10	⬛	⬛	⬛	⬛			
actinolite 50	⬛	⬛	⬛	⬛	⬛		
cummi 10	⬛	⬛	⬛	⬛	⬛	⬛	
cummi50	⬛	⬛	⬛	⬛	⬛	⬛	⬛

Table 2: Spectral integrations and statistical tables' results of amides I and II (1720-1490 cm^{-1}) bands for amide I/II ratio calculation. ^{a}= Control significantly different 10 and 50 µg/cm² for each type of fiber; red block = No significantly different.

CELLULAR TOXICITY OF AMPHIBOLES IS FIBER LENGTH DEPENDENT

Objectives: The goal of this work was to study the interaction between asbestos fiber and single living cell in vitro using high resolution Raman spectroscopy as a probe.

The project was firstly focused at realizing for the first time a safe 3D Raman spectrum of a single living cell, and then at obtaining the spectra after adding asbestos fibers to the system such as to monitor the behavior of single cells in contact with inorganic materials.

The use of Raman spectroscopy was designed for multiple reasons. The first is the possibility to perform in vitro experiments which is the main purpose of the study. The second is that with this spectroscopic technique one has the possibility to achieve chemical information from both the inorganic (fiber) and organic elements (lung cell) in the system. We could obtain direct images of the interaction between cells and fibers by plotting the intensity of a particular Raman bands. In addition, the modern spectrometers allow extremely fast data collections and this is a crucial point in experiments were there is the need to prevent the degradation of the biological materials and monitor of phenomena compatible with biological time – 20 minutes. The final great advantage of Raman spectroscopy is the high lateral resolution of 700nm permitting to visualize and track change occurring at sub cellular components, i.e. are at a sub-micrometer scale.

For this work, the suitable experimental conditions allowing the interaction between living cells and asbestos fiber and then the monitoring of this interaction were investigated. Cells were grown in a Dulbecco’s Modified minimum Essential Medium; a concentration of 40.10^3 cells / well was added into 6-wells plates and cultivated on Si wafer. We incubated with this concentration of cells 5µg / cm² of asbestos fibers for 24h. These amounts were chosen to respect two conditions: 1- the cells must be distant from each other to allow a single cell observation by Raman spectroscopy 2-fibers concentration such as to allow the physical interaction with a cell. The spectra were acquired using 70*70 (points per line*line per image) sample area for the XY mapping with a scan speed of 14 s/line and an integration time of 0.2 s. For Z-stack images, the number of layers was determined such as to obtain a final difference of 800nm between layers.

Before analyzing the data, a pre-processing study was realized thanks to the software Witec Project 2.06 (Witec, Germany). The baseline was subtracted from each mapping with a polynomial of 0 order for a constant offset and the Si substrate peaks were removed from the whole spectrum. Then the patterns were smoothed using a Savitsky-Golay filter of 3rd order to reduce the electronic noise to a signal. Indeed, SG is proved useful to reduce the noise levels of spectroscopic data [85]. It's important to note that the order of SG can influence the peak intensity.

Once determined the marker bands for the cells and asbestos fiber, respectively, we obtained several images of asbestos within the single cell. The most interesting result from the images is that the small fibers can be apparently well internalized by the cell, while larger fibers are not internalized. In order to confirm or infirm the result, multivariate statistical analysis as principal component analysis and clustering analysis have been performed. Thus, the use of these statistical techniques led to the detection of the mechanism of defense of the cells in contact with asbestos fiber.

In summary, the use of Raman spectroscopy allows to obtain simultaneously morphological and chemical information leading to the determination of the mechanism of defense of single living cells interacting with asbestos fiber.

This work is summarized in a manuscript given below which will be submitted.

Cellular toxicity of amphiboles depends on fiber aspect ratio

Yao Seydou [1], Giancarlo Della Ventura [2], Cyril Petibois [1]

Amphiboles caused cohorts of deaths in exposed workers, leading to some of the largest class actions in the industry. Once inhaled, these inorganic fibers are thought to be both chemically and morphologically toxic, and their biopersistence in lungs over decades lead to progressive pathologies, mesothelioma and asbestosis. However, this exceptionally long chronicity for human pathologies suggests that chemical toxicity is certainly low, making that morphological parameters could be more relevant in the pathology. Here, we developed a 3D Raman/optical imaging methodology *in vitro* to characterize both morphological and chemical parameters of cell/fiber interactions. We determined that lung cells could vesiculate amphiboles with length below 5 µm or could embed those not exceeding 15 µm in their fibrous extracellular matrix. Lung cells can thus develop defense strategies for handling the biopersistence of inorganic species, which may thus have major impact for biosafety issues related to nanomaterials.

Correspondence and requests for materials should be addressed to C.P. (email: c.petibois@cbmn.u-bordeaux.fr). 1: Université de Bordeaux, CNRS UMR 5248, Allée de St Hillaire, 33600 Pessac-Cedex, France. 2: Dipartimento Scienze Geologiche, Università Roma Tre, I-00146 Roma, Italy.

Acknowledgements: We thank E. Harte for the training on Raman imaging system. This work is supported by the "Ligue Nationale contre le cancer" and the VINCI-2009 PhD fellowship program from French-Italy University (UFI).

Author contributions: G.D.V. and C.P. designed the experiments; Y.S. and C.P. performed and analyzed the experiments; Y.S. and C.P. wrote the paper.

Amphiboles refer to asbestos fibers, a group of six naturally occurring fibrous silicate minerals. These minerals have been widely used in the industry because of their exceptional physical and chemical properties, thus resulting in their significant presence in the environment, as airborne dust particles. However, these fibers cause deadly lung pathologies as asbestosis or mesothelioma if inhaled in large amounts [1, 2]. The details on the pathological pathways remain largely unknown due to the heterogeneity in chemistry and morphology of these materials. Indeed, the toxicity of these fibers depends not only on their morphology and dimension, commonly defined by the "aspect ratio", i.e. the length of a fiber over its width, but also by their dynamic surface chemistry and the duration of their "biopersistence" into the lung [3, 4]. These multiple factors in these fiber-cell interactions make challenging the understanding of the related lung pathologies.

It is also noteworthy that morphological and chemical parameters of amphiboles toxicity on lung cells are usually investigated separately, thus prohibiting any conclusion about their relative impact on pathologies occurrence and development. And, one must also consider that both morphological and chemical toxicities are families of heterogeneous parameters with potential effects varying according to cell phenotypes. A known consequence of this lack of knowledge is that experts could not be convincing when litigations appeared during the resounding calls actions setup against companies that produced amphiboles-derived products during the last century. First of all, the extremely long pathological processes observed in amphiboles-related pathologies makes doubtful the fact that all species are equally toxic, which is relayed by epidemiological studies that reported heterogeneous morbidity impact according to the geological origin of amphiboles and their chemistry and/or morphology [2, 3]. A second issue relates to the abnormally long delay between amphiboles exposure and occurrence of pathologies, sometimes after decades. It is thus unlikely that chemical toxicity of fibers can be the major parameters in the pathology induction [4]. However, this does not mean that fibers toxicity plays a significant role in the pathology development, according to their pro-oxydant properties for example [5-7].

Face to the known or supposed chemical and morphological toxicities of amphibole fibers accumulated in lungs, one must also consider that lung cells, and particularly the epithelial ones, can develop a defense mechanism when they must interact persistently with nano-objects [8]. Indeed, carbon nanoparticles can be uptake by epithelial lung cells into vesicles, which is likely to reduce significantly their toxicity [9, 10]. It is also known that lung cells have an exceptional ability to handle the systematic overexposure to reactive oxygen species (ROS) occurring at the air/cellular space interface during breathes. It is thus likely that toxicity of ROS released by inorganic materials accumulating in lungs can be at least partially controlled by cells. The analysis of cell/fiber interactions to understand the pathogenicity of amphiboles thus requires the utilization of analytical techniques able to characterize both organic (cells) and inorganic (fibers) parameters in 3D and possibly *in vitro*. In addition, such analytical technique should allow a sub-micron lateral resolution for detecting fibers (usual length of biopersistent fibers in lung is 0.1-3 µm width and 1-100 µm length) in cells. Finally, the technique must also produce the 3D image (a stack of 2D images) in delays compatible with the biology of the cell, i.e. 15-20 minutes maximum (for motility purposes notably). Thanks to the recent technological development of Raman microscopy with fast-acquisition detector, it's now possible to collect 2D images with a high resolution (ca. 250 nm) in a confocal-like mode, thus allowing to obtain 3D reconstruction image from a stack of 2D images of a living cell.

Only few groups have succeeded 3D Raman imaging of single living cells and analyze *in vitro* the chemical and morphological changes from single living cells using Raman spectroscopy [11, 12]. Studies based on single cells analyses were mainly based on the change of proportions of nucleic acid and proteins [13, 14] or the difference of distribution of macromolecule [15, 16]. In general, most of these groups worked using fixed [17] cells as reference for the study but it became impossible to monitor a biological process over the time and be sure that the change is not due to the fixation method [18, 19]. Other groups worked with living cell but by using the SERS [20, 21] or the CARS techniques [22] with a red laser source to avoid overheat of the sample. However, in this configuration, only poor spectral information can be obtained, thus limiting the interpretation and interest of results [23]. At present, only one group [24] has been successful in studying the cell response to a chemotherapy drug treatment at single cell level using living cells and a 532 nm laser source. They observed spectral differences in the RNA and DNA regions (800 and 1800 cm^{-1}) by using Raman micro spectrometry but they obtained very poor intensities in the patterns. However, no study has reported the analysis of both organic and inorganic parameters to describe a cell / nanomaterial interaction using Raman microscopy *in vitro*.

Here, we report the behavior of lung living cells in interaction with different species of asbestos fibers (natural and synthetic). Gradual concentrations of fiber were used for testing their toxicological effect on cells. Fast-acquisition 3D Raman and optical (Rayleigh) images allowed determining the interaction between an individual cell and a fiber according to its aspect ratio.

RESULTS

Raman spectra were used to obtain a spectral marker related to each asbestos fiber type as shown in figure 1.

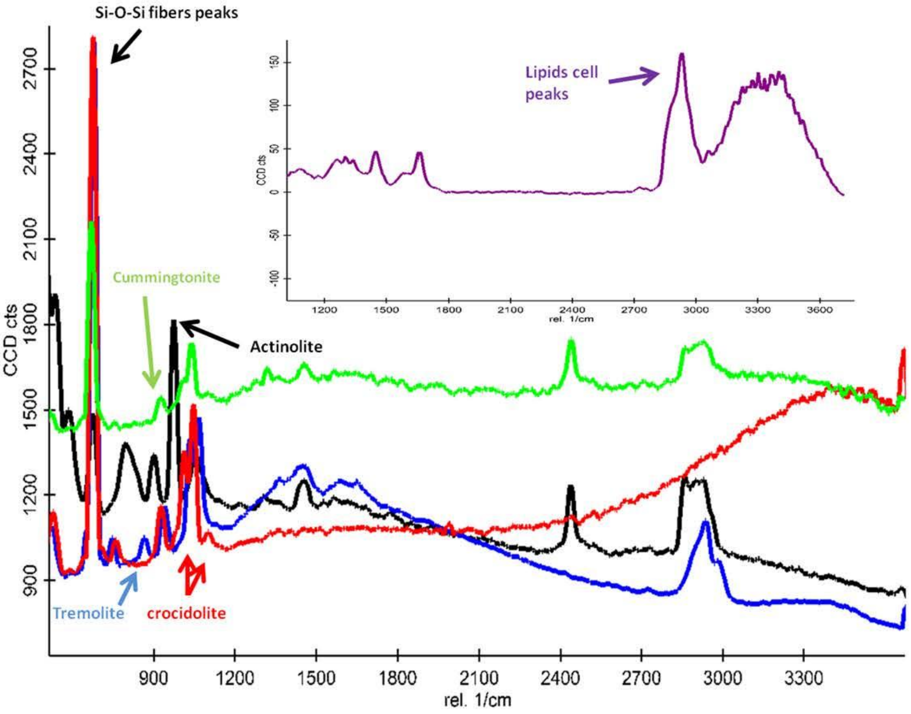

Fig 1: Raman Spectra of Asbestos fibers used in this study - Tremolite (blue), crocidolite (red), actinolite (black) and cummingtonite (green). The black arrow corresponds to the common band of all fibers. The inserted spectrum refers to the A549 cell spectrum located in the nucleus region. Rel.1/cm = Raman shift in cm^{-1} , λ_{exc}= *520.1* cm^{-1}

All fibers have in common an intense band between 650 and 710 cm^{-1} – assigned to the Si-O-Si stretching mode. Thus, this spectral region can be used as a marker for presence of asbestos fibers in cellular environment. Specific bands could be also considered as fingerprint for each asbestos fiber type, such as 862 cm^{-1} for tremolite, 1023 and 1050 cm^{-1} for crocidolite, 925 cm^{-1} for cummingtonite, and 972 cm^{-1} for actinolite [25]. As observed in figure 1, the inserted Raman spectrum of a lung cell obtained *in vitro* shows that ν_{as} (CH_2), and ν_{as} (CH_3) is well defined between 2830-3000 cm^{-1}. It is also noteworthy that characteristic band of fibers detailed above are not overlapping major vibrational band observed for the cells due to the nature of the materials (inorganic / organic) regions for cells.

Lung cells were cultured on non-toxic Si wafers [26] with gradual concentrations of asbestos fibers (1 to 100 µg/cm^2). Toxicity assays revealed that 10 µg/cm^2 concentration of asbestos fiber induced moderate toxicity while a concentration up to 20 µg/cm^2 became highly toxic with at least 10 % of cell deaths. The 3D *in vitro* analysis of live cells was performed in less than 30 minutes by first collecting a series of 2D Rayleigh images at a 250-nm lateral resolution every 100 nm on the Z-axis from sample holder surface. In this acquisition time, 3D images were also obtained and reconstructed from series of fast-acquisition 2D Raman images covering the thickness of cells from sample holder surface with a 250-nm spatial resolution, typically for 7 µm in the Z-axis and a 30*30 µm surface (1200*1200 spectra per 2D image) – figure 2. To restrict the total acquisition time to 30 minutes, 2D Raman images could be obtained with 300 to 700 nm Z intervals, with a final stack of 8-12 images. An optical video of cells was obtained before and after 3D image acquisitions to verify the positioning and viability of cells (see supplementary material n°1 and n° 2).

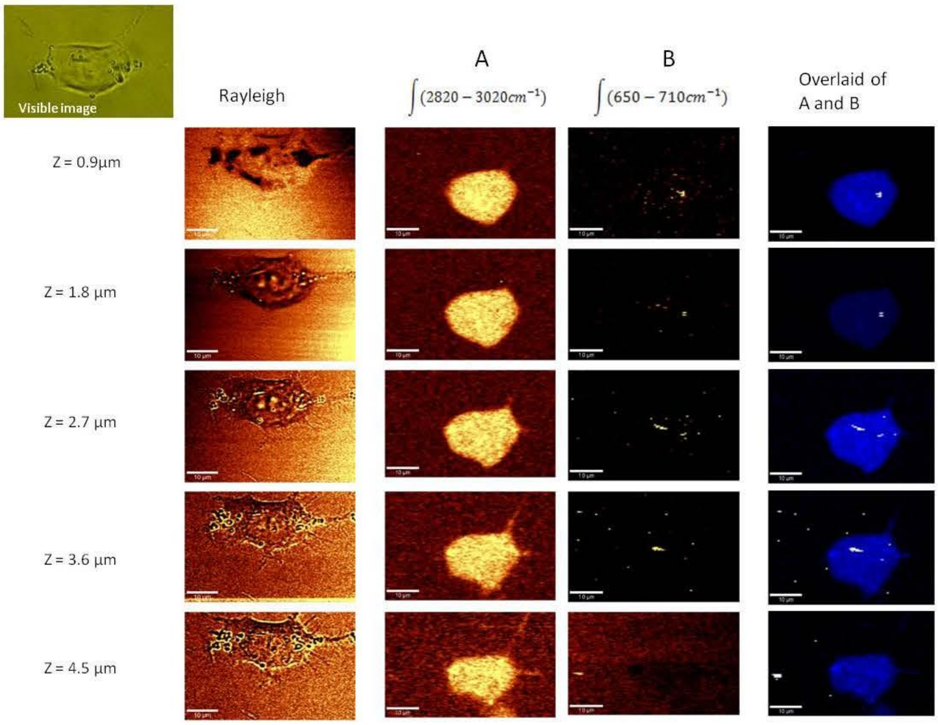

Fig XX : Rayleigh images of A549 cell and visible corresponding image. Raman XY images reconstructed at different Z levels from integrating the intensities of A) the ν(C-H) 2820 cm^{-1} – 3020cm^{-1} range assign mainly to the C-H stretching of lipids and B) the ν (Si-O) stretching peaks 650–710 cm^{-1} range characteristic of the fiber. Then the overlaid of A) and B) from Raman images with fiber (650–710cm^{-1}) in white and lipids (2820–3020 cm^{-1}) in blue for each Z. Scale bar for the Rayleigh and Raman image: 10µm.

The 3D reconstructed images allowed determining precisely the position of fibers inside or outside the cells (see supplementary material n°3). A total of 39 measurements with video of cells confirming their viability and positioning after acquisitions were done and allowed determining the location of fibers with respect to their length (table 1). A first major result was that only the asbestos fibers not exceeding 5 µm in length could be found located in the cytosol or totally embedded in ECM while those having larger length up to 15 could be found only embedded in ECM. These fibers were thus totally isolated from chemical interactions with the intracellular and extracellular space. Conversely, fibers exceeding 15 µm in length could be found located across the cell or not totally embedded in the ECM, suggesting still possible interaction with extracellular space. One may note in this situation of *in vitro* experiments, i.e., without the deformation of ECM due to lung movements in breathes, that all fibers remained isolated from intracellular space. These movements are not likely to change significantly the situation of found inside cytosol and possibly limit mechanical constrains from those totally embedded in ECM.

Fiber Size	**ECM**	**Cytosol**	**Across**
0 - 5 µm	**5**	**5**	
5 - 10 µm	**17**		
10 - 15 µm	**6**		
15 - 20 µm			**6**

Table 1: Location of amphiboles found at the contact of cells according to fiber length. N = 39. . Fibers found externalized (n=6) correspond to fibers partially embedded in ECM (n=3) or partially vesiculated (n=3).

The main aim of this study was to determine the chemical-structural interface formed by cell/fibers interaction. To address this point, a multivariate statistical analysis was performed using principal component analysis (PCA) and clustering analysis (CA) on the stacks of 2D Raman images obtained for 3D image reconstruction. The goal was to use the specific cellular and fiber Raman absorptions described in figure 1 to determine how cells could sequestrate or embed the fibers with respect to their length (figure 3). Using these specific Raman markers, it was possible to reconstruct 2D and 3D images highlighting the incorporation of short-length asbestos fibers into vesicles as stronger lipid was observed at the immediate vicinity of fibers inside cytosol. This vesiculation suggests that fibers were totally isolated from other intra-cellular space component in cells. The fibers found embedded in ECM were also presenting stronger amide one vibration mode at their immediate vicinity, thus suggesting the development of a fibrous matrix to isolate fibers from extra- and intra-cellular matrix (see supplementary material n°3).

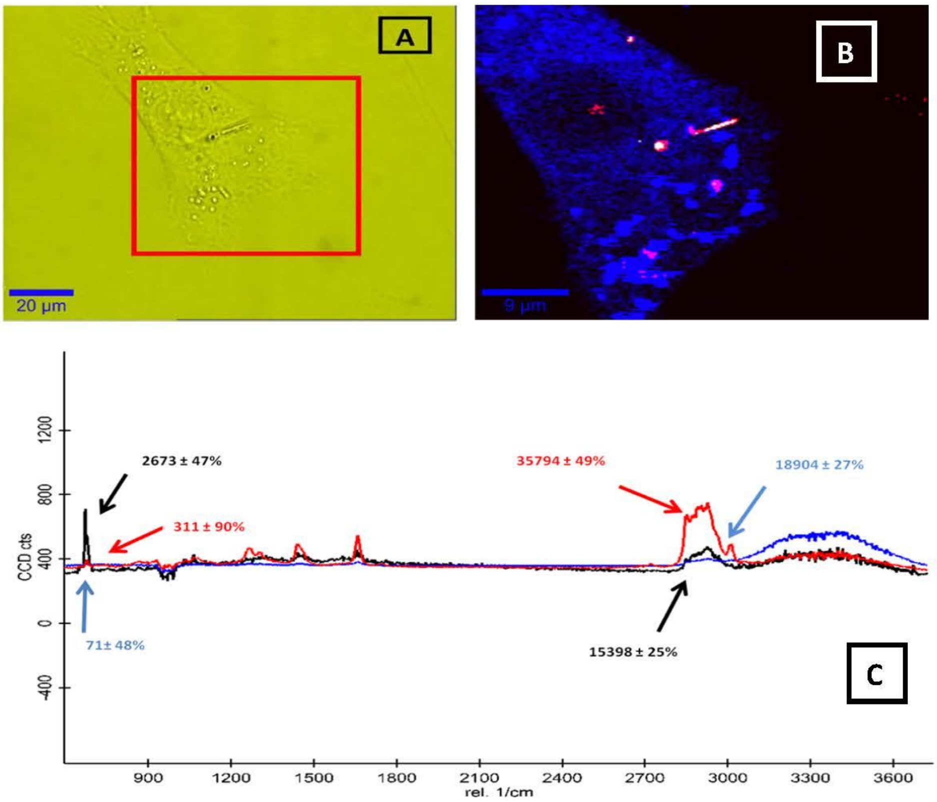

Fig 3: A) Visible image the target of cell B) combined image of the cell (in blue), the fiber (in white) and a vesicle (in red); z=1.5µm C) Spectra of each component from (B): cell spectrum in blue, fiber spectrum in black and the vesicle spectrum in red. Integration values (a.u., average ± standard deviation) *from the lipids and asbestos fiber spectral region for each class*

of spectra are above the colored arrow. The red box corresponds to the Raman microscopy area of interest.

DISCUSSION

With the advent of the nanoworld in the industry, analyzing the interaction between cells and nanomaterials has become a major paradigm for health issues. In fact, one may consider that this issue has been raised to the population through the large class action lawsuits engaged against companies exploiting amphiboles during the second part of 20th century, which made dying about 750000 workers from mesothelomia and asbestosis [27-30]. These class actions typically were filed against companies that knew the dangers of asbestos exposure but did not inform employees of the risks. Now, the question is permanently raised against industry-related nanoproducts, which have become ubiquitous to our life environment. It has thus become necessary to follow the development of the nanomaterials-related products and help this industrial area to provide the expected safety certifications before place on the market or use. In this study, our aim was to investigate the effects of chemical and morphological parameters of micro-sized asbestos fibers on cells *in vitro*, thus requiring the utilization of a microscopy technique able to provide both organic information and inorganic information from cells and fibers, respectively. Raman microscopy is a spectroscopy-related technique providing such information with which an *in vitro* methodology could be proposed [31-33]. The 3D Rayleigh image acquisition allowed first a fast visualization of interaction location between cell and fibers. It was then followed by series of 2D Raman images covering the full height of cultured cells (8-12 images in the Z-axis). A multivariate statistical analysis based on characteristic cell and fibers Raman absorptions was finally applied. A first result was that fiber concentration in cell environment (here the culture medium volume in petri dish) induces a chemical toxicity over 10 $\mu g.cm^{-2}$, which confirms previous studies on the same asbestos fiber species [34], [35]. The main result was that cell-fiber interaction is truly dependent on morphological characteristics of fibers, with the first demonstration that lung cells adopt a defense strategy to isolate fibers when feasible. Typically, we found fibers vesiculated or embedded in ECM when length did not exceed 5 µm, or just embedded in ECM below 15 µm. Fibers exceeding this length were found crossing cells (with membrane surrounding the part of the fiber entering in cellular space) or incompletely embedded in ECM when on the surface of petri dish. One may consider that fibers partially entering the cellular space or incompletely embedded in the ECM of a single cell will be responsible of major mechanical damages following lung movements during breathes. On the other hand, the vesiculation of small fibers shows that cells can isolate inorganic nanomaterials that cannot be eliminated by biochemical of exocytosis ways. By extension, one may consider that such isolation mechanism also applies to other non-degradable nanomaterials, such as carbon nanotubes, nanoparticles…etc.

This study thus shows that Raman microscopy can be setup for 3D *in vitro* analysis of cells, which is an ideal methodology to investigate experimentally the exposure to organic nanomaterials.

MATERIALS AND METHODS

Cell culture: The cell line used was the type II epithelial lung A549 (ATCC: CCL-185). Cells were grown in a Dulbecco's Modified minimum Essential Medium (DMEM)/F-12 medium supplemented with 10% fetal calf serum, 1 g/L of glucose, glutamine, HEPES and antibiotics. Cells were routinely propagated in a humidified 5 % CO_2 atmosphere at 37°C. Serum-free culture was performed according to Barnes *et al* [36]. The serum-free medium consists of a basal medium supplemented with 25 µg/mL HDL, 5 µg/ml insulin, 5 µg/mL transferrin, 2 ng/mL EGF, 1 mg/mL f-BSA and antibiotics. A concentration of 40.10^3 cells / well has been added into 6-wells plates for 24h and cultivated on Si wafer.

Sample preparation: Two natural asbestos fibers were used for this work; all samples were selected from the collection of the Museum National d'Histoire Naturelle of Paris. The first one is a "crocidolite" from Buchanawald (South Africa), labeled MNHN 134-86. Wavelength-dispersive microprobe analysis (WDS-EMP) gave a composition in the Riebeckite compositional field, according the recent accepted nomenclature schemes for amphiboles [37, 38]. The second is a cummingtonite, labeled MNHN 137.96; EMP data showed this sample to be very rich in Mn, with a composition actually close to the species mangano-cummingtonite ($Mn_2Mg_5Si_8O_{22}OH_2$). Scanning electron microscopy (SEM) showed all samples to consist of very to extremely fibrous crystals, as it is typically the case of "crocidolite" from South Africa, which has an average dimensions < 1.0 µm in width (average 400-500 nm) and typically > 10 µm in length (and up to several tenths of µm). Before the experiments, the fibers were ground in a mechanical milling machine equipped with a micro agata mortar and baked at 250-300°C overnight to avoid chemical and/or biological contaminations due to handling procedures or from the environment. The amphibole powders were suspended in the cell medium and sonicated (Labsonic, 100 W, B. Braun Biotech International) for 5 minutes before each experiment. The concentration of asbestos fibers used all along this work was 5µg / cm².

Colorimetric assay: The cytotoxicity of each type of fiber and concentration was investigated by 3-(4,5-dimethylthiazol-2-yl)-2,5-diphenyl tetrazolium bromide (MTT). It's an alternative method for rapidly and indirectly determining cell viability based on metabolic activity. The test measures the conversion of MTT to insoluble formazan by dehydrogenase enzymes of the intact mitochondria of living cells. A549 cells were seeded at a density of 5.10^3 cells / well into 96-well micro plates for 24h. After treatment with the different concentrations of fibers for 24h, the medium was removed and 200 µl of MTT (Sigma) solution (5 mg/ml in PBS) were added to the plates and incubated for 3 h at 37°C. After a centrifugation at 2000 rpm for 10 minutes, the liquid was removed and the formazan crystals were dissolved in 200 µl of DMSO (Sigma) for 30 minutes. The amount of formazan crystals formed correlates directly with the number of viable cells. Optical density (OD) was measured at 570 nm (reference filter 690 nm) using a UV-spectrofluorometer. Controls were grown in culture medium without treatments; their absorbance values were taken as reference values. Results were analyzed and expressed as percentage of the control (control equals 100%). Mean values of relative viability ± standard deviation (s.d.) were considered for statistical evaluations [39].

3D Raman spectroscopy: Raman spectra were collected using a 532 nm excitation source and a grating of 600 lines / mm at 500nm. The experiments were conducted with a water immersion objective of 63x with a numerical aperture of 1.0. To protect the objective lens and perform long acquisitions spectra, the growing medium cell was removed and replaced before the experiments by PBS with glucose at room temperature. Spectra were acquired using 90*90 (points per line*line per image) sample area for the XY mapping with a scan speed for tracing of 14 s/line and an integration time of 0.2 s. For Z-stack images, the number of layers was determined to obtain a final difference of 800nm between layers. The spectral range from 0 to 4000 cm^{-1} was collected which allows the study of the main fingerprint regions of the inorganic and organic samples. Images have been also performed using the Rayleigh scattering. Before analyzing the data, a pre-processing study has been realized using the software Witec Project 2.06 (Witec, Germany). The baseline was subtracted from each pattern with a 0 order polynomial for a constant offset and the Si substrate peaks were removed from the whole spectrum. Then a Savitsky-Golay filter of 3^{rd} order with eight smoothing point was applied to reduce the electronic noise from the signal. Multivariate analyses were performed further on the modified data. The same procedure was done on all XY mapping. At the end, 3D reconstructed images from all the stack is performed.

Test video: Video tests were done before and after each spectroscopic data collection to prove that the cell is still living at the end the experiment.

Statistics: Multivariate analyses were performed on all data. First, Principal component analysis (PCA) was applied in order to reduce the number of variable of the dataset. Then K-means Hierarchical Cluster Analysis (k-means HCA) test was realized to find out "useful" groups of objects i.e. find out the process of internalization of the fiber into the cells.

SUPPLEMENTARY MATERIALS

Supplementary material n°1 : Video of a living cell **before** the Raman experiment

Supplementary material n°2 : Video of the same living cell **after** the experiment

Supplementary material n°3: Video of the 3D raman showing the fiber (in red) embedded into the cells (in blue)

References

1. Suzuki, Y., S.R. Yuen, and R. Ashley, *Short, thin asbestos fibers contribute to the development of human malignant mesothelioma: pathological evidence.* Int J Hyg Environ Health, 2005. **208**(3): p. 201-10.
2. Addison, J. and E.E. McConnell, *A review of carcinogenicity studies of asbestos and non-asbestos tremolite and other amphiboles.* Regul Toxicol Pharmacol, 2008. **52**(1 Suppl): p. S187-99.
3. Ohar, J., et al., *Changing patterns in asbestos-induced lung disease.* Chest, 2004. **125**(2): p. 744-53.
4. Kamp, D.W., *Asbestos-induced lung diseases: an update.* Transl Res, 2009. **153**(4): p. 143-52.
5. Kamp, D.W., et al., *The role of free radicals in asbestos-induced diseases.* Free Radic Biol Med, 1992. **12**(4): p. 293-315.
6. Kamp, D.W. and S.A. Weitzman, *Asbestosis: clinical spectrum and pathogenic mechanisms.* Proc Soc Exp Biol Med, 1997. **214**(1): p. 12-26.
7. Mossman, B.T. and J.P. Marsh, *Evidence supporting a role for active oxygen species in asbestos-induced toxicity and lung disease.* Environ Health Perspect, 1989. **81**: p. 91-4.
8. Clift, M.J., et al., *The impact of different nanoparticle surface chemistry and size on uptake and toxicity in a murine macrophage cell line.* Toxicol Appl Pharmacol, 2008. **232**(3): p. 418-27.
9. Chan, J., et al., *In vitro toxicity evaluation of 25-nm anatase TiO2 nanoparticles in immortalized keratinocyte cells.* Biol Trace Elem Res, 2011. **144**(1-3): p. 183-96.
10. Carlson, C., et al., *Unique cellular interaction of silver nanoparticles: size-dependent generation of reactive oxygen species.* J Phys Chem B, 2008. **112**(43): p. 13608-19.
11. Chan, J.W., et al., *Micro-Raman spectroscopy detects individual neoplastic and normal hematopoietic cells.* Biophys J, 2006. **90**(2): p. 648-56.
12. Meister, K., et al., *Label-Free Imaging of Metal–Carbonyl Complexes in Live Cells by Raman Microspectroscopy.* Angewandte Chemie International Edition, 2010. **49**(19): p. 3310-3312.
13. Taleb, A., et al., *Raman microscopy for the chemometric analysis of tumor cells.* J Phys Chem B, 2006. **110**(39): p. 19625-31.
14. Short, K.W., et al., *Raman spectroscopy detects biochemical changes due to proliferation in mammalian cell cultures.* Biophys J, 2005. **88**(6): p. 4274-88.
15. Hartmann, K., et al., *A study of Docetaxel-induced effects in MCF-7 cells by means of Raman microspectroscopy.* Anal Bioanal Chem, 2012. **403**(3): p. 745-53.
16. Shetty, G., et al., *Raman spectroscopy: elucidation of biochemical changes in carcinogenesis of oesophagus.* Br J Cancer, 2006. **94**(10): p. 1460-4.
17. Kammer, M., et al., *Spatially resolved determination of the structure and composition of diatom cell walls by Raman and FTIR imaging.* Analytical and Bioanalytical Chemistry, 2010. **398**(1): p. 509-517.
18. Draux, F., et al., *Raman spectral imaging of single cancer cells: probing the impact of sample fixation methods.* Anal Bioanal Chem, 2010. **397**(7): p. 2727-37.
19. Gregas, M.K., et al., *Characterization of nanoprobe uptake in single cells: spatial and temporal tracking via SERS labeling and modulation of surface charge.* Nanomedicine, 2011. **7**(1): p. 115-22.
20. Kneipp, K., et al., *Surface-Enhanced Raman Spectroscopy in Single Living Cells Using Gold Nanoparticles.* Appl. Spectrosc., 2002. **56**(2): p. 150-154.
21. Feng, S., et al., *Gold nanoparticle based surface-enhanced Raman scattering spectroscopy of cancerous and normal nasopharyngeal tissues under near-infrared laser excitation.* Appl Spectrosc, 2009. **63**(10): p. 1089-94.
22. Segawa, H., et al., *Label-free tetra-modal molecular imaging of living cells with CARS, SHG, THG and TSFG (coherent anti-Stokes Raman scattering, second harmonic generation, third*

harmonic generation and third-order sum frequency generation). Opt Express, 2012. **20**(9): p. 9551-7.

23. Wachsmann-Hogiu, S., T. Weeks, and T. Huser, *Chemical analysis in vivo and in vitro by Raman spectroscopy--from single cells to humans.* Curr Opin Biotechnol, 2009. **20**(1): p. 63-73.
24. Draux, F., et al., *Raman imaging of single living cells: probing effects of non-cytotoxic doses of an anti-cancer drug.* Analyst, 2011. **136**(13): p. 2718-25.
25. Bard, D., J. Yarwood, and B. Tylee, *Asbestos fibre identification by Raman microspectroscopy.* Journal of Raman Spectroscopy, 1997. **28**(10): p. 803-809.
26. Petibois, C., et al., *Synchrotron radiation FTIR imaging in minutes: a first step towards real-time cell imaging.* Anal Bioanal Chem, 2010. **397**(6): p. 2123-9.
27. Thebaud-Mony, A., *Justice for asbestos victims and the politics of compensation: the French experience.* Int J Occup Environ Health, 2003. **9**(3): p. 280-6.
28. Williams, T., P. Slade, and J. Raeburn, *Lump sum compensation for asbestos related lung disease.* Thorax, 1998. **53**(7): p. 535.
29. Siskind, F.B., *The cost of compensating asbestos victims under the Occupational Disease Compensation Act of 1983.* Risk Anal, 1987. **7**(1): p. 59-69.
30. Vanotto, A., *[Asbestos victims still in search of justice: the battle of AIEA (Italian Association of the Exposed to Asbestos)].* Epidemiol Prev, 2010. **34**(1-2): p. 15-6.
31. Park, J., et al., *Confocal Raman microspectroscopic study of folate receptor-targeted delivery of 6-mercaptopurine-embedded gold nanoparticles in a single cell.* J Biomed Mater Res A, 2012. **100**(5): p. 1221-8.
32. Bogliolo, L., et al., *Raman microspectroscopy as a non-invasive tool to assess the vitrification-induced changes of ovine oocyte zona pellucida.* Cryobiology, 2012. **64**(3): p. 267-72.
33. Pudlas, M., et al., *Raman spectroscopy: a noninvasive analysis tool for the discrimination of human skin cells.* Tissue Eng Part C Methods, 2011. **17**(10): p. 1027-40.
34. Giantomassi, F., et al., *Biological effects and comparative cytotoxicity of thermal transformed asbestos-containing materials in a human alveolar epithelial cell line.* Toxicol In Vitro, 2010. **24**(6): p. 1521-31.
35. Pugnaloni, A., et al., *Effects of asbestiform antigorite on human alveolar epithelial A549 cells: a morphological and immunohistochemical study.* Acta Histochem, 2010. **112**(2): p. 133-46.
36. Loo, D.T., et al., *Extended culture of mouse embryo cells without senescence: inhibition by serum.* Science, 1987. **236**(4798): p. 200-2.
37. Leake, B.E., et al., *Nomenclature of amphiboles: additions and revisions to the International Mineralogical Association's amphibole nomenclature.* Mineralogical Magazine, 2004. **68**(1): p. 209-215.
38. Hawthorne, F.C. and R. Oberti, *Classification of the Amphiboles.* Reviews in Mineralogy and Geochemistry, 2007. **67**(1): p. 55-88.
39. Mosmann, T., *Rapid colorimetric assay for cellular growth and survival: application to proliferation and cytotoxicity assays.* J Immunol Methods, 1983. **65**(1-2): p. 55-63.

Figures:

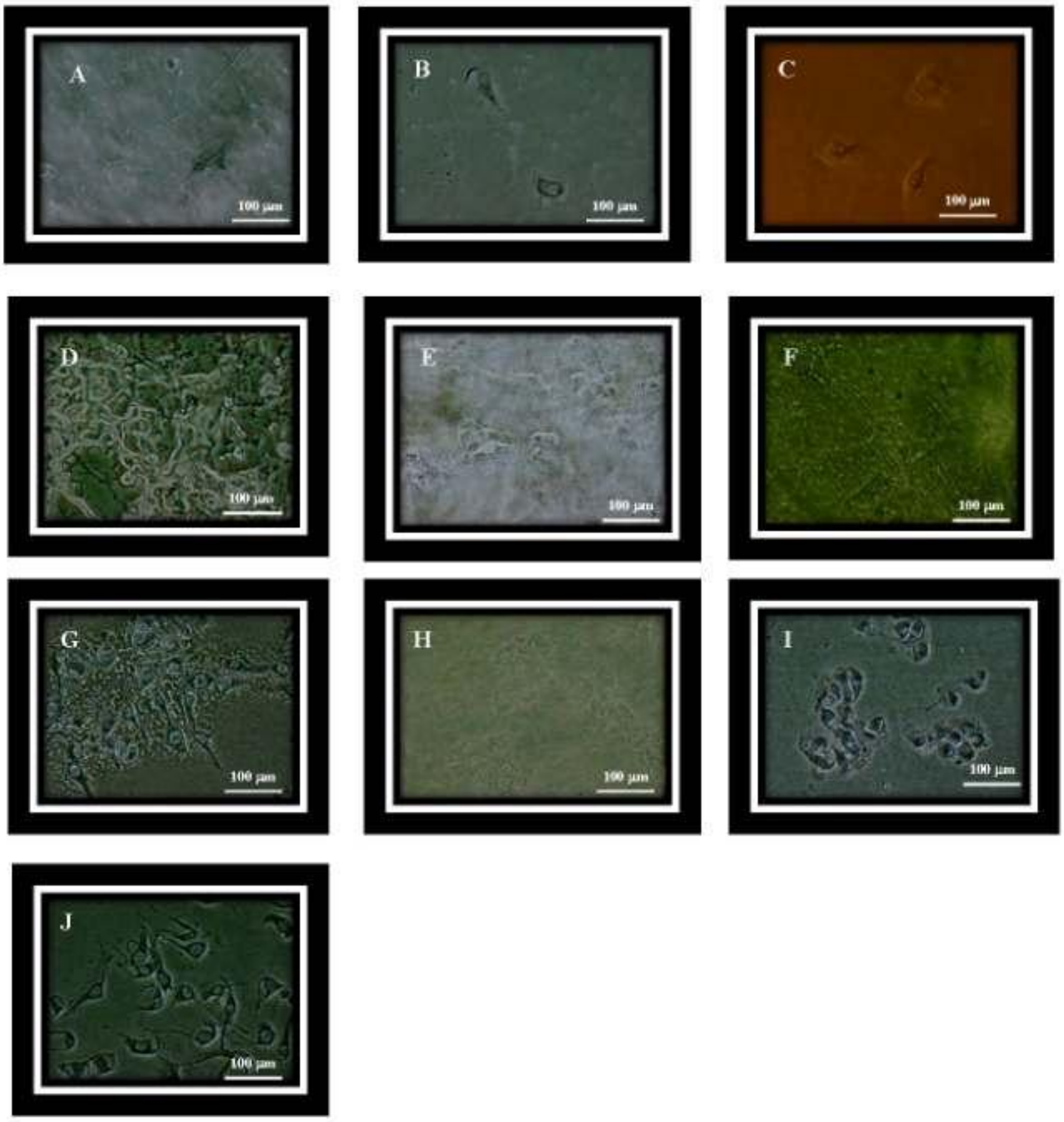

Figure 1: Optical images of two days culture cell on different substrates. **A**: AgCl – 9 cells/cm^2; **B**: CaF$_2$ – 24 cells/cm^2; **C**: GLS – 6 cells/cm^2; **D**: Si$_3$N$_4$ – 164 cells/cm^2; **E**: Diamond – 5 cells/cm^2; **F**: AgBr– 5 cells/cm^2; **G**: SrF$_2$ – 44 cells/cm^2; **H**: ZnS-F – 8 cells/cm^2; **I**: ZnS-C – 110 cells/cm^2 ; **J**: LaF$_3$ – 155 cells/cm^2.

7. DISCUSSION AND CONCLUSIONS

In this study we addressed the cellular response to asbestos fibers. To this end, we developed new spectroscopic methodologies to access both organic (cells) and inorganic (fibers) information at the single cell level. A first step has been the test of suitable IR-transparent substrates for in vitro analyses of single cells by FTIR imaging. The goal was to ensure a safe, i.e. non-toxic, cell culture to perform spectroscopic analyses on living or cryofixed cells. Further, the toxicity of amphiboles could be evaluated by performing biological tests with different types of fibers after culture on the selected IR-transparent substrates. Although not fully developed in this PhD work for analyzing the cell-fiber interactions, *in vitro* IR images of single cells could be also obtained by proposing a new utilization of an ATR device on which cells could be grown. These studies allowed determining that asbestos fibers toxicity was not equal between fiber species, but all shown gradual effects with concentration in culture medium. To further discriminate between chemical and morphological parameters of asbestos fibers toxicity on lung cells, a new Raman microscopy method was proposed on living cells for 3D analysis with respect to fiber aspect ratio. It could be demonstrated that fiber length is a key-parameters of toxicity.

7.1. IMPROVED EXPERIMENTAL CONDITIONS

FTIR imaging is a novel spectroscopic technique able to provide cell imaging, *in vivo* and in real-time. However, one key-issue is developing methodologies for cell culture on IR-transparent substrates fitting cell biology requirements. Indeed, the choice of a substrate suitable for the spectroscopic measurement is a critical point to address before proceeding to the development of dedicated methodologies for cell imaging. Preliminary studies performed in our laboratory permits to develop FTIR imaging coupled with bi-dimensional focal-plane-array (FPA) of detectors using synchrotron radiation in order to obtain 2D IR images of a single cell with a good SNR [81, 86]. To enhance this SNR and obtain quality of cell culture and good IR spectral image, new experiments have been performed testing several substrates with different physical and biological properties. As discussed and illustrated in the article 1, Si, Ge and Si_3N_4 substrates turned out to be the best choices. Based on this finding the results obtained in previous works where CaF_2 or ZnSe substrates were employed [87, 88] could be reviewed and discussed in term of a poor biocompatibility between cells and these substrates.

Despite the use of synchrotron radiation coupled with FPA detectors, the acquired SNR were low because of the cryofixed cells used containing very low amount of organic materials. The consequence was the impossibility to apply the study to spectra located in the cytosol and membrane regions.

The different parameters defined as suitable for this study and the number of substrates makes difficult the choice of a multivariate process to describe the response. Moreover, the necessity to plot the results limited the choice of the model. Thus, the PCR, combination between PCA and PLS regression, leads to the results with high accuracy of the model.

Therefore, the study shows that there is a correlation between the type of substrate, the cell culture quality and the quality of the obtained spectra thus making the correct choice of substrate mandatory for IR imaging of live cell. This point is particularly relevant for live cell analyses, where cell culture conditions must remain unaffected by substrate properties.

7.2. FTIR SPECTROSCOPY AND IMPLICATIONS

FTIR imaging of individual cells is still limited by the low signal-to-noise ratio obtained from analysis of such weakly absorbing organic matter when using a Globar IR source. In this study, we used FTIR imaging with a synchrotron radiation source and a focal plane array detector to determine changes in the cellular contents of cryofixed cells after culture for 48 h on Si_3N_4 substrate. Several spectral differences were observed for cells deprived of glucose compared with control cells: a lower amide I-to amide II ratio ($P<0.01$), a different secondary structure profile of proteins (obtained from amide I spectral region curve fitting), with a significant increase in non-ordered structure components ($P<0.01$); and a higher $\nu(C{=}CH)/\nu_{as}(CH_3)$ absorption ratio ($P<0.01$), suggesting increased unsaturation of fatty acyl chains.

Our study has shown that SR-FTIR imaging is now sufficiently efficient to enable analysis of the low organic matter content of small biological samples, namely individual cells, on the basis of their main molecular structures. A low energy storage ring with stable current level was used for long scanning periods to obtain a high signal-to-noise ratio in FTIR spectral images of cells, thus enabling use of sophisticated spectral data treatment. Importantly, curve fitting of the amide I spectral region could be performed for analysis of the secondary structure of proteins. Spectral regions of fatty acyl chains and the saccharide content of cells could be also investigated, thus providing a global overview of cell molecular changes between two physiological conditions. Therefore, this study demonstrated that SR-FTIR imaging is a suitable analytical technique for investigation of the molecules in cells and their changes.

On the basis of this knowlegde, we decided to investigate the effect of the interaction between asbestos fibers and lung cell by implementing the methodology explains above. The methodology has been tested on individual cells cultured directly on IR-transparent windows for transmission IR measurements after cryofixation.

Because of technical problems, the SR IR coupled with FPA detector could not be used to study the interaction between asbestos fibers and epithelial single cells. To counteract this issue, we developed the method using Globar source as described in article 2. Despite all the conditions used to enhance the IR signal of a single *ex vivo* cell – use of Si wafer and a large number of scan to obtain the highest SNR – the obtained intensity was very low. Therefore, we performed a large number of experiments (n=30) for each condition and instead of using single spectra, we used an average of spectra in the nucleus region. Consequently, only univariate analyses as ANOVA could be performed for the statistical consideration. The results obtained using FTIR imaging coupled to a synchrotron radiation source and FPA detectors in order to determine changes in cellular contents of cryofixed cells is presented in article 3. The aim was to show the ability of SR IR imaging to solve spectral changes on individual cells as a function of different fiber concentrations.

The interpretation of the IR result reveals that the amide II/ amide I absorptions ratio from spectra corresponding to the nucleus location are different as a function of the fibers concentration. Amide absorption changes are associated with a variation of protein content and conformational change of protein and nucleic acids (DNA and RNA) in cells submitted to stress [89, 90]. These changes have the same decreasing pattern for each type of fibers. Thus, the ratio amide I / amide II can be considered as a marker of cellular stress induced by the asbestos fibers.

Similar results were found for amide I / lipids absorptions ratio. In this case, changes were increasing with the concentration. An increase of protein to lipids content ratio explains an enhancement of cellular proliferation, result already provided by cytotoxicity assays [91].

Since the same results were observed for gradually increasing amounts of asbestos fibers up to 10µg/cm², and to different types of fibers with different chemistry, IR spectroscopy has shown its ability to discriminate the effects of different concentrations of fibers. Moreover, these ratios expose biochemical variations of the cells, confirming the ability of IR spectroscopy to access to toxicological information. These promising results show that IR spectroscopy can be an alternative technique to determine of subtle changes in cells exposed to inorganic species and evaluate the toxicity of the fibers at similar concentrations. The use of synchrotron radiation will allow to enhance the results and find more specific markers of toxicity of the asbestos fibers with epithelial cells.

An Attenuated Total Reflection (ATR)-based device designed for an IR microscope coupled to a FPA detector and optimized for in-vivo cell imaging is in development in our laboratory. This device is designed to allow the *in vitro* imaging of living cells and by using existing brilliant synchrotron radiation sources this ATR device may collect images at the surface of the Ge crystal at a sub-cellular spatial resolution with a penetration depth of the evanescent wave around 500 nm within the sample in few seconds. A brief summary of the cellular components that can be detected with such optical device is also presented in annex 1. Preliminary studies of cell imaging using the manually removable Ge-crystal shows that the *in vitro* imaging of living cells is possible. Unfortunately, by lack of time, the development of this original technique to the study of the interaction of fibers with human cells couldn't be performed.

7.3. IN VITRO BEHAVIOR ASSESSMENT

To try accessing the *in vitro* information during the interaction of fibers with living cell, we developed a 3D Raman/optical imaging methodology to characterize both morphological and chemical parameters of the experiments. Despite problems in adjustment of the laser power and scan speed, we were able to collect images at a sub cellular level. Thus, we determined that the toxicity of asbestos fibers is strongly dependent on the fiber length, allowing to characterize a possible mechanism of defense of the cells.

As detailed in section 3.2.3, the confocal system allows a hyperspectral imaging i.e. a sample is scanned point-by-point and line-by-line, and at every pixel a complete Raman spectrum is taken. Then, the multispectral files are analyzed to display the distribution of specific sample properties. The specificity of our Raman microscope system is that only the core of the fiber guides the light and acts as a pinhole for the confocal microscopy. The use of a pinhole permits to the confocal Raman spectroscopy to suppress vertical and horizontal out-of-focus light and ensures that only light originating from the focal plane of the image can reach the detector. By passing through the sample, the resulting signal is a combination between the confocal point signal and the signal that goes through the sample and return to the detector. That's why even if we focalized on a fiber inside the cell, the obtained spectrum contains lipids signal. Thus, the size of the pinhole is critical since the confocal volume illuminated is correlated to the size of the laser light and the use of the core of the optic fiber as pinhole allows a range of pinhole sizes from 100 µm to 25 µm of diameter. This increases the final resolution of the confocal system leading to have fine stack of images. Unfortunately, the high sensitivity of the device due to the reduction of the spot size leads to the rapid degradation of the sample.

Experiments done with fibers in interaction with living cells permitted to characterize some tendencies: 1- most fibers are located under the cells; 2- only small sized fibers (< 5µm in length) are internalized into the cell and 3-longer fibers (5 to 15 µm) are observed in the extra cellular matrix or cross the cell. Multivariate analysis of the data showed that the internalization was made by vesicles via endocytosis mechanism. When the fiber length is > 15 µm, the cell is unable to envelop it illustrating the limitation of the mechanism of defense of the cells. Finally, the exceptional long chronicity for human pathologies related to asbestos fibers as mesothelioma and asbestosis can be linked to the fiber longer than 15 µm whom the toxic effect can't be constrained. This observation suggests that chemical toxicity is certainly low; making those morphological parameters more relevant in the pathology. Since the result has been observed for different types of asbestos chemistry, we can conclude that the toxicity of the fiber is dependent on the length. Lung cells can thus develop defense strategies for handling the biopersistence of inorganic species, which may thus have major impact for bio-safety issues related to nanomaterials.

As a final comment, it is clear that the spectroscopic techniques as IR and Raman may contribute significantly to the analysis of cellular toxicity of asbestos fibers. This work reveals that toxicity of the asbestos fibers is length dependent. Thus, asbestos fibers are not intrinsically toxic but become toxic when inhaled into the lung only when the length is > 15 micron. At this stage of the study, the role of the chemical composition of the fiber is not considered, and requires further investigations to allow a complete comprehension of the process leading to disease as mesothelioma and asbestosis.

Despite the validity of spectroscopic techniques to analyze the toxicity of asbestos fiber in interaction with epithelial lung cells, a lot of work remains to be done. The optimization of the cells responses and the systematic application of the dedicated methodology performed here with synchrotron radiation need to be improved. With the developed methods exposed above, the systematic use of synchrotron radiation with IR spectroscopy and the progress in signal processing for Raman spectroscopy will provide efficient tools to investigate the toxicity of inorganic materials as asbestos fibers in interaction with living cells.

Moreover, experiments using ATR - FTIR device will permit to explore the in vitro interaction between asbestos fiber and cells at a nanometric spectral resolution. It will permit to study the interaction between the extra cellular matrix of the cells and the fibers with a size between 5 and 15µm. We will be able to examine how the interaction is realized at the extra cellular matrix level. It could also be interesting to couple these information with those provided by techniques such as X-ray fluorescence. Indeed, this latter method could provide access to the chemical components related with the pathological effect of the fibers.

REFERENCES

1. VIRTA, R.L., U.S. GEOLOGICAL SURVEY MINERALS YEARBOOK 2001: P. 7.

2. GOLDSMITH, D.F., T.L. GUIDOTTI, AND D.R. JOHNSTON, *DOES OCCUPATIONAL EXPOSURE TO SILICA CAUSE LUNG CANCER?* AM J IND MED, 1982. 3(4): P. 423-40.

3. HOLLAND, L.M., *CRYSTALLINE SILICA AND LUNG CANCER: A REVIEW OF RECENT EXPERIMENTAL EVIDENCE.* REGUL TOXICOL PHARMACOL, 1990. 12(3 PT 1): P. 224-37.

4. DONALDSON, K. AND P.J. BORM, *THE QUARTZ HAZARD: A VARIABLE ENTITY.* ANN OCCUP HYG, 1998. 42(5): P. 287-94.

5. LEE, R.J. AND D.R. VAN ORDEN, *AIRBORNE ASBESTOS IN BUILDINGS.* REGUL TOXICOL PHARMACOL, 2008. 50(2): P. 218-25.

6. LI, H., ET AL., *CURCUMIN PROTECTS AGAINST CYTOTOXIC AND INFLAMMATORY EFFECTS OF QUARTZ PARTICLES BUT CAUSES OXIDATIVE DNA DAMAGE IN A RAT LUNG EPITHELIAL CELL LINE.* TOXICOL APPL PHARMACOL, 2008. 227(1): P. 115-24.

7. LI, H., ET AL., *INHIBITION OF THE MITOCHONDRIAL RESPIRATORY CHAIN FUNCTION ABROGATES QUARTZ INDUCED DNA DAMAGE IN LUNG EPITHELIAL CELLS.* MUTAT RES, 2007. 617(1-2): P. 46-57.

8. BECKER, A., ET AL., *INDUCTION OF CYP1A1 IN RAT LUNG CELLS FOLLOWING IN VIVO AND IN VITRO EXPOSURE TO QUARTZ.* ARCH TOXICOL, 2006. 80(5): P. 258-68.

9. ALBRECHT, C., ET AL., *THE CRUCIAL ROLE OF PARTICLE SURFACE REACTIVITY IN RESPIRABLE QUARTZ-INDUCED REACTIVE OXYGEN/NITROGEN SPECIES FORMATION AND APE/REF-1 INDUCTION IN RAT LUNG.* RESPIR RES, 2005. 6: P. 129.

10. NYGREN, J., ET AL., *DNA DAMAGE IN BRONCHIAL EPITHELIAL AND MESOTHELIAL CELLS WITH AND WITHOUT ASSOCIATED CROCIDOLITE ASBESTOS FIBERS.* ENVIRON MOL MUTAGEN, 2004. 44(5): P. 477-82.

11. HAYES, A.A., ET AL., *ASBESTOS-INDUCED RELEASE OF A HUMAN ALVEOLAR MACROPHAGE-DERIVED NEUTROPHIL CHEMOTACTIC FACTOR.* EXP LUNG RES, 1990. 16(2): P. 121-30.

12. KAMP, D.W., *ASBESTOS-INDUCED LUNG DISEASES: AN UPDATE.* TRANSL RES, 2009. 153(4): P. 143-52.

13. MACCORKLE, R.A., ET AL., *INTRACELLULAR PROTEIN BINDING TO ASBESTOS INDUCES ANEUPLOIDY IN HUMAN LUNG FIBROBLASTS.* CELL MOTIL CYTOSKELETON, 2006. 63(10): P. 646-57.

14. ROBLEDO, R. AND B. MOSSMAN, *CELLULAR AND MOLECULAR MECHANISMS OF ASBESTOS-INDUCED FIBROSIS.* J CELL PHYSIOL, 1999. 180(2): P. 158-66.

15. QUINLAN, T.R., ET AL., *MECHANISMS OF ASBESTOS-INDUCED NITRIC OXIDE PRODUCTION BY RAT ALVEOLAR MACROPHAGES IN INHALATION AND IN VITRO MODELS.* FREE RADIC BIOL MED, 1998. 24(5): P. 778-88.

16. Kamp, D.W., et al., *The role of free radicals in asbestos-induced diseases.* Free Radic Biol Med, 1992. 12(4): p. 293-315.

17. Hodgson A.A. and W. C.A., *The Physics and Chemistry of Asbestos Minerals.* Oxford Conference on Asbestos Minerals, 1967: p. p. 2-10.

18. Janik H. and Wrona M., *Asbestos.* Encyclopedia of Analytical Science, 2005(1): p. 141-148.

19. Settle F.A., *Handbook of Instrumental Techniques for Analytical Chemistry.* 1997: p. 995.

20. Bernade M.A., *Asbestos: The Hazardous Fiber.* 1990: p. 4, 30-38, 41, 80.

21. Division of Occupational Safety & health (DOSH) October, 2009.

22. Krombach, F., et al., *Cell size of alveolar macrophages: an interspecies comparison.* Environ Health Perspect, 1997. 105 Suppl 5: p. 1261-3.

23. *https://diamondenv.wordpress.com/tag/nanoparticles-2/).*

24. Raju, B. and W.N. Rom, *Silica, Some Silicates, Coal Dust and Para-aramid Fibrils. IARC Monographs on the Evaluation of Carcinogenic Risks to Humans, Vol. 68.* Cancer Causes and Control, 1998. 9(3): p. 351-353.

25. Gibbs, G.W. and G. Berry, *Mesothelioma and asbestos.* Regul Toxicol Pharmacol, 2008. 52(1 Suppl): p. S223-31.

26. Bernstein, D.M. and J.A. Hoskins, *The health effects of chrysotile: current perspective based upon recent data.* Regul Toxicol Pharmacol, 2006. 45(3): p. 252-64.

27. Aust, A.E., et al., *Particle characteristics responsible for effects on human lung epithelial cells.* Res Rep Health Eff Inst, 2002(110): p. 1-65; discussion 67-76.

28. Yao, S., G. DellaVentura, and C. Petibois, *Analytical characterization of cell-asbestos fiber interactions in lung pathogenesis.* Anal Bioanal Chem, 2010. 397(6): p. 2079-89.

29. Knaapen, A.M., et al., *Inhaled particles and lung cancer. Part A: Mechanisms.* Int J Cancer, 2004. 109(6): p. 799-809.

30. Perkins, R.C., et al., *Human alveolar macrophage cytokine release in response to in vitro and in vivo asbestos exposure.* Exp Lung Res, 1993. 19(1): p. 55-65.

31. Manning, C.B., V. Vallyathan, and B.T. Mossman, *Diseases caused by asbestos: mechanisms of injury and disease development.* Int Immunopharmacol, 2002. 2(2-3): p. 191-200.

32. Kasper, M. and G. Haroske, *Alterations in the alveolar epithelium after injury leading to pulmonary fibrosis.* Histol Histopathol, 1996. 11(2): p. 463-83.

33. Mossman, B.T., et al., *Cell signaling pathways elicited by asbestos.* Environ Health Perspect, 1997. 105 Suppl 5: p. 1121-5.

34. Barrett, J.C., *Cellular and molecular mechanisms of asbestos carcinogenicity: implications for biopersistence.* Environ Health Perspect, 1994. 102 Suppl 5: p. 19-23.

35. Liu, Z. and J. Klominek, *Chemotaxis and chemokinesis of malignant mesothelioma cells to multiple growth factors.* Anticancer Res, 2004. 24(3a): p. 1625-30.

36. Scott, R.P.W., *Essential Information for the Analytical Chemist.*

37. Petibois, C. and B. Desbat, *Clinical application of FTIR imaging: new reasons for hope.* Trends Biotechnol, 2010. 28(10): p. 495-500.

38. Smith, B.C., *Fourier Transform IR Spectroscopy.* 1996.

39. Petibois, C. and G. Deleris, *Chemical mapping of tumor progression by FT-IR imaging: towards molecular histopathology.* Trends Biotechnol, 2006. 24(10): p. 455-62.

40. Petibois, C. and M. Cestelli Guidi, *Bioimaging of cells and tissues using accelerator-based sources.* Analytical and Bioanalytical Chemistry, 2008. 391(5): p. 1599-1608.

41. Lasch, P. and D. Naumann, *Spatial resolution in infrared microspectroscopic imaging of tissues.* Biochim Biophys Acta, 2006. 1758(7): p. 814-29.

42. Nishikida K., *Spatial resolution in infrared microscopy and imaging.* thermo electron corporation, 2005. Application Note 50717

43. Mariangela, C.G., et al., *Experimental ATR device for real-time FTIR imaging of living cells using brilliant synchrotron radiation sources.* Biotechnol Adv, 2011.

44. Petibois, C., et al., *Facing the challenge of biosample imaging by FTIR with a synchrotron radiation source.* J Synchrotron Radiat, 2010. 17(1): p. 1-11.

45. Marcelli, A., et al., *Biological applications of synchrotron radiation infrared spectromicroscopy.* Biotechnol Adv, 2012.

46. Erukhimovitch, V., et al., *FTIR microscopy as a method for identification of bacterial and fungal infections.* Journal of Pharmaceutical and Biomedical Analysis, 2005. 37(5): p. 1105-1108.

47. Drogat, B., et al., *Acute L-glutamine deprivation compromises VEGF-a upregulation in A549/8 human carcinoma cells.* J Cell Physiol, 2007. 212(2): p. 463-72.

48. Goormaghtigh, E., V. Raussens, and J.M. Ruysschaert, *Attenuated total reflection infrared spectroscopy of proteins and lipids in biological membranes.* Biochim Biophys Acta, 1999. 1422(2): p. 105-85.

49. Serulle, Y., M. Sugimori, and R.R. Llinas, *Imaging synaptosomal calcium concentration microdomains and vesicle fusion by using total internal reflection fluorescent microscopy.* Proc Natl Acad Sci U S A, 2007. 104(5): p. 1697-702.

50. Borglin, S.E., E. Wozei, and H.-Y.N. Holman, *Rapid Water Sample Screening for Estrogenic Activity Using Live Yeast Cells*, in *World Environmental and Water Resources Congress 2007*. p. 1-8.

51. Meade, A., et al., *Growth substrate induced functional changes elucidated by FTIR and Raman spectroscopy in in–vitro cultured human keratinocytes.* Analytical and Bioanalytical Chemistry, 2007. 387(5): p. 1717-1728.

52. Hodgson A.A., *Scientific Advances in Asbestos, 1967 to 1985.* Anjalena Publication, 1986: p. 10, 14, 17, 23, 42, 53, 76, 78, 85, 95-99, 107-117.

53. Marconi, A., *Application of infrared spectroscopy in asbestos mineral analysis.* Ann Ist Super Sanita, 1983. 19(4): p. 629-37.

54. Hahn, D.W., *Raman Scattering Theory.* february 2007.

55. Puppels, G.J., et al., *Laser irradiation and Raman spectroscopy of single living cells and chromosomes: sample degradation occurs with 514.5 nm but not with 660 nm laser light.* Exp Cell Res, 1991. 195(2): p. 361-7.

56. Siebert F. and Hildebrant P., *Vibrational Spectroscopy in Life Science.* Wiley-VCH, 2008.

57. Siesler S., *Infrared and Raman Spectroscopic Imaging* Wiley, 2009.

58. Hendra, P., *Fourier Transform Raman Spectroscopy, .* Spectrochim. Acta, Part A, 1995. 51A(12): p. 1975-2210.

59. Stepakova, L.V., et al., *Vibrational spectroscopic and force field studies of copper(II) chloride and bromide compounds, and crystal structure of KCuBr3.* Journal of Raman Spectroscopy, 2008. 39(1): p. 16-31.

60. Rinaudo, C., E. Belluso, and D. Gastaldi, *Assessment of the use of Raman spectroscopy for the determination of amphibole asbestos.* Mineralogical Magazine, 2004. 68(3): p. 455-465.

61. Bard, D., J. Yarwood, and B. Tylee, *Asbestos fibre identification by Raman microspectroscopy.* Journal of Raman Spectroscopy, 1997. 28(10): p. 803-809.

62. Chan, J.W., et al., *Micro-Raman spectroscopy detects individual neoplastic and normal hematopoietic cells.* Biophys J, 2006. 90(2): p. 648-56.

63. Chan, J., et al., *Raman spectroscopy and microscopy of individual cells and cellular components.* Laser & Photonics Reviews, 2008. 2(5): p. 325-349.

64. Puppels, G.J., et al., *Studying single living cells and chromosomes by confocal Raman microspectroscopy.* Nature, 1990. 347(6290): p. 301-3.

65. Wachsmann-Hogiu, S., T. Weeks, and T. Huser, *Chemical analysis in vivo and in vitro by Raman spectroscopy--from single cells to humans.* Curr Opin Biotechnol, 2009. 20(1): p. 63-73.

66. Taleb, A., et al., *Raman microscopy for the chemometric analysis of tumor cells.* J Phys Chem B, 2006. 110(39): p. 19625-31.

67. Short, K.W., et al., *Raman Spectroscopy Detects Biochemical Changes Due to Proliferation in Mammalian Cell Cultures.* Biophysical journal, 2005. 88(6): p. 4274-4288.

68. Shetty, G., et al., *Raman spectroscopy: elucidation of biochemical changes in carcinogenesis of oesophagus.* Br J Cancer, 2006. 94(10): p. 1460-4.

69. Kammer, M., et al., *Spatially resolved determination of the structure and composition of diatom cell walls by Raman and FTIR imaging.* Anal Bioanal Chem, 2010. 398(1): p. 509-17.

70. Draux, F., et al., *Raman spectral imaging of single cancer cells: probing the impact of sample fixation methods.* Anal Bioanal Chem, 2010. 397(7): p. 2727-37.

71. Gregas, M.K., et al., *Characterization of nanoprobe uptake in single cells: spatial and temporal tracking via SERS labeling and modulation of surface charge.* Nanomedicine, 2011. 7(1): p. 115-22.

72. Kneipp, K., et al., *Surface-Enhanced Raman Spectroscopy in Single Living Cells Using Gold Nanoparticles.* Appl. Spectrosc., 2002. 56(2): p. 150-154.

73. Feng, S., et al., *Gold nanoparticle based surface-enhanced Raman scattering spectroscopy of cancerous and normal nasopharyngeal tissues under near-infrared laser excitation.* Appl Spectrosc, 2009. 63(10): p. 1089-94.

74. Segawa, H., et al., *Label-free tetra-modal molecular imaging of living cells with CARS, SHG, THG and TSFG (coherent anti-Stokes Raman scattering, second harmonic generation, third harmonic generation and third-order sum frequency generation).* Opt Express, 2012. 20(9): p. 9551-7.

75. Draux, F., et al., *Raman imaging of single living cells: probing effects of non-cytotoxic doses of an anti-cancer drug.* Analyst, 2011. 136(13): p. 2718-25.

76. Loo, D.T., et al., *Extended culture of mouse embryo cells without senescence: inhibition by serum.* Science, 1987. 236(4798): p. 200-2.

77. Lin, W., et al., *In vitro toxicity of silica nanoparticles in human lung cancer cells.* Toxicol Appl Pharmacol, 2006. 217(3): p. 252-9.

78. *http://www.addexbio.com/productdetail?pid=23*.

79. **LEAKE, ET AL., *NOMENCLATURE OF AMPHIBOLES: ADDITIONS AND REVISIONS TO THE INTERNATIONAL MINERALOGICAL ASSOCIATION'S AMPHIBOLE NOMENCLATURE*. VOL. 89. 2004, WASHINGTON, DC, ETATS-UNIS: MINERALOGICAL SOCIETY OF AMERICA. 5.**

80. **HAWTHORNE, F.C. AND R. OBERTI, *CLASSIFICATION OF THE AMPHIBOLES.* REVIEWS IN MINERALOGY AND GEOCHEMISTRY, 2007. 67(1): P. 55-88.**

81. **PETIBOIS, C., ET AL., *SYNCHROTRON RADIATION FTIR IMAGING IN MINUTES: A FIRST STEP TOWARDS REAL-TIME CELL IMAGING.* ANAL BIOANAL CHEM, 2010. 397(6): P. 2123-9.**

82. **MOSMANN, T., *RAPID COLORIMETRIC ASSAY FOR CELLULAR GROWTH AND SURVIVAL: APPLICATION TO PROLIFERATION AND CYTOTOXICITY ASSAYS.* J IMMUNOL METHODS, 1983. 65(1-2): P. 55-63.**

83. **PETIBOIS, C., ET AL., *DETERMINATION OF GLUCOSE IN DRIED SERUM SAMPLES BY FOURIER-TRANSFORM INFRARED SPECTROSCOPY.* CLIN CHEM, 1999. 45(9): P. 1530-5.**

84. **CATTELL, R.B., *THE SCREE TEST FOR THE NUMBER OF FACTORS.* MULTIVARIATE BEHAVIORAL RESEARCH, 1966. 1(2): P. 245-276.**

85. **FERRARO, J.R., K. NAKAMOTO, AND C.W. BROWN, *INTRODUCTORY RAMAN SPECTROSCOPY (SECOND EDITION)*, ELSEVIER, EDITOR. 2003.**

86. **PETIBOIS, C., *IMAGING TECHNIQUES WITH SYNCHROTRON RADIATION.* ANAL BIOANAL CHEM, 2010. 397(6): P. 2031-2.**

87. **ORSINI, F., ET AL., *FT-IR MICROSPECTROSCOPY FOR MICROBIOLOGICAL STUDIES.* J MICROBIOL METHODS, 2000. 42(1): P. 17-27.**

88. **CHEUNG, H.Y., ET AL., *MORPHOLOGICAL AND CHEMICAL CHANGES IN THE ATTACHED CELLS OF PSEUDOMONAS AERUGINOSA AS PRIMARY BIOFILMS DEVELOP ON ALUMINIUM AND CAF2 PLATES.* J APPL MICROBIOL, 2007. 102(3): P. 701-10.**

89. **MALINS, D.C., ET AL., *ANTIOXIDANT-INDUCED CHANGES IN OXIDIZED DNA.* PROC NATL ACAD SCI U S A, 2002. 99(9): P. 5937-41.**

90. **MALINS, D.C., N.L. POLISSAR, AND S.J. GUNSELMAN, *INFRARED SPECTRAL MODELS DEMONSTRATE THAT EXPOSURE TO ENVIRONMENTAL CHEMICALS LEADS TO NEW FORMS OF DNA.* PROCEEDINGS OF THE NATIONAL ACADEMY OF SCIENCES, 1997. 94(8): P. 3611-3615.**

91. **ADAMSON, I.Y., *EARLY MESOTHELIAL CELL PROLIFERATION AFTER ASBESTOS EXPOSURE: IN VIVO AND IN VITRO STUDIES.* ENVIRON HEALTH PERSPECT, 1997. 105 SUPPL 5: P. 1205-8.**

ANNEX 1

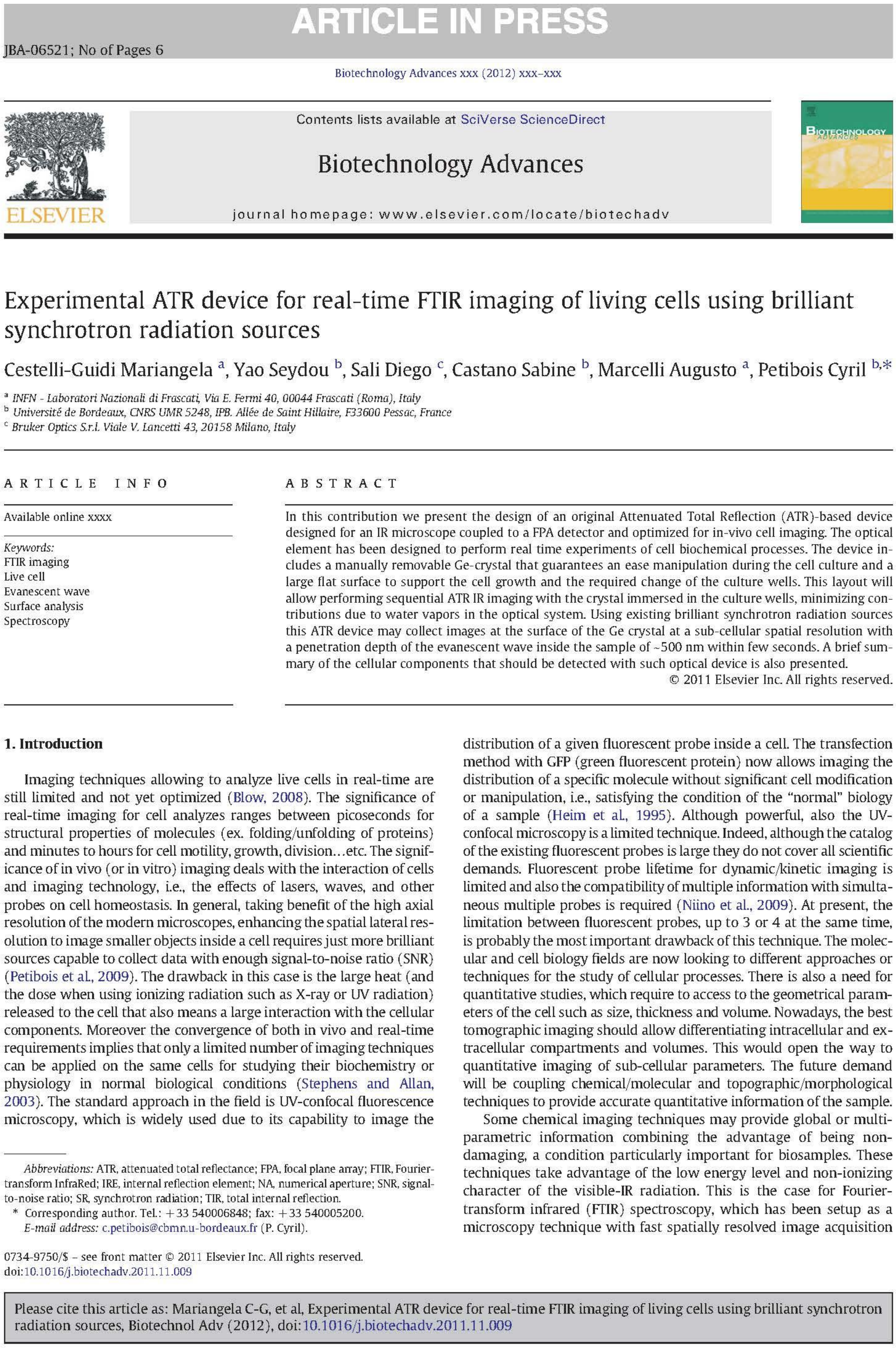

ARTICLE IN PRESS

JBA-06521; No of Pages 6

Biotechnology Advances xxx (2012) xxx–xxx

Contents lists available at SciVerse ScienceDirect

Biotechnology Advances

journal homepage: www.elsevier.com/locate/biotechadv

Experimental ATR device for real-time FTIR imaging of living cells using brilliant synchrotron radiation sources

Cestelli-Guidi Mariangela [a], Yao Seydou [b], Sali Diego [c], Castano Sabine [b], Marcelli Augusto [a], Petibois Cyril [b,*]

[a] INFN - Laboratori Nazionali di Frascati, Via E. Fermi 40, 00044 Frascati (Roma), Italy
[b] Université de Bordeaux, CNRS UMR 5248, IPB. Allée de Saint Hillaire, F33600 Pessac, France
[c] Bruker Optics S.r.l. Viale V. Lancetti 43, 20158 Milano, Italy

ARTICLE INFO

Available online xxxx

Keywords:
FTIR imaging
Live cell
Evanescent wave
Surface analysis
Spectroscopy

ABSTRACT

In this contribution we present the design of an original Attenuated Total Reflection (ATR)-based device designed for an IR microscope coupled to a FPA detector and optimized for in-vivo cell imaging. The optical element has been designed to perform real time experiments of cell biochemical processes. The device includes a manually removable Ge-crystal that guarantees an ease manipulation during the cell culture and a large flat surface to support the cell growth and the required change of the culture wells. This layout will allow performing sequential ATR IR imaging with the crystal immersed in the culture wells, minimizing contributions due to water vapors in the optical system. Using existing brilliant synchrotron radiation sources this ATR device may collect images at the surface of the Ge crystal at a sub-cellular spatial resolution with a penetration depth of the evanescent wave inside the sample of ~500 nm within few seconds. A brief summary of the cellular components that should be detected with such optical device is also presented.

1. Introduction

Imaging techniques allowing to analyze live cells in real-time are still limited and not yet optimized (Blow, 2008). The significance of real-time imaging for cell analyzes ranges between picoseconds for structural properties of molecules (ex. folding/unfolding of proteins) and minutes to hours for cell motility, growth, division…etc. The significance of in vivo (or in vitro) imaging deals with the interaction of cells and imaging technology, i.e., the effects of lasers, waves, and other probes on cell homeostasis. In general, taking benefit of the high axial resolution of the modern microscopes, enhancing the spatial lateral resolution to image smaller objects inside a cell requires just more brilliant sources capable to collect data with enough signal-to-noise ratio (SNR) (Petibois et al., 2009). The drawback in this case is the large heat (and the dose when using ionizing radiation such as X-ray or UV radiation) released to the cell that also means a large interaction with the cellular components. Moreover the convergence of both in vivo and real-time requirements implies that only a limited number of imaging techniques can be applied on the same cells for studying their biochemistry or physiology in normal biological conditions (Stephens and Allan, 2003). The standard approach in the field is UV-confocal fluorescence microscopy, which is widely used due to its capability to image the distribution of a given fluorescent probe inside a cell. The transfection method with GFP (green fluorescent protein) now allows imaging the distribution of a specific molecule without significant cell modification or manipulation, i.e., satisfying the condition of the "normal" biology of a sample (Heim et al., 1995). Although powerful, also the UV-confocal microscopy is a limited technique. Indeed, although the catalog of the existing fluorescent probes is large they do not cover all scientific demands. Fluorescent probe lifetime for dynamic/kinetic imaging is limited and also the compatibility of multiple information with simultaneous multiple probes is required (Niino et al., 2009). At present, the limitation between fluorescent probes, up to 3 or 4 at the same time, is probably the most important drawback of this technique. The molecular and cell biology fields are now looking to different approaches or techniques for the study of cellular processes. There is also a need for quantitative studies, which require to access to the geometrical parameters of the cell such as size, thickness and volume. Nowadays, the best tomographic imaging should allow differentiating intracellular and extracellular compartments and volumes. This would open the way to quantitative imaging of sub-cellular parameters. The future demand will be coupling chemical/molecular and topographic/morphological techniques to provide accurate quantitative information of the sample.

Some chemical imaging techniques may provide global or multiparametric information combining the advantage of being non-damaging, a condition particularly important for biosamples. These techniques take advantage of the low energy level and non-ionizing character of the visible-IR radiation. This is the case for Fourier-transform infrared (FTIR) spectroscopy, which has been setup as a microscopy technique with fast spatially resolved image acquisition

---

Abbreviations: ATR, attenuated total reflectance; FPA, focal plane array; FTIR, Fourier-transform InfraRed; IRE, internal reflection element; NA, numerical aperture; SNR, signal-to-noise ratio; SR, synchrotron radiation; TIR, total internal reflection.

* Corresponding author. Tel.: +33 540006848; fax: +33 540005200.
E-mail address: c.petibois@cbmn.u-bordeaux.fr (P. Cyril).

0734-9750/$ – see front matter © 2011 Elsevier Inc. All rights reserved.
doi:10.1016/j.biotechadv.2011.11.009

Please cite this article as: Mariangela C-G, et al, Experimental ATR device for real-time FTIR imaging of living cells using brilliant synchrotron radiation sources, Biotechnol Adv (2012), doi:10.1016/j.biotechadv.2011.11.009

capabilities using focal plane array (FPA) detectors (Bhargava, 2007; Petibois and Déléris, 2006). Another important feature of the FTIR technique is the absence of contrast agents and molecular probes for characterizing sample contents. This is however compensated by the difficult to extract relevant molecular information from the global spectral signal of cellular organic contents. Nevertheless, the main limitations of FTIR imaging is the diffraction limit condition, i.e., the maximum spatial lateral resolution available that ranges between 3 and 10 μm in the mid-IR spectral range(Petibois et al., 2010b) (Fig. 1, right panel), and the difficulty to handle the strong water absorption signal. Recent attempts to develop live cell imaging by FTIR means conducted to propose microfluidic coupled to an attenuated total reflection (ATR) device (Holman et al., 2009), with the aim to reduce water absorption at cell location by minimizing water thickness. However, cell was almost at the air contact, and this experimental condition can be considered as a stress situation altering the cell response to experimental condition. Therefore, live cell imaging became feasible by FTIR-ATR microscopy, but applications to cell biology studies did not appear promising. Nevertheless, such new utilization of an ATR device has opened the route to high resolution cell imaging with FTIR microscopy (Petibois and Desbat, 2010). Indeed, ATR devices offer the opportunity to collect the evanescent wave propagating at the surface of a high-refractive-index crystal, improving the spatial lateral resolution by increasing the numerical aperture of the optical system and the refractive index (n) of the device. The technique is based on the well-known phenomena of the total internal reflection (TIR). Actually, at the interface between two media with different refraction indexes ($n_1 > n_2$), if the incidence angle θ is greater than the critical angle ($\sin\theta > n_2/n_1$), the light is totally reflected at the interface, a standing wave normal to the reflecting surface is established in the denser (n_1) transparent medium and an evanescent non-propagating field occurs in the rarer (n_2) medium. The electric field amplitude will decay exponentially with the distance from the interface in the medium with the lower refraction index. The reflectivity measured with this technique is a probe of the interaction of the evanescent wave with the sample and the spectrum is characteristic of the sample material. Compared to transmission spectra, the nature of these measurements is controlled also by the incidence angle. The evanescent wave is indeed a special type of electromagnetic radiation that occurs only in the regime of supercritical internal reflection. It propagates parallel to the interface and it is confined to a narrow region outside the sampling surface of the ATR device. Its intensity decreases exponentially with the distance from the sampling surface and the penetration depth of IR light in the sample for ATR measurements is of the order of the wavelength. It ranges between 200 and 500 nm for a germanium ATR crystals and it is independent by the sample thickness. Consequently, this approach appears particularly suitable to measure substances with a strong infrared absorption such as live epithelial cells in an aqueous culture medium (Kuimova et al., 2009). However, ATR devices are not yet optimized to couple with FPA detectors and are not yet developed for live cell imaging studies, i.e., are not optimized to be compatible with a culture medium to maintain cell homeostasis. In this manuscript, we propose a conceptually new ATR layout specifically designed for live cell imaging. This device is based on an optimized and removable ATR germanium crystal, thought for a direct cell growth on its surface. A specific petri dish will be also developed with a customized geometry in order to match the Ge-crystal for an easy surface-surface alignment, and to ensure the normal cell growth and the surface attachment during culture. First image acquisitions show promising results for this new biotechnological development of FTIR imaging. The potential applications of this unique ATR device and what kind of cell contents information can be obtained with such surface imaging technique are also discussed.

2. Materials and methods

2.1. Development of the ATR device

For allowing cell culture directly on the crystal surface, the ATR crystal needs:

1 a large flat surface, typically ~200 μm in diameter;
2 comparable surface properties, e.g., adhesiveness and biocompatibility as glass or plastics that are used for cell cultures, but a high refractive index;
3 be manually removable avoiding the direct contact with fingers.

In Fig. 2 we show the concept of a removable ATR device made by two parts: the Ge crystal itself and the metallic (e.g., aluminum) holder on which it is fixed. The choice of germanium is in line with previous studies that demonstrated its comparable surface properties with glass or a polycarbonate petri dish (Petibois et al., 2010a). Furthermore, Ge has a refractive index ($n = 4$ at 10 μm) much higher than that typical of biosamples (~1.4). IR radiation enters the crystal through a set of mirrors, and in this layout is internally reflected only one time. The crystal holder has the same dimensions of existing ATR devices, but it is now manually positioned on the ATR optical device (currently welded). For ensuring the optical alignment between the Ge-crystal and the mirrors of the ATR optics, the aluminum crystal holder has only one possible matching position with the ATR device,

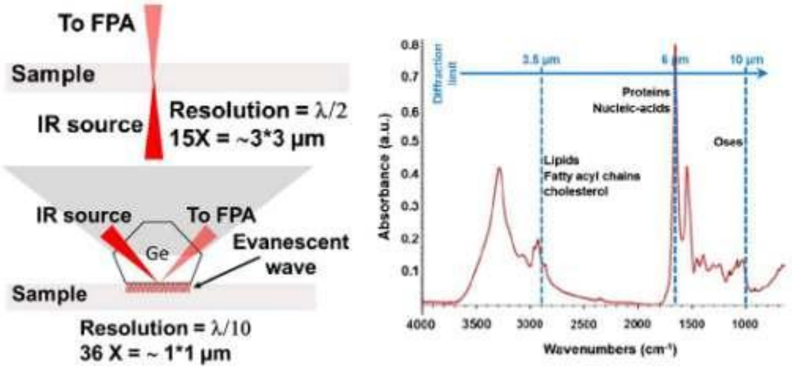

Fig. 1. Lateral spatial resolution limits for two FTIR microscopy setups: transmission (top left) and ATR (bottom left). On the right a typical spectrum in the mid-IR range outlining the different diffraction limit contribution vs. wavelength.

Please cite this article as: Mariangela C-G, et al, Experimental ATR device for real-time FTIR imaging of living cells using brilliant synchrotron radiation sources, Biotechnol Adv (2012), doi:10.1016/j.biotechadv.2011.11.009

Fig. 2. Layouts of the removable ATR crystal device.

which is guaranteed by two mechanical pivots. Lock and stabilization of the Ge-crystal holder with the ATR optics are done magnetically.

2.2. Cell culture on Ge-crystal

The removable device has been properly developed to have the cell culture on the Ge-crystal surface. The crystal has to be inserted in a special petri disk matching the crystal shape and dimensions. We propose to modify a glass-made petri dish (reusable and easily washable) as shown in Fig. 3. The petri dish has edges beveled at 45° with a 200 μm diameter hole on the top for matching the Ge-crystal geometry. In this way, a perfect overlap between the surface of the Ge-crystal and that of the petri dish bottom is obtained, minimizing or avoiding surface topology effects during the cell culture. We proposed also developing a specific support for maintaining the crystal holder in the vertical position during cell incubation. The support is just a Plexiglas made basis matching the crystal holder insertion shape, i.e., a rounded basis with two pivots. The basis has on top a conic body with the height of the crystal holder whose role is to maintain the petri dish while inserted on the Ge-crystal. This support will then ensure the verticality of the Ge-crystal and the cohesion with the petri dish during the incubation process.

2.3. Insulation of ATR optics

The goal to perform live cell imaging and possibly successive image acquisitions for kinetic studies may significantly increase potential applications of the FTIR-ATR (surface) imaging tool. However, in this scenario the water contained in the petri dish, at the typical temperature of 37 °C at which experiments are performed easily evaporates. Although water loss compensation may be easily managed by a surface tension sensor placed at the surface of the culture medium, the main issue is that ATR optical elements will be constantly exposed to water vapor. They can be removed continuously by the N_2 purge of the microscope. However, it is much better to consider a way to insulate the ATR optics from the water vapor that may easily condensate inside the objective. To minimize contribution due to water vapors inside the system we propose to modify the device by placing an IR-transparent and hydrophobic membrane at the level of the Ge-crystal holder insertion in the ATR device. Once ATR optics is isolated, the subtraction of the water spectrum (background) at the surface of the Ge-crystal is easier. Summarizing, the combination of the following three conditions will make such ATR device optimized for routine cell imaging:

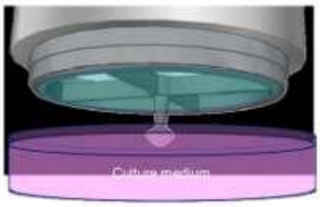

Fig. 4. The hydrophobic membrane protecting the ATR objective for multiple image acquisitions for kinetic studies.

1 a removable Ge-crystal easy to handle and to align on the ATR device;
2 a kit of customized petri dish matching the geometry of the Ge-crystal and of the support maintaining constant all the necessary conditions during cell culture; and
3 an insulated ATR optics minimizing spectral variations induced by water vapor fluctuations vs. time (Fig. 4).

3. Expected results

3.1. Lateral resolution for cell imaging

Lateral resolution is one of the most critical parameters in FTIR micro-spectroscopy and it is determined by a combination of different contributions, notably the diffraction limit and parameters such as the pixel size of the detector and the numerical aperture (NA) of the objective. However, the concept of the lateral resolution has to be associated to a resolution criterion, i.e., the ability to record the separation of two closely spaced objects inside a sample. As an example, in the Rayleigh criterion, two points can be separated when the central maximum of the first Airy disk is placed at a distance greater than the radius of the first minimum of the Airy disk:

$$d = 1.22\lambda/2\mathrm{NA} \quad (1)$$

where λ is the wavelength and NA is the numerical aperture of the objective. NA is defined as:

$$\mathrm{NA} = n\sin(\theta) \quad (2)$$

where n is the refractive index of the imaging medium between the objective and the sample, and θ is half the angular aperture. In the ideal conditions, this criterion is valid only when the two points have the same intensity, a condition that corresponds to a minimum contrast of 26.4% (Levenson et al., 2008). Moreover, as it has been shown recently (Levenson et al., 2006) that spatial resolution is affected by both the optical design (e.g., objectives and apertures) and contrast. This parameter is clearly associated to the SNR of an

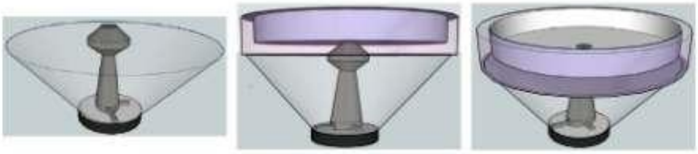

Fig. 3. Drafts showing the petri dish customization to allow the cell growth on the ATR crystal.

Please cite this article as: Mariangela C-G, et al, Experimental ATR device for real-time FTIR imaging of living cells using brilliant synchrotron radiation sources, Biotechnol Adv (2012), doi:10.1016/j.biotechadv.2011.11.009

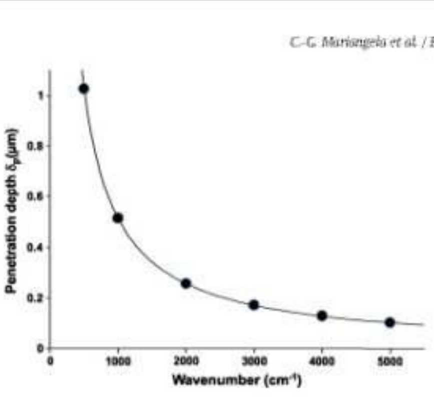

Fig. 5. Typical curve showing the penetration depth of the evanescent wave at different wavelengths.

image. Then to resolve two adjacent points completely, the separation required will depend by the effective contrast existing between the two points and will range from λ up to ~2λ (Chan and Kazarian, 2003). For most infrared microscope objectives the numerical aperture NA ranges between 0.5 and 0.7. Thus the diffraction limited spatial resolution in the IR fingerprint region (4000–1000 cm^{-1}) ranges from ~3 to ~10 µm. However, according to Eq. (1) the spatial resolution can be increased using an optical system with a large numerical aperture, e.g., using a higher magnification objective or, as it has been demonstrated (Colley et al., 2004) using a high-refractive-index material as the reflection element of an ATR device. The use of a high-refractive-index material has the effect to *shortening* all the wavelengths that reach the sample, actually reducing the effects of the diffraction by the same factor of the refractive index value. In an ATR device, the IR light is totally reflected at the interface between the sample and the internal reflection element (IRE). At this interface, the electric field of the IR light penetrates into the sample of the lower refractive index as an evanescent wave, whose electrical field amplitude decays exponentially within the surface of the material. It is important to underline here that the establishment of a standing wave means that there is no flow of energy into the non-absorbing less dense medium. The penetration depth δ_p is defined as the distance at which the electric field falls to e^{-1} of its value at the surface. It is independent by the sample thickness and it is a function of the wavelength λ, of the incident angle θ and of the refractive indexes of the crystal (n_1) and the sample (n_2):

$$\delta_p = \frac{\lambda}{2\pi n_1 \sqrt{\sin^2\theta - \left(\frac{n_2}{n_1}\right)^2}}. \tag{3}$$

Although the ATR technique enables only a coarse depth profile as outlined above the penetration depth can be varied changing experimental parameters such as the angle of incidence and eventually the refractive index of the material of the ATR. For a Ge-crystal ($n_1 = 4$ at 10 µm) and a typical biological sample (n_2~1.4) the penetration depth ranges from ~0.5 µm at 10,000 cm^{-1} to ~0.2 µm at 3000 cm^{-1} (Fig. 5).

ATR spectra are intrinsically affected by light polarization and dispersion effects, resulting in a deviation from the Beer's law, a shift of the absorption bands to lower frequency and a dependence of the absorption intensity from the wavelength. These effects are usually corrected by specifics algorithms. Coupling an ATR device with a FPA detector has the additional advantage to combine the small FPA pixel size with the objective magnification to achieve the highest spatial resolution. Depending on the magnification level used (the examples given below refer to commercially available systems) and the pixel detector size, the resultant pixel resolution on an IR image can be calculated as follows:

1. pixel detector size of 40×40 µm with 15× magnification = 2.66×2.66 µm
2. pixel detector size of 40×40 µm with 36× magnification = 1.11×.1.11 µm (see Fig. 1)
3. pixel detector size of 40×40 µm with 74× magnification = 0.54×0.54 µm.

For a FPA with 64×64 pixels the area of the final IR image will range between 171×171 µm with the 15× objective to 71×71 µm with the 36× and down to 35×35 µm with the 74×. Images with such areas contain one or several cells (Fig. 6). The practical limit will depend by the SNR achieved within a given time acquisition (see below the real-time imaging section). A high SNR can be obtained using intense and brilliant synchrotron radiation (SR) sources (Petibois et al., 2010b). However, as it has been clearly demonstrated (Petibois et al., 2010b), to match a synchrotron radiation source a FPA detector has to be resized by selecting a limited number of pixels of the FPA in order to match the intrinsically small SR source size. Moreover, the latter has an elliptical shape with a strongly inhomogeneous photon density whose intensity may change 1–2 orders of magnitude between the center (maximum) and the edges (minimum) (Petibois et al., 2010b). Summarizing, both pixel resolution and larger numerical apertures may increase the spatial resolution down to the diffraction limit and thanks to the nowadays available brilliance of the SR source the ATR-FPA combination can reach the ultimate resolution necessary for cell investigations.

3.2. Real-time FTIR-ATR imaging of cells

In imaging methods, *time resolution* is usually considered on the side of physical constrains, which deal with the necessary SNR to

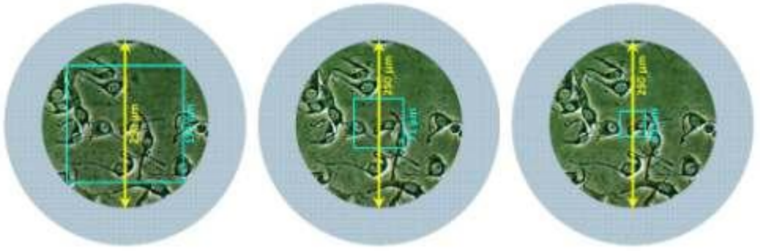

Fig. 6. Simulation of cell image acquisitions at different magnification levels. The three panels show the Ge-crystal surface on which tumor cells have grown during a culture of typically 24 h. From left to right, the different FPA detector coverage areas on the Ge-crystal surface using an objective with 15×, 36×, and 74× magnification levels.

Please cite this article as: Mariangela C-G, et al, Experimental ATR device for real-time FTIR imaging of living cells using brilliant synchrotron radiation sources, Biotechnol Adv (2012), doi:10.1016/j.biotechadv.2011.11.009

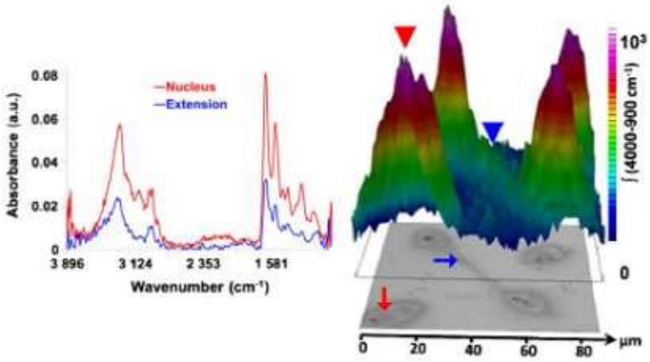

Fig. 7. FTIR image of living cells with corresponding spectra. FTIR images were obtained using 500 coadded scans (8 cm^{-1}, 4000–900 cm^{-1}) and representation is in full spectral absorbance.

obtain interpretable data from an experiment. However, there is another more relevant *time resolution* that an imaging technique has to consider: the cell life timing (Cardone and Sassone-Corsi, 2003). Depending on the expected result of the experiment and the cell parameters to monitor, the *time resolution* of a real-time image acquisition ranges between picoseconds and minutes. Fast resolution is required when dealing with protein folding, molecular interfaces, membrane trafficking of solutes (free ions and cations, etc.) and, in general, almost all biochemical processes such as enzymatic reactions…etc. On the other side, resolution in the range of minutes is required for the imaging of the internal cell organization, e.g., morphology, the extracellular matrix, the cytoskeleton… In general, inside a petri dish, the cell motility prohibits image acquisitions longer than 5 min. Now, considering the minimal time acquisition for a spectral image with sufficient SNR (> 100) to extract spectral data, with one scan (milliseconds range), 10 scans (second range), and 100 scans (minute range), a general evaluation is that it will be possible to analyze biochemical, biological, and morphological processes, respectively.

3.3. FTIR-ATR cell imaging data

The growth of cells on a substrate can be imaged directly from the surface of this latter. Collection of the evanescent wave depends directly by the refractive index of the substrate (in our case $n_{Ge}=4$) and of the sample (~1.4 for biosamples) and by the wavelength of the IR radiation. This internal reflection creates an evanescent wave, which extends beyond the surface of the crystal inside the sample in contact with its surface. However, the evanescent wave decays rapidly from the surface, with about 90% of the signal confined in the first 500 nm from the crystal surface (Fig. 7). In this example, FTIR image of several cells shows clearly that morphological features of cells can be recognized, namely the core of the cells and cytosolic extensions between them. The quality of IR spectra extracted from nucleus or extension locations of cells can be considered as sufficient for further spectral data treatments. However, this approach of live cell imaging will require determining which molecular information from cell is present in extracted spectra, i.e., coming from the ~500 nm below crystal surface. Taking into account that the refractive index of the Ge decreases from 4.04 to 4.00 between 3 and 10 µm wavelengths, the penetration depth of the field associated to the evanescent wave actually is almost constant in the mid-IR range (cf. Fig. 5; the 900–4000 cm^{-1} spectral interval for cell images presented in Fig. 7). In the first 500 nm from the surface where cells grow in the culture media, the first molecular components belong to the extracellular matrix developed for ensuring the structural support and the stability of cells. This is probably a significant part of the absorption of amides observed in spectra (1700–1500 cm^{-1}), which is present both at nucleus and extension locations. This matrix is made of fibrous proteins, e.g., collagens and polysaccharides and has a thickness ranging between 5 and 50 nm, mostly depending by the cell phenotype and the confluence level achieved in the culture. In fact, cells at confluence can further develop the extracellular matrix for 3D organization. The next cellular components accessible are the membrane, ~7 nm thick, the cytoskeleton and intracellular organelles. In addition to these, because the nucleus diameter is ~1–3 µm and its location is usually very close to the membrane and maintained by the cytoskeletal proteins, also the nucleus will be partially analyzed. Also subcellular organelles will be randomly accessible so that, within the limit of ~500 nm, it will be possible to monitor and analyze almost all relevant cellular compartments and compounds by FTIR-ATR imaging.

4. Conclusion

We presented here a novel ATR device based on a germanium crystal optimized for high spatial resolution cell imaging. We described how it may be combined with a FPA detector for single reflection imaging via collection of the evanescent wave at the surface of the crystal. The device has been also designed to allow an easy removal of the crystal from the ATR optics to support the growth of cell directly on the Ge crystal. FTIR-ATR imaging experiments performed at high magnification levels will give in the future new opportunities in live cell imaging. In particular, to investigate cellular components the use of high brilliance-high current synchrotron radiation sources would allow the achievement of sub-micron resolution in real time.

Acknowledgments

Authors acknowledge the "Italian-French University" (Vinci program 2009), the "Ligue Contre le Cancer", the "Association Française contre les Myopathies" and the "Agence Nationale pour la Recherche – ANR" for their financial supports. This research has been partially supported within the EU 7th Framework Programme (FP7/2007-2013) under the grant agreement no. 226716.

References

Bhargava R. Towards a practical Fourier transform infrared chemical imaging protocol for cancer histopathology. Anal Bioanal Chem 2007;389:1155–69.
Blow N. Cell imaging: new ways to see a smaller world. Nature 2008;456:825–8.
Cardone L, Sassone-Corsi P. Timing the cell cycle. Nat Cell Biol 2003;5:859–61.

Please cite this article as: Mariangela C-G, et al, Experimental ATR device for real-time FTIR imaging of living cells using brilliant synchrotron radiation sources, Biotechnol Adv (2012), doi:10.1016/j.biotechadv.2011.11.009

Chan KL, Kazarian SG. New opportunities in micro- and macro-attenuated total reflection infrared spectroscopic imaging: spatial resolution and sampling versatility. Appl Spectrosc 2003;57:381–9.

Colley CS, Kazarian SG, Weinberg PD, Lever MJ. Spectroscopic imaging of arteries and atherosclerotic plaques. Biopolymers 2004;74:328–35.

Heim R, Cubitt AB, Tsien RY. Improved green fluorescence. Nature 1995;373:663–4.

Holman HY, Miles R, Hao Z, Wozei E, Anderson LM, Yang H. Real-time chemical imaging of bacterial activity in biofilms using open-channel microfluidics and synchrotron FTIR spectromicroscopy. Anal Chem 2009;81:8564–70.

Kuimova MK, Chan KL, Kazarian SG. Chemical imaging of live cancer cells in the natural aqueous environment. Appl Spectrosc 2009;63:164–71.

Levenson E, Lerch P, Martin MC. Infrared imaging: synchrotrons vs. arrays, resolution vs. speed. Infrared Phys Technol. 2006;49:45–52.

Levenson E, Lerch P, Martin MC. Spatial resolution limits for synchrotron-based infrared microspectroscopy. Infrared Phys Technol. 2008;51:413–6.

Niino Y, Hotta K, Oka K. Simultaneous live cell imaging using dual FRET sensors with a single excitation light. PLoS One 2009;4:e6036.

Petibois C, Déléris G. Chemical mapping of tumor progression by FT-IR imaging: towards molecular histopathology. Trends Biotechnol 2006;24:455–62.

Petibois C, Desbat B. Clinical application of FTIR imaging: new reasons for hope. Trends Biotechnol 2010;28:495–500.

Petibois C, Deleris G, Piccinini M, Cestelli Guidi M, Marcelli A. A bright future for synchrotron imaging. Nat Photonics 2009;3:179.

Petibois C, Piccinini M, Cestelli-Guidi M, Marcelli A. Facing the challenge of biosamples FTIR imaging using the synchrotron radiation source. J Synhrotron Rad. 2010a;17: 1-11.

Petibois C, Cestelli Guidi M, Piccinini M, Moenner M, Marcelli A. Synchrotron radiation FTIR imaging in minutes: a first step towards real-time cell imaging. Anal Bioanal Chem 2010b;397:2123–9.

Stephens DJ, Allan VJ. Light microscopy techniques for live cell imaging. Science 2003;300:82–6.

Please cite this article as: Mariangela C-G, et al, Experimental ATR device for real-time FTIR imaging of living cells using brilliant synchrotron radiation sources, Biotechnol Adv (2012), doi:10.1016/j.biotechadv.2011.11.009